Relapse of Challenging Behaviors in Known and Unknown Context Changes within an Intensive Outpatient Behavior Clinic

Ishita Aggarwal[1]; Matthew O'Brien, PhD, BCBA-D[2]; Alex Pauls, MA, BCBA[2]
Amador Valley High School, CA[1], The University of Iowa, IA[2]

University of Iowa Stead Family Children's Hospital

Introduction

- About 60% of individuals with developmental disabilities display challenging behaviors (CBs).[1]
- CBs are classified as behaviors with intensity, frequency, and duration that poses a safety concern to the individual exhibiting behaviors and/or to those around them.[2]
  - This includes aggression, self-injury, destruction, elopement, etc.
- Function-based treatments are highly effective for treatment of CBs[3], but their efficacy is limited by relapse.[4]
- This study examined a specific type of relapse in CBs that occurs following a context change, called *renewal*.
- Common context changes include setting, therapist and task changes, which are observable and known; however, there are many other context changes that may not be observable or known (e.g., biomedical conditions).
- Objective: The purpose of this study was to evaluate the relapse of challenging behaviors for patients receiving function-based treatments. More specifically, we sought to determine the proportion of relapse episodes associated with known context changes versus unknown context changes and further analyze the types of known context changes, as well as the magnitude and maintenance of renewal episodes.

Participants

We conducted a consecutive controlled case series of 15 patients from the BioBehavioral Day Treatment Clinic at the University of Iowa between the years 2019 and 2023 who met the following criteria (see Table 1):

1. Must display CB(s) in both assessment/treatment.
2. Must have socially maintained behavior and no automatically maintained behavior.

Methods

General Procedures and Data Collection:

For each patient, we reviewed all treatment sessions and notes on context changes. Sessions were conducted in 5-min intervals and data were recorded using responses per minute (RPM) of CB. For this study, data were collected using two methods.

Method 1 – Known Context Changes: Data were collected on the rate of CB in the five sessions preceding a known context change (i.e., therapist, setting, or task change) and the three sessions following the context change (see Figure 1). When the mean rate of CB of the three sessions following a context change exceeded the highest rate in the five preceding sessions, it was considered renewal.[5]

Method 2 – Unknown Context Changes: Data were collected on all relapse events and categorized as being associated with a known context change or an unknown context change.

Incidents of renewal (Method 1) were further classified by type (setting, therapist, task) and the magnitude and maintenance of renewal incidents were calculated as follows:

- Magnitude: percent increase in CB from max of the five pre-change sessions to average of the three post-change sessions.
- Maintenance: the maximum number of post-change sessions (in groupings of three) where the average exceeds the max of initial five pre-change sessions.

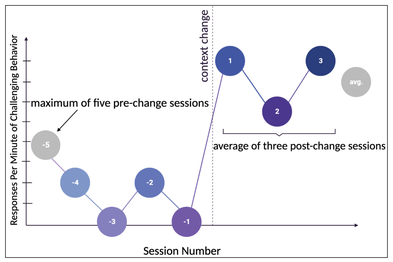

Figure 1: Renewal Definition

Figures

Renewal Frequency:

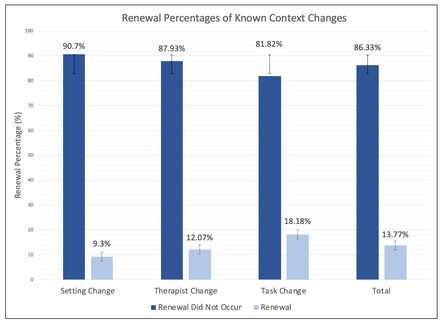

Figure 2: Frequency of Renewal for Known Context Changes (Setting, Therapist, and Task).

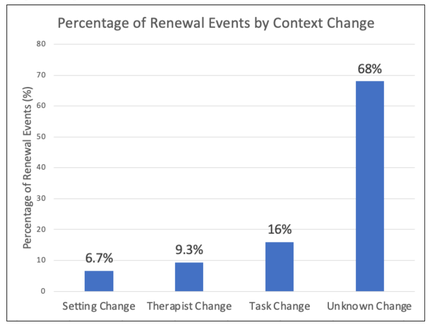

Figure 3: Percentage of each type of Context Change in Renewal Events.

Participant Demographics:

PATIENT NUMBER	YEAR	AGE	SEX	RACE	DX
1	2019	9	Male	White	ID
2	2019	10	Male	White	ASD, ADHD, ID
3	2023	7	Female	White	ADHD
4	2023	3	Male	Black	ASD
5	2023	17	Male	White	ASD, ID
6	2023	7	Male	White	n/a
7	2023	11	Male	Asian	ASD, ID
8	2023	8	Male	White	ASD, ADHD, ID
9	2023	13	Female	White	ADHD
10	2023	22	Male	White	ASD, ID
11	2023	6	Female	White	ASD, ADHD, ID
12	2022	6	Female	White	ID
13	2022	5	Female	White	ID
14	2022	5	Female	Multiple Races	ID
15	2022	12	Female	White	n/a

Table 1: Demographics of fifteen study participants.

Maintenance/Magnitude:

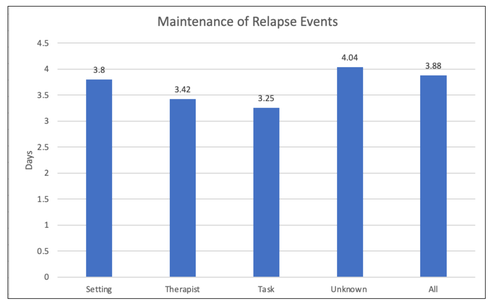

Figure 4: Maintenance (Average Duration) of Renewal for each type of Context Change.

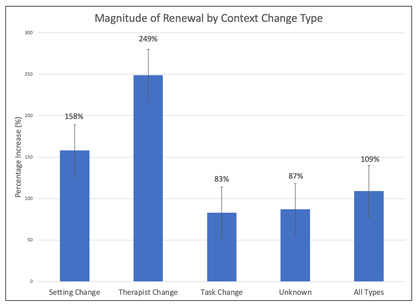

Figure 5: Magnitude (Average Percentage Increase) of Renewal for each type of Context Change.

Results

- Within known context changes:
  - Task-based context changes produced the greatest frequency of renewal (18.18%), followed by therapist (12.07%) and setting (9.30%) changes
  - Setting-based context changes were associated with the greatest maintenance (3.8 sessions) when compared to task (3.25 sessions) and therapist (3.42 sessions) changes.
  - Therapist-based context changes had the greatest magnitude (249% increase, on average), when compared to task (83%) and setting (158%) changes.
- When comparing known and unknown context changes:
  - Unknown context changes occurred more frequently (68% vs. 32%).
  - Unknown context changes had the greatest maintenance (4.04 sessions).
  - Known and unknown context changes had similar levels of magnitude.
- Of all events where renewal occurred, the majority were due to unknown context changes (68%), followed by context changes associated with task (16%), therapist (9.3%), and setting changes (6.7%).

Discussion

- Among known context changes, task-based renewal occurred at the greatest frequency, setting-based renewal occurred for the longest durations, and therapist-based renewal resulted in the greatest percentage increase in CBs.
  - Each type of known context change exceeded the other two in one of the analyzed parameters of renewal (frequency, maintenance, magnitude).
  - This suggests that each type of context change may have a unique effect on CBs and renewal.
    - Future research might consider which of the parameters evaluated in this study are most detrimental to patient treatment and plan to mitigate those effects.
- Unknown context changes were associated with over half of all relapse events and demonstrated the greatest maintenance when compared to known context changes.
  - This should be the focus of further study, as the majority of renewal events last longer, on average, than known context changes and may be caused by unknown internal/external factors that treatment providers are unaware of.
  - These data suggest that the current definition of "known context change" in applied research should be broadened past "task", "setting", and "therapist" to incorporate more types of context changes that may be internal or external to the patient. A broader definition would allow us to better monitor and identify connections between a patient's behavior and a respective context change.
- Of the parameters used to evaluate relapse, proportion of events and magnitude were associated with the greatest difference among context changes, while maintenance tended to be relatively similar across all context changes.
- Limitations to this study include the small sample size and potential omissions of context changes within the patient documentation.
- Future steps include collecting data on more participants to analyze a larger sample and looking for unknown context changes that are observable for data collection.

References

1. Reyes-Martín, J., Simó-Pinatella, D., & Font-Roura, J. (2022). Assessment of challenging behavior exhibited by people with intellectual and developmental disabilities: A systematic review. *International Journal of Environmental Research and Public Health*, *19*(14), 8701 https://doi/10.3390/ijerph19148701
2. Emerson, E. (2001). *Challenging behaviour: Analysis and intervention in people with severe intellectual disabilities*. Cambridge University Press.
3. Lindgren, S., Wacker, D., Schieltz, K. et al. (2020). A randomized controlled trial of functional communication training via telehealth for young children with autism spectrum disorder. *Journal of Autism and Developmental Disabilities, 50*, 4449–4462 https://doi.org/10.1007/s10803-020-04451-1.
4. Mitteer, D. R., Greer, B. D., Randall, K. R., & Haney, S. D. (2022). On the scope and characteristics of relapse when treating severe destructive behavior. *Journal of Applied Behavior Analysis, 55*(3), 688–703 https://doi.org/10.1002/jaba.912.
5. Muething, C., Call, N., Pavlov, A., Ringdahl, J., Gillespie, S., Clark, S., & Mevers, J. L. (2020). Prevalence of renewal of problem behavior during context changes. *Journal of Applied Behavior Analysis*, *53*(3), 1485-1493 https://doi.org/10.1002/jaba.740.

Automated Modeling of 3D Solar Cell Concentrators

Electrical & Computer Engineering Department, University of Iowa

Reyna Alam, Dorothy Zhang, Maxwell Leonard, Sebastian Hazlett , Daniel Keefe, Rezwan Mohammad Sayeed, and Fatima Toor, Ph.D.

Belin-Blank Center
College of Education
The University of Iowa

Introduction

- Solar energy is a rapidly growing energy source, particularly with green initiatives
- We aimed to determine the ideal solar cell concentrator shape among various polygonal compound parabolic constructions
- We developed two methods of solar tracking to further improve solar cell efficiency

Methods

We used OpenSCAD (parameterized, script-based CAD tool) to develop the 3D concentrator models using bash script

N-sided polygonal compound parabolic 8.0X concentration concentrators shown below, all 1 cm radius of bottom aperture and 6 cm tall

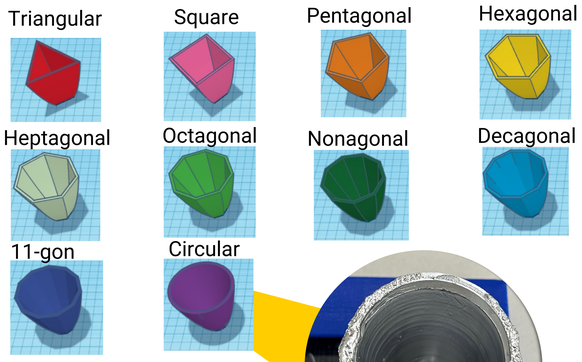

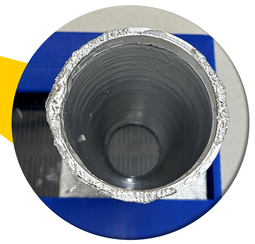

Smoothed and coated circular parabolic concentrator

Dual Axis Solar Tracking Systems

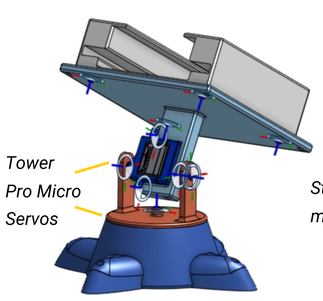

Photoresistor Method

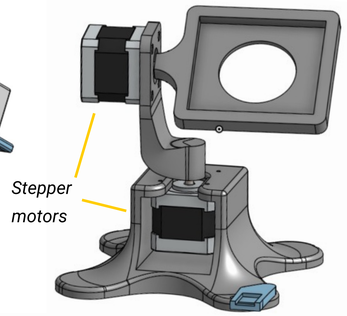

Sun Tracking Method

Coating and Ray-tracing

We chemically smoothed the 3D printed concentrators using X2C 3D print coating before coating them in reflective metal coating. Chromium, aluminum, copper, and nickel were tested on sample squares for reflectivity, as shown in figure A below. Chromium proved to be the most reflective and thus we coated our final concentrators with it.

Figure 1

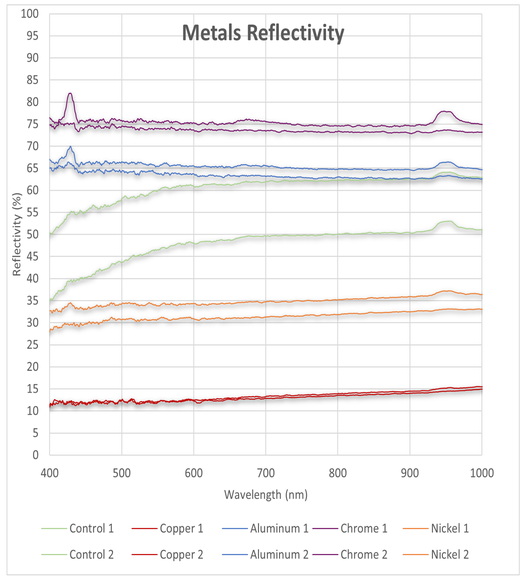

Above shows the reflectivity percentages of the four different metal coatings at corresponding wavelengths on the solar spectrum.

Figure 2

Radiance Ray-tracing of Each N-Sided Compound Parabolic Concentrator

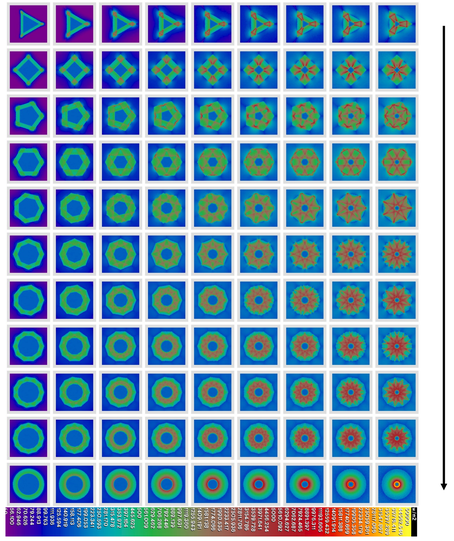

Results

Our experimental results of measuring each solar cell concentrator's short circuit density aligned with our observed theoretical pattern with an increasing number of sides for a given concentration ratio achieving a higher value and thus better observed efficiency.

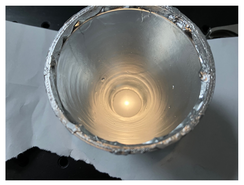

Figure 3

Short-Circuit Current Density (J_{SC})

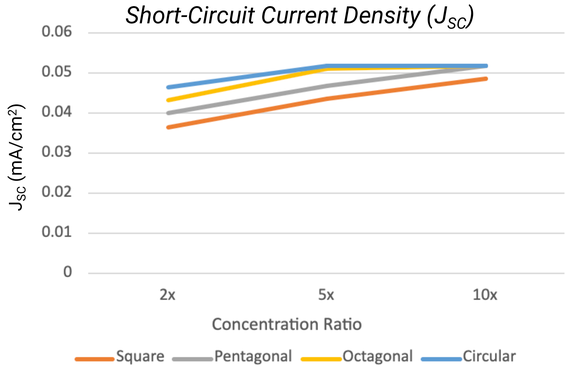

Conclusions

Through my team's investigation of the ideal design for solar cell concentrators, we devised a way to automate the 3D modeling process of these concentrators with our OpenSCAD program. In this way, other researchers looking to easily and efficiently develop concentrator 3D models can use our program as a tool in their own research or applications.

Figure 4
Radiance Ray-Tracing Results (With 256-Sided)

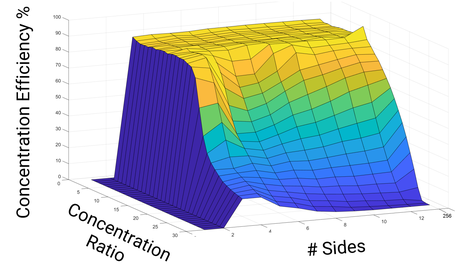

Acknowledgments

Thank you to my lab members for making this experience possible and always entertaining, and to my mentor Dr. Toor, graduate students Dan and Rezwan, and super cool guys Nick and Caleb for their guidance. I'm also glad to have spent time with the RA's and made so many good memories ☺

References

1. **Cooper, T., Dähler, F., Ambrosetti, G., Pedretti, A., & Steinfeld, A. (2013).** Performance of compound parabolic concentrators with polygonal apertures. *Solar Energy*, *95*, 308–318. https://doi.org/10.1016/j.solener.2013.06.023
2. **Rincón, E., Lentz, A. (2009b).** *New solar air heater based on Non-Imaging Optics for High-Temperature applications*. https://doi.org/10.1115/es2009-90306

Link to research brief

MATLAB Code

IOWA

Assessing Anti-Seizure Properties of Ibuprofen and Genistein in a *Drosophila* Epilepsy Model

Lila Anafi*[1], Brady Williquett[2], Oliver Cho[3], Gowthami Vidhya[4], J. Robert Manak[5]

[1]Lower Merion High School, [2]Department of Biology, University of Iowa, Iowa City, IA 52242, [3]The Nueva School, [4]Kings High School, [5]Department of Pediatrics, University of Iowa Carver College of Medicine, Iowa City, IA 52242.

Abstract

One third of epilepsy patients do not respond to currently available medications[1]. To search for **alternative treatments,** we tested whether the anti-inflammatory drug ibuprofen & anti-oxidant drug genistein **alleviate seizures** in a seizure-prone line of *Drosophila melanogaster.* We chose these drugs based on data generated by the Manak lab demonstrating that oxidative stress activates the brain innate immune response, which in turn leads to epilepsy progression[2].

Drosophila with mutations in the *prickle* gene, especially in the ***prickle-spiny legs*** isoform, exhibit myoclonic (isolated muscle contraction) seizures similar to those observed in human patients carrying *PRICKLE* mutations[4]. Flies homozygous for pk^{sple} were treated with varying drug concentrations, then assessed for seizure penetrance. While neither drug resulted in significant seizure reduction, 4μM of genistein showed a decrease in seizures.

Background

Epilepsy

- Affects 1% of population[1]
- Associated with increased **oxidative stress** (production of reactive oxygen species in cells)[3]
- Associated with increased activation of brain **innate immune response**[3]
- Both decreasing **oxidative stress** levels & inactivating the brain **innate immune response** suppress seizures[3] (see Figures 1-3)

Genistein

- Phytoestrogen[5]
- Reduces **oxidative stress** by increasing expression of anti-oxidant enzymes[5]

Ibuprofen

- Anti-inflammatory
- Blocks cells' production of prostaglandins, which help to trigger the **innate immune response**[2]

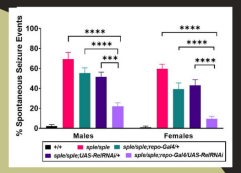

Figure 1. Knockdown of Relish transcription, & subsequently the **innate immune response,** leads to lower seizure penetrance.[3]

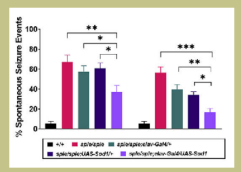

Figure 2. Overexpression of Sod1, which reduces **oxidative stress,** leads to lower seizure penetrance.[3]

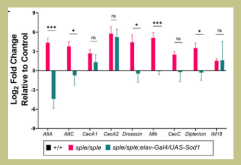

Figure 3. Overexpression of Sod1 suppresses the innate immune response, providing evidence that oxidative stress acts **upstream** of the IIR.[3]

Nukala et al, 2023 (Figures 1-3)

Methods

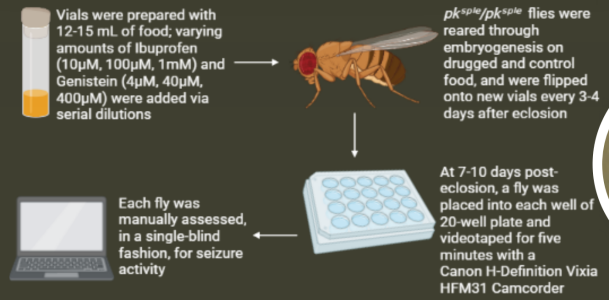

Drug-treated & control pk^{sple}/pk^{sple} flies were analyzed for **seizure activity** at 7-10 days post-eclosion, at which time the **number of seizures** experienced in five minutes were quantified.

Results

Figure 4. No significant difference between controls & genistein-treated pk^{sple}/pk^{sple} flies was observed at any of the indicated concentrations. Data shown is mean +- SEM; Mann-Whitney test (uncorrected); 1-3 seizure assays; 7-10 flies per sex per assay; ns = not significant.

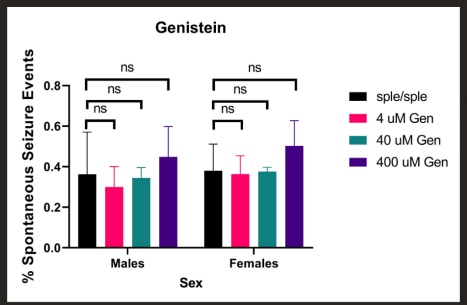

Figure 5. No significant difference between controls and ibuprofen-treated flies was observed at any of the indicated concentrations. Data shown is mean +- SEM; Mann-Whitney test (uncorrected); 1-3 seizure assays; 7-10 flies per sex per assay; ns = not significant.

Scan QR code for in-progress site on pk^{sple}-mediated seizure identification.

Figure 6. A 20-well plate in which we placed flies for seizure assays.

Conclusions

Neither **Genistein** nor **Ibuprofen** was shown to significantly reduce pk^{sple}-mediated seizure penetrance at any concentration tested. However, 4μM of genistein showed a slight decrease in seizure penetrance.

Future Directions

Redo experiment with improved seizure calling accuracy and/or more flies to increase statistical power. The Manak lab will continue assessing antioxidant & anti-inflammatory drugs for anti-seizure properties in the ***prickle-spiny legs*** model.

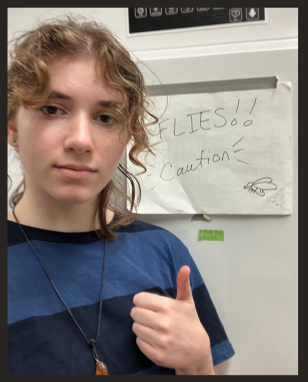

Figure 7. Author standing in front of the fly incubator.

Acknowledgements

I would like to thank **Dr. Manak, Brady Williquett,** & the **Secondary Student Training Program** for giving me the opportunity to contribute to this project.

Funding

University of Iowa Stead Family Department of Pediatrics Research Grant to J.R.M.

References

1. Kwan, P., and Brodie, M.J. (2000). Early identification of refractory epilepsy. N. Engl. J. Med. 342, 314–319. 10.1056/NEJM200002033420503
2. Ngo, Vincent Trung H. and Tushar Bajaj. "Ibuprofen." StatPearls, StatPearls Publishing, 29 May 2023.
3. Nukala, K. M., Lilienthal, A. J., Lye, S. H., Bassuk, A. G., Chtarbanova, S., & Manak, J. R. (2023). Downregulation of oxidative stress-mediated glial innate immune response suppresses seizures in a fly epilepsy model. *Cell Reports*, *42*(1), 112004. https://doi.org/10.1016/j.celrep.2023.112004
4. Tao, Hirotaka, et al. "Mutations in Prickle Orthologs Cause Seizures in Flies, Mice, and Humans." The American Journal of Human Genetics, vol. 88, no. 2, 2011, pp. 138–149, https://doi.org/10.1016/j.ajhg.2010.12.012.
5. Zhang, Sai, et al. "Neuroprotective Effects of Genistein on SH-SY5Y Cells Overexpressing A53T Mutant α-Synuclein." Neural Regeneration Research, vol. 13, no. 8, 2018, p. 1375, https://doi.org/10.4103/1673-5374.235250.

Bioengineered Tissue Patches for Dynamic Organ Mimicry using Silk Fibroin

Donovan J Burke[1], Hannah J Vogts[2], Reza Amouzandeh[2], Milad Arzani[2], Mohan Yu[3], Xuan Mu, Ph.D.[2]

[1]College Park High School; [2]Roy J. Carver Department of Biomedical Engineering,[3]Department of Mechanical Engineering, The University of Iowa

Problem

Current Therapuetic Patches Are Not Biocompatible

Contemporary therapeutic patches fail to compensate for the **anisotropic deformation** of organs that are intrinsically anisotropic or auxetic (negative Poisson's ratio) (Chansoria et al., 2022).

In addition, patches made from **synthetic polymers** often lack biocompatibility, which may cause a negative immune response in the body (Fernandez-Yague et al., 2022).

PEGDA Hydrogel

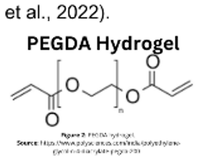

Research Goal

Engineering Goal

Develop a **therapeutic patch** that accounts for the anisotropic deformation of organs, such as the heart, through the use of **monolithic proteinaceous non-synthetic materials.**

Materials

- InkRedible3D Printer
- Silk Cocoons
- Ultra Pure Water
- PDMS
- Lithium Bromide
- Dialysis Tubing
- Enrichment Cassette
- Salt bath

Approach

Accounting For anisotropic deformation

Auxetic patch design, such as the one seen to the right, has demonstrated the ability to account for the **anisotropic deformation** of organs.

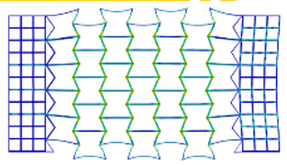

Figure 3: Auxetic Honeycomb structure while stretched

Biocompatible Materials

Figure 4: Cut up silk cocoons with the silk worm removed

To account for the lack of biocompatible hydrogels, **silk fibroin** was developed inside the Mu lab. This silk fibroin is **capable of being 3D-printed** to create the therapeutic patches in this project (Mu et al., 2022).

Methodology

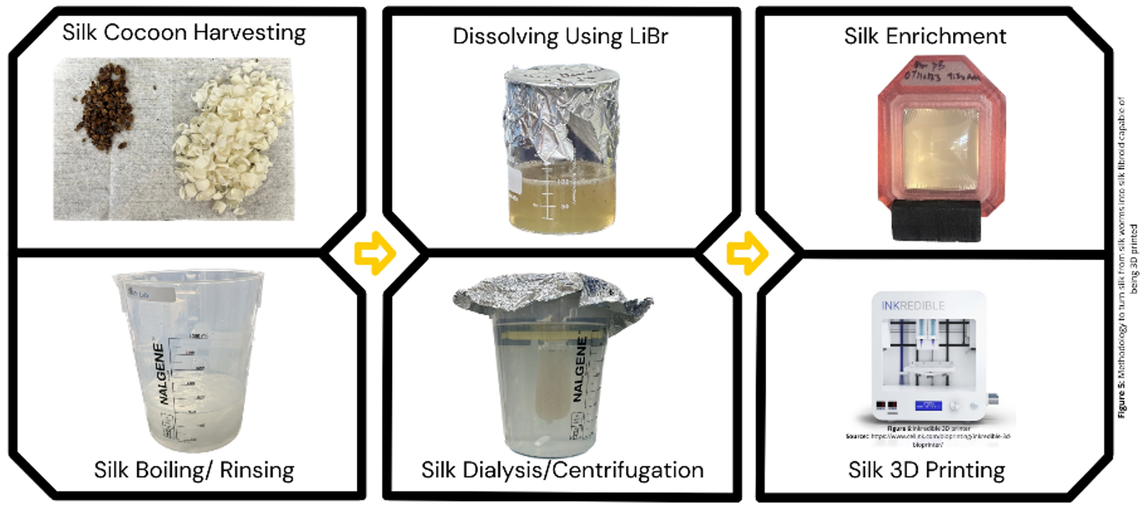

Figure 5: Methodology to turn silk from silk worms into silk fibroin capable of being 3D printed

Results

Arrowhead

Poisson's Ration: 0.024

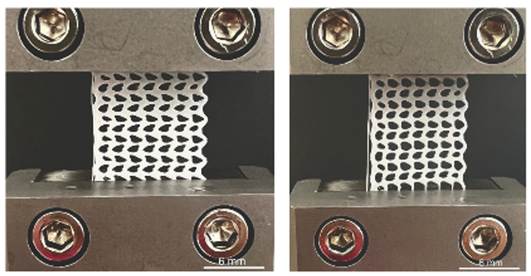

Chiral Truss

Poisson's Ration: 0.22

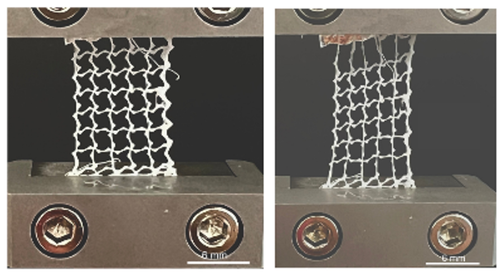

Re-entrant Honeycomb

Poisson's Ration: 0.98

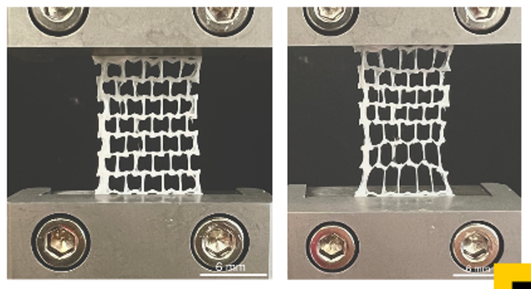

Lozenge Truss

Poisson's Ration: 0.48

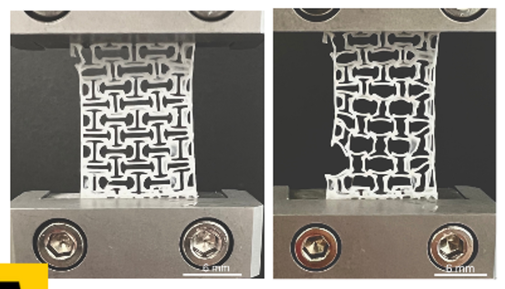

Discussion

Auxetic Design Implications

The results indicate that the **project goal has not yet been reached,** and the patches are not yet ready to be produced. The stretching of the designs often led to tearing, indicating that more layers are needed so that the patch can reach its fully stretched auxetic state.

Future Auxetic Designs

Future patch designs will incorporate two significant changes:

- First, the **layer count of the patches will increase** to prevent tearing when under significant strain of 20% or more
- Second, the **size of each unit in the design will increase,** which will decrease the overall number of units per patch. This will allow the strain and auxetic performance to be equally distributed across the structure.

Conclusion

Application of Tissue Patches

- **Rapid Recovery of Organ-Based Surgeries**
  - Through using a biocompatible nonsynthetic material, cells are able to regenerate and grow on the patches. This will allow for a speedy recovery from injury or surgery.
- **More Effective Small-Scale Bandage**
  - Heighten cell regeneration.
  - The auxetic design can account for the stretching of smaller appendages such as the fingers and feet.

Summary

- Contemporary therapeutic patches are unable to account for the anisotropic deformation of organs and may cause negative immune responses due to the nonsynthetic materials used.
- Testing indicates that the therapeutic patches created from silk fibroin, while functional, would likely become stronger with **fewer units and more layers.**

Acknowledgement

Thank you to the Belin-Blank Center at the University of Iowa for granting me this opportunity, and a special thanks to the Mu Lab, especially Hannah J Vogts and Dr. Mu, for their mentorship throughout this project and my time in the lab.

References

Chansoria, P., Blackwell, J., Etter, E. L., Bonacquisti, E. E., Jasiewicz, N., Neal, T., Kamal, S. A., Hoque, J., Varghese, S., Egan, T., & Nguyen, J. (2022). Rationally designed anisotropic and auxetic hydrogel patches for adaptation to dynamic organs. Advanced Functional Materials, 32(43). https://doi.org/10.1002/adfm.202207590

Fernandez-Yague, M. A., Hymel, L. A., Olingy, C. E., McClain, C., Ogle, M. E., Garcia, J. R., Minshew, D., Vyshnya, S., Lim, H. S., Qiu, P., Garcia, A. J., & Botchwey, E. A. (2022). Analyzing immune response to engineered hydrogels by hierarchical clustering of inflammatory cell subsets. Science Advances, 8(8). http://doi.org/10.1126/sciadv.abd8056

Mu, Xuan, et al. 3D Printing of Monolithic Proteinaceous Cantilevers Using Regenerated Silk Fibroin. Molecules 27.7 (2022): 2148.

Polymerization of Amine Derivatives Yielding Polymers with Conjugated –NS- and –NSS- Backbones

Jolene Cao[1], Atman Shah[2], Shanari Wickremasinghage[3], B.S., Ned Bowden[3], Ph.D.

[1]Smithtown High School East, [2]Archbishop Mitty High School, [3]Department of Chemistry, University of Iowa

Department of Chemistry

Introduction

Degradable and Electrically Conductive Polymers (DECPs)

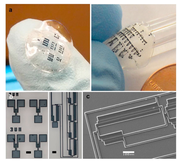

- Biomedical applications: drug or gene delivery, tissue engineering, and medicine
- Ideally nontoxic, stable, and cleavable
- Have controlled degradation in the body

Fig. 1. DECP biosensors formed on flexible substrates (Kenry & Liu, 2018)

Polymers based on Polythiazyl $(SN)_x$

- Conjugated backbones with S-N bond
- Stable and easier to alter properties
- Carbamates, ureas, and diamines have yet to be studied as monomers

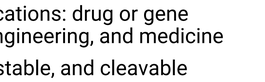

Fig. 2. Polythiazyl Structure (Paudel et al., 2023)

Poly[(*N*,*N*-phenylamino)disulfides]

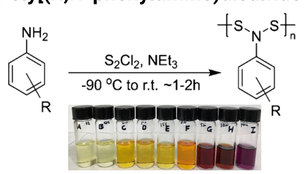

Fig. 3. Synthesis of Poly-NADs (Grace et al., 2021)

Poly[(*N*,*N*-amino)sulfide]

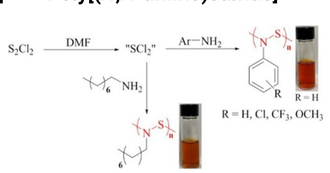

Fig. 4. Synthesis of Poly-NAS (Paudel et al., 2023)

Hydrogen Sulfide in Agriculture

Fig. 5. H_2S releasing dibutyldithiophosphate fertilizer was found to significantly increase harvest yield using a Tukey–Kramer test. (Brown et al., 2021)

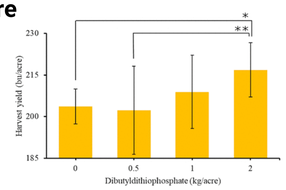

Research Question

How can a series of polymers with conjugated –NS- and –NSS- backbones be synthesized, isolated and characterized?

Methodology

Synthesis and Isolation of Polymers

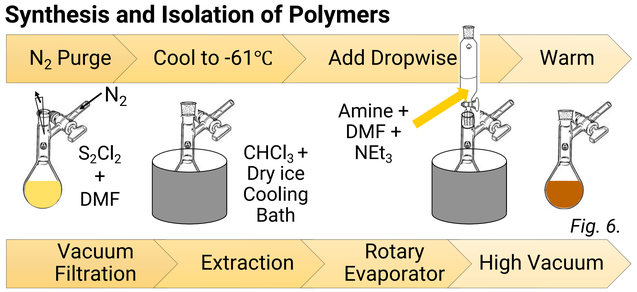

Fig. 6.

Spectroscopy & Chromatography Techniques

^{1}H NMR	UV-Vis	SEC-MALS

Results & Discussion

NS Polymerization

General Monosulfide Polymerization Scheme

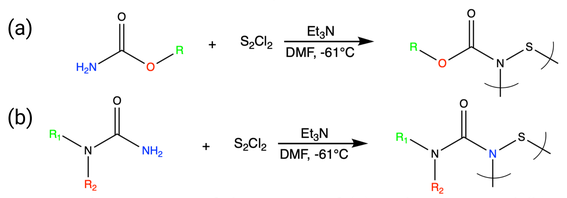

Fig. 7. Polymerization of derivatives of (a) carbamates and (b) ureas. DMF was reacted with S_2Cl_2 to produce a monosulfide transfer reagent.

Monomers Used:

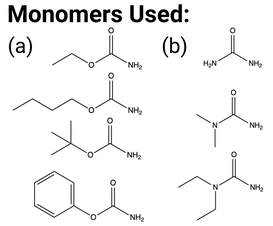

Fig. 8. Derivatives of (a) carbamates and (b) ureas were reacted

Effects of Molar Ratios on Polymerization

Amine : S_2Cl_2	Color	Solubility	
		Water	Brine
0.92:1	Dark red	Soluble	Soluble
0.95:1	Orange	Insoluble	Insoluble
0.97:1	Yellow	Soluble	Soluble

Table 1. Optimization of molar ratios for greatest isolated yield of SN backbone polymers synthesized from butyl carbamate.

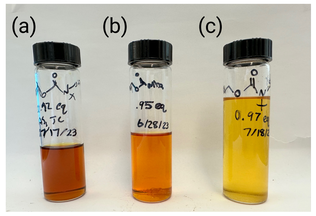

Fig. 10. (a-c) 0.92, 0.95, and 0.97 equivalences amine : S_2Cl_2 respectively.

Ureas vs. Carbamates

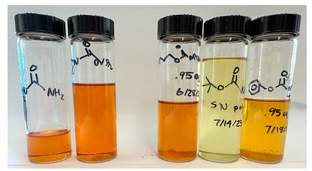

Fig. 9. SN polymers in solution with different functional groups Monomers used (left-right): urea, 1,1-dimethylurea, butyl carbamate, tert-butyl carbamate, phenyl carbamate

(All polymers were synthesized using a 0.95:1 ratio of amine monomer to S_2Cl_2)

^{1}H NMR of Monomer

^{1}H NMR of Polymer

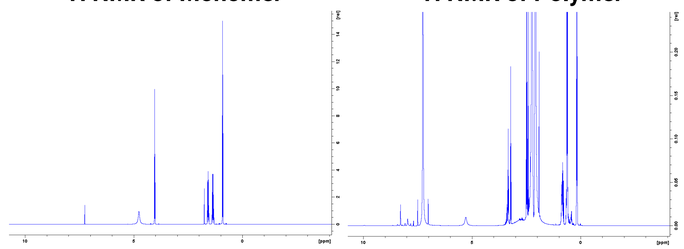

Fig. 11. The ^{1}H NMR spectra of the butyl carbamate monomer and its corresponding –NS- Polymer were obtained (400 MHz, $CDCL_3$). A broadening of peaks suggests the successful synthesis of the polymer.

NSS Polymerization

General Disulfide Polymerization Scheme

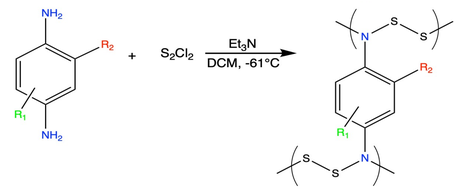

Fig. 12. Schematic of polymerization of diamine derivatives to yield -NSS- backbone polymers

Quick 2-D Printing

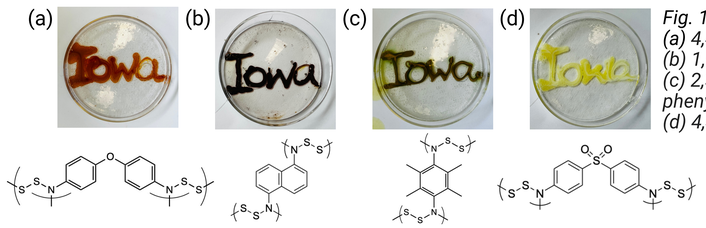

Fig. 13. Polymerized from (a) 4,4'-Oxydianiline (b) 1,5-Diaminonaphthalene (c) 2,3,5,6-Tetramethyl-1,4-phenylenediamine (d) 4,4'-sulfonyldianiline

These brightly colored –NS- and –NSS- backbone polymers are stable in organic solvents and ideal for applications including drug/gene delivery, sensors, medicine and fertilizer. In addition, they can be easily printed for biocompatible devices and act as colorimetric sensors.

Conclusion

- **Polymers with conjugated –NS– and –NSS– backbones** were produced, and their synthesis was confirmed using ^{1}H NMR.
- The colors of these polymers arise from their **conjugated backbone** that has an **energy band gap in the visible light range**.
- **Different equivalences** of amines affected polymer characteristics and yield.
- –NSS– polymers were successfully used for **quick 2-D printing**.

Future Works

- Test electrical conductivity enhancing dopants (e.g., Br_2) on the polymer
- Synthesize polycyclic polythiazyl derivatives using hydrazine

Acknowledgements

Thank you Prof. Bowden and Shanari Wickremasinghage for mentoring and supporting me during this great experience. I would also like to thank the Bowden Group.

References

Brown, E. M., Ranasinghe Arachchige, N. P. R., Paudel, A., & Bowden, N. B. (2021). Synthesis, Stability, and Kinetics of Hydrogen Sulfide Release of Dithiophosphates. *Journal of Agricultural and Food Chemistry*, *69*(43), 12900–12908. https://doi.org/10.1021/acs.jafc.1c04655

Grace, J.P., Flitz, E.S., Hwang, D.S., & Bowden, N.B. (2021). Polymerization of Aniline Derivatives to Yield Poly[N,N-(phenylamino)disulfides] as Polymeric Auxochromes. *ACS Macromolecules*, *54*(22), 10405-10414. https://doi.org/10.1021/acs.macromol.1c01548

Kenry, & Liu, B. (2018). Recent advances in biodegradable conducting polymers and their biomedical applications. *Biomacromolecules*, *19*(6), 1783–1803. https://doi.org/10.1021/acs.biomac.8b00275

Paudel, A., Campbell, E.J., Van Benschoten, W.Z., Otting, G.W., Shepard, J.J., & Bowden, N.B. (2023). Polymerization of Primary Amines with Sulfur Monochloride to Yield Red Polymers with a Conjugated SN Backbone. *ACS Macromolecules*, *56*(10), 3721-3730. https://doi.org/10.1021/acs.macromol.2c02507

The Ajamization of Islamic Manuscripts in Arabic: An examination of Islamic faith and Arabic script in West African Manuscripts from the 17th to 20th Century

Introduction of Islamic Faith to West Africa

Islam first arrived in the North African Sahel region through Arab traders and later spread to Ancient Ghana and the zone of Kanem in West Africa. Wherever Islam spread, Arabic, considered the language of the gods in Islam, would follow. Therefore, Arabic was used by African scholars and became an important part of education in Africa

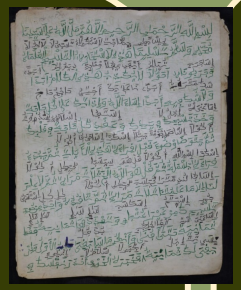

Collection of Multilingual Ephemeral Text III with glosses in Mandinka

Significance

- African manuscripts have been under-represented in historical research and have often been dismissed or destroyed
- Gaining comprehensive understanding of world culture requires the study of all cultures
- Contributes to the Global Writing Culture website that will be used as an educational tool

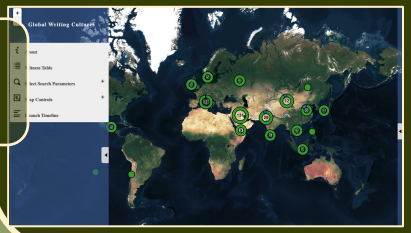

Global Writing Culture Website

Results

I recorded a total of eleven manuscripts. For each manuscripts recorded, I also included a paragraph description, and information such as languages, scripts, forms, script format, material, find date, place of composition, current location, content, religion, coordinate location, and additional information on the appearance of each manuscript such as height and dimension, whether the manuscript is a colophon or palimpsest, and more.

- Multiliteracy of West African Scholars
- Help add to Professor Dilley's Manuscript Database website

Query Results				Y/N
id	manuscript	significance	is_multi_mss_co	multilingual
1	Cheikh Moustapl	The Cheikh Mous	N	Y
2	Tanbīh al-ghāfilīn	Created around t	N	Y
3	Fā'idahs with inv	Manuscripts cont	N	Y
4	History of Hausa	Part of a collectic	N	Y
5	Kandoolu Kitaab	Part of the Issa D	Y	Y
7	Kandoolu Kitaabe	This manuscript a	Y	Y
8	Kanjamaalu Kita	Also known as C	N	Y
9	Celebrating Prop	Also known as B	Y	Y
10	Fula Ajami Poetr	Showcasing the u	Y	Y
11	Jante la Kandool	This manuscript i	Y	Y

What are Ajami Scripts?

- African Languages written in Arabic Script.
- Like how European languages adopted Latin Script and Japanese adopted the Chinese Script.
- Many manuscripts are in Arabic but have glosses in Ajami languages.

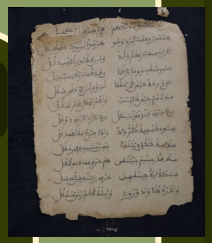

Fula Ajami Poetry

Methods

British Library Endangered Archives

Hill museum & manuscripts library

GPR for Ionized Particle Energy Prediction

Reducing Computational Cost of WDM Simulations using Machine Learning

Kat Carver, Gabriel Smith, William Van Benschoten, James Shepherd

Introduction

Warm dense matter (WDM) is a classification of states of matter within the temperature range of a plasma (0.1 – 100 eV) and the density of a solid. It can be defined as having its coupling (Γ) and degeneracy (Θ) parameters near 1, as defined by the equation

$$\Gamma = Z^2 e^2 / 4\pi\epsilon_0 d k_B T$$

WDM can be modeled; however, its computational cost is substantial, necessitating the exploration of cost reduction strategies, in this case, Gaussian Process Regression. Gaussian Process Regression (GPR) is a versatile statistical technique used to model complex systems and predict outcomes with uncertainty estimation. It employs Gaussian processes to infer relationships from data, making it adaptable to diverse applications in science and engineering.

Research Question

How can the composition of a Gaussian Process Regression (GPR) model's covariance function be approached to enhance the prediction accuracy of the electronic energy in an ionized particle?

Methods

- Implementation of Gaussian Process Regression (GPR) in Python using the NumPy library for computational efficiency
- Empirical validation of GPR predictions using data obtained from Hydrogen 4 simulation for performance assessment
- Exploration of the influence of standard covariance functions on the predictive capabilities of GPR
- Development and integration of a new kernel using the generalized Matérn function where v = 3
- Final performance assessment of the new kernel's performance on data of Carbon and Carbon+ particle simulations

Python Libraries:

- **Data processing:** Numbers Python (NumPy), Pandas
- **Plotting:** matplotlib, matplotlib.pyplot

$$C_{p+\frac{1}{2}}(d) = \sigma^2 \exp\left(-\frac{\sqrt{2p+1}d}{\rho}\right) \frac{p!}{(2p)!} \sum_{i=0}^{p} \frac{(p+i)!}{i!\,(p-i)!} \left(\frac{2\sqrt{2p+1}d}{\rho}\right)^{p-1}$$

The generalized equation for Matérn covariance where $\nu = p + \frac{1}{2};\ p \in \mathbb{N}^+$

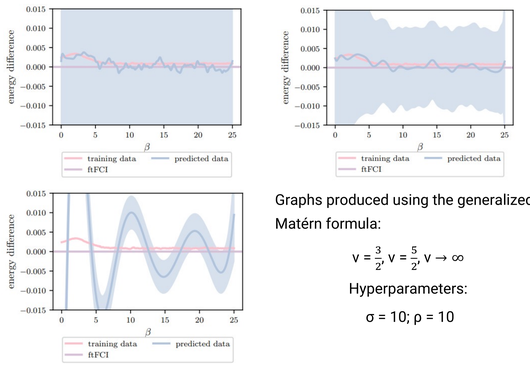

Graphs produced using the generalized Matérn formula:

$\nu = \frac{3}{2}, \nu = \frac{5}{2}, \nu \to \infty$

Hyperparameters:

σ = 10; ρ = 10

2 Matérn $\frac{7}{2}$ on Equilibrium H4

- Matérn $\frac{7}{2}$ with σ = 10 and ρ = 10 is the result of testing using different hyperparameter values and the approximate optimal values of hyperparameter(s) for the function.
- Data observed after testing both Matérn $\frac{3}{2}$ and Matérn $\frac{5}{2}$ provided evidence supporting the hypothesis of graphs exhibiting less erratic patterns and error bars showing reduced dispersion with increasing v.
- Based on prior observations, the empirical evidence suggested that the function would be well-suited for testing on larger carbon systems.

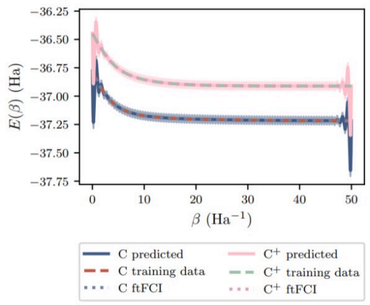

Graphs produced through the use of Matérn $\frac{7}{2}$ with hyperparameter values σ = 10 and ρ = 10 on training data of carbon and carbon+ particles

1 Matérn Covariance; Increasing the value of v

- As v (varying from v = $\frac{3}{2}$, v = $\frac{5}{2}$, and v → ∞ approaching infinity) increases, a noticeable trend is observed with the prediction graph exhibiting gradual smoothing.
- Matérn $\frac{3}{2}$ displayed considerable dispersion in error bars, whereas an increase in v resulted in error reduction, especially noticeable in the case of the squared exponential.
- Matérn $\frac{3}{2}$ exhibited acceptable fitting performance across the entire range, upon which Matérn $\frac{5}{2}$ showed marginal improvement.

Graph produced using Matérn $\frac{7}{2}$ following the generalized formula with σ = 10 and ρ = 10

3 Proof of Concept: C/C+ testing

- While predictions remain marginally imprecise at extreme values of beta, the function exhibits notably high accuracy for intermediate values.
- The error bars in the intermediate range are of negligible magnitude, allowing for clear differentiation between the graphs of the two systems.
- H4 predictions demonstrated high accuracy across the entire range, however, C and C+ predictions notably exhibited suboptimal accuracy for extreme values of β.

Summary of Findings

- The Matérn kernel family (Squared Exponential and Matérn $\frac{3}{2}$, $\frac{5}{2}$, $\frac{7}{2}$) demonstrated unparalleled accuracy.
- The covariance matrices generated using the Matérn $\frac{7}{2}$ function, as modeled by the generalized, equation yielded the best results overall.
- Only a few kernels produced unfavorable results; most performed reasonably well and were able to be further tuned through adjusting the hyperparameters.
- Some covariance functions excelled at predicting extreme β values, while others performed better at intermediate β values. We found that through multiplying kernels, the resulting graphs inherit properties of the graphs produced originally.

Future work

To enhance the predictive capacity and applicability of Gaussian process regression in ionized particle energy prediction, further research should aim to:

- Further investigate the multiplication or otherwise combination of individual covariance functions to leverage their distinct strengths at different β regimes.
- Conduct a systematic exploration of further increasing the value of v and adjusting hyperparameters σ and ρ to produce the optimal Matérn kernel configuration.

Acknowledgments

I extend my sincere appreciation to Gabe Smith and Professor Shepherd for their invaluable mentorship and constructive guidance throughout my project. Furthermore, I am grateful to the Belin-Blank Center and the SSTP for providing this exceptional research opportunity.

References

1. Rasmussen, C. E., & I., W. C. K. (2008). Chapter 4 Covariance Functions. In Gaussian processes for machine learning. essay, MIT Press.
2. Falk, K. (2018). Experimental methods for warm dense matter research. High Power Laser Science and Engineering, 6. https://doi.org/10.1017/hpl.2018.53
3. Los Alamos National Laboratory, O. by L. A. N. S. (n.d.). The Physical Regimes. Physical Regimes. https://www.lanl.gov/projects/dense-plasma-theory/background/physical-regimes.php#gamma

Assessing Anti-Seizure Properties of Antioxidants Gallic Acid and Allyl Disulfide in a *Drosophila* Epilepsy Model

Oliver Cho[1]; Brady Williquett[2]; J. Robert Manak, Ph.D.[2,3]

[1]The Nueva School, [2]Department of Biology, [3]Department of Pediatrics, University of Iowa

RESEARCH OBJECTIVE

To assess the effectiveness of two antioxidants, gallic acid and allyl disulfide, in suppressing myoclonic seizures in *pk^{sple}* mutant flies

INTRODUCTION

Epilepsy is a neurological disease characterized by recurrent seizures and affects over 50 million people worldwide. Despite a wide variety of anti-epilepsy drugs (AEDs) on the market, approximately one-third of epilepsy patients do not respond to available therapies and two-thirds report adverse side effects.[1]

The *prickle* gene found in *Drosophila melanogaster* expresses two adult isoforms: *prickle-prickle* and *prickle-spiny-legs*. Mutations in the *prickle-spiny-legs* (*pk^{sple}*) isoform lead to myoclonic seizures and locomotor defects in flies akin to those observed in human *PRICKLE* patients.[2]

Research in the Manak Laboratory has revealed a significant increase in oxidative stress in *pk^{sple}* mutant neurons, which activates the innate immune response (IIR) in glial cells. This heightened IIR activity promotes neuronal cell death, fostering a positive feedback loop that further amplifies glial IIR activation and culminates in the escalation of the seizure phenotype and epileptogenesis.[3] Given the connections between oxidative stress and epilepsy progression, we decided to test whether two antioxidants, gallic acid and allyl disulfide, had anti-seizure properties in our fly epilepsy model.

In this research, we discovered that the two antioxidants, gallic acid and allyl disulfide, do not have anti-seizure effects in *pk^{sple}* mutants. These data serve to augment existing antioxidant drug screening research in *Drosophila* and assist in the discovery of novel therapeutics for managing epilepsy, particularly in cases unresponsive or averse to conventional AEDs.

Figure 1. Tissue-Specific Gene Expression in *Drosophila* via the GAL4/UAS system

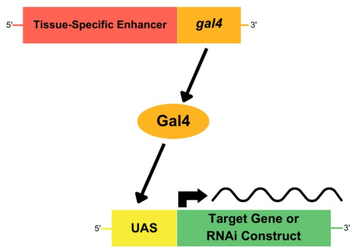

Figure 2. Overexpression of *Superoxide Dismutase 1* (*Sod1*) Pan-Neuronally Suppresses Neuronal Cell Death

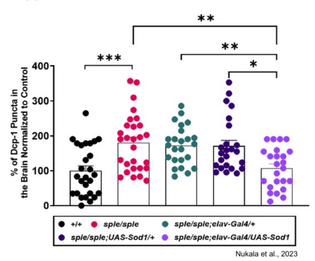

Nukala et al., 2023

Figure 3. Overexpression of Sod1 Suppresses *pk^{sple}*-Mediated Myoclonic Seizures

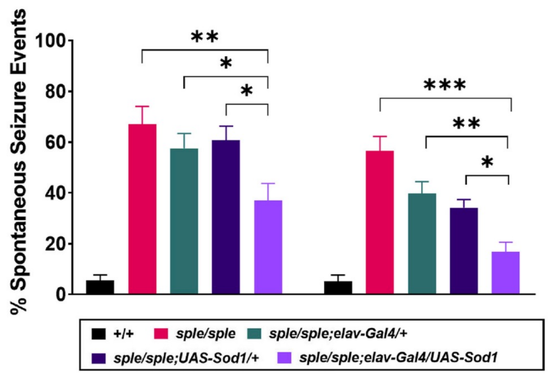

Nukala et al., 2023

METHODS

***Drosophila* Stocks:**

- The *pk^{sple}* mutation was outcrossed into a *w^{1118}* background. *pk^{sple}*/*pk^{sple}* (*w^{1118}*) flies were used in all experiments.

Gallic Acid and Allyl Disulfide Feeding:

- Drug food was made by combining standard cornmeal molasses *Drosophila* medium with gallic acid (10μM, 100μM, and 1mM) and allyl disulfide (20μM, 200μM, and 2mM).

Spontaneous Seizure Assay:

- *pk^{sple}*/*pk^{sple}* flies were either treated or left untreated with drug throughout early development and then up to 7-10 days post-eclosion at 25°C.
- 10 male and 10 female flies were mouth-pipetted into a 20-well plate and recorded for 5 minutes.
- Seizures were assessed by eye with a single-blind setup.

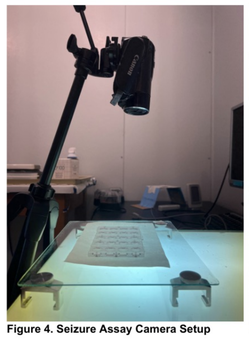

Figure 4. Seizure Assay Camera Setup

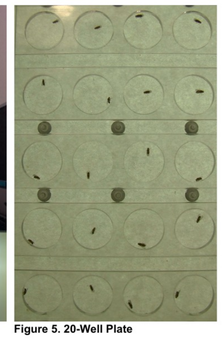

Figure 5. 20-Well Plate

RESULTS

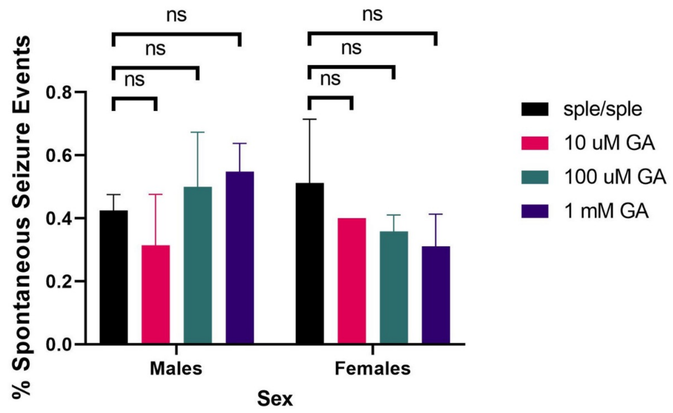

Figure 6: Gallic acid-enriched diet does not decrease spontaneous seizure activity in *pk^{sple}* mutants. Quantification of seizure events in *sple*/*sple* mutants on 10μM, 100μM, and 1mM gallic acid. ns = not significant. Mann-Whitney Test, Error bars: SEM, n = 2-4 biological replicates, 7-10 flies per sex in each seizure assay.

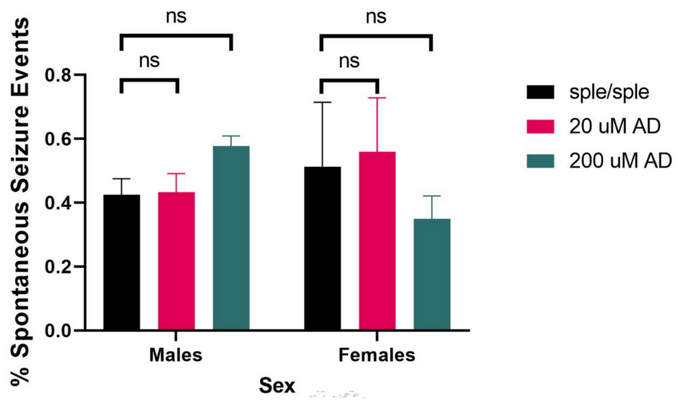

Figure 7: Allyl disulfide-enriched diet does not decrease spontaneous seizure activity in *pk^{sple}* mutants. Quantification of seizure events in *sple*/*sple* mutants on 20μM, 200μM, and 2mM allyl disulfide. ns = not significant. Mann-Whitney Test, Error bars: SEM, n = 2-4 biological replicates, 7-10 flies per sex in each seizure assay.

CONCLUSIONS

- Neither gallic acid nor allyl disulfide were effective in significantly suppressing *pk^{sple}*-mediated seizures at the concentrations tested.
- While not statistically significant, 10uM GA in males showed a decrease in seizure penetrance.
- In females, all GA concentrations showed a decrease in seizure penetrance.
- For allyl disulfide, 200uM showed a decrease in seizure penetrance in females only.

FUTURE DIRECTIONS

- Redo experiment with more flies to increase statistical power.
- Improve accuracy in calling spontaneous seizures.
- Try a combination of gallic acid and allyl disulfide.
- Increase drug concentrations to determine whether higher doses might be more effective in suppressing seizures.

REFERENCES

1. Kwan, P., & Brodie, M. J. (2000). Early identification of refractory epilepsy. *New England Journal of Medicine*, 342(5), 314–319. https://doi.org/10.1056/nejm200002033420503
2. Ehaideb, S. N., Wignall, E. A., Kasuya, J., Evans, W. H., Iyengar, A., Koerselman, H. L., Lilienthal, A. J., Bassuk, A. G., Kitamoto, T., & Manak, J. R. (2016). Mutation of orthologouspricklegenes causes a similar epilepsy syndrome in flies and humans. *Annals of Clinical and Translational Neurology*, 3(*9*), 695–707. https://doi.org/10.1002/acn3.334
3. Nukala, K. M., Lilienthal, A. J., Lye, S. H., Bassuk, A. G., Chtarbanova, S., & Manak, J. R. (2023). Downregulation of oxidative stress-mediated glial innate immune response suppresses seizures in a fly epilepsy model. *Cell Reports*, 42(*1*), 112004. https://doi.org/10.1016/j.celrep.2023.112004

ACKNOWLEDGEMENTS

I would like to thank Brady Williquett and Dr. John Manak for their continued support, guidance, and mentorship over the course of this research project. A special thanks to The University of Iowa and Belin-Blank Honors Center for this opportunity. This research was funded by the University of Iowa Stead Family Department of Pediatrics Research Grant to J.R.M.

Working Towards Optimized Commercial Production of AAO

As a Substrate for CdTe and CdSe Electrodeposition for Use in Solar Cells

Jack Eugster, Sam Adesanoye, Jacob Fields, Syed Mubeen, PhD.

The University of Iowa

SunHydrogen

Background

- One of the major issues facing the world today is the greenhouse effect from non-renewable energy sources
- Hydrogen is one of the most abundant and efficient renewable energy sources and thus presents an enticing commercial
- Cadmium-based semiconductors such as CdSe and CdTe are commercially viable in the United States and can be used in photovoltaic cells with the intention of producing hydrogen from water (Nafaji et al., 2019).
- Currently, most commercial cadmium-based semiconductors use a closed space sublimation technique to produce a thin layer of semiconductive material on a conductive substrate (Singh et al., 2019).
- While thin films are currently cheaper to produce, they have many drawbacks when compared to a nanowire structure which can be achieved by depositing the semiconductive material on anodized aluminum (AAO)
- AAO is produced through an electrochemical system in which a working electrode of pure aluminum (anode) and a counter electrode (cathode) are submerged in an electrolyte bath and subjected to a constant voltage until the target current density is reached (Fig. 1).
- Anodizing the aluminum creates a surface network of nanopores into which CdSe or CdTe are deposited upon to create standing nanowires, which are incredibly durable in addition to being efficient due to their high surface area; essentially the AAO acts as a mold for the semiconductive material (Kapoor et al., 2019).
- This project focused on optimizing the anodization process, specifically by testing the effect of using an aluminum counter electrode as opposed to a graphite counter electrode

Figure 1 (Anodization Setup)

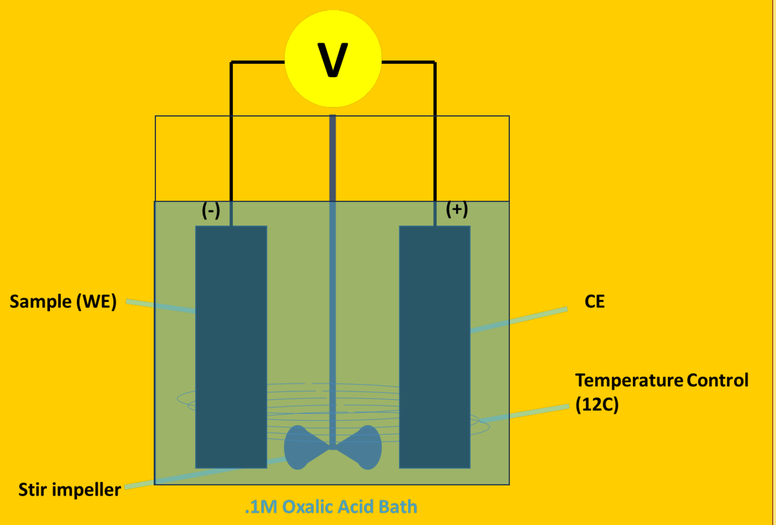

Results

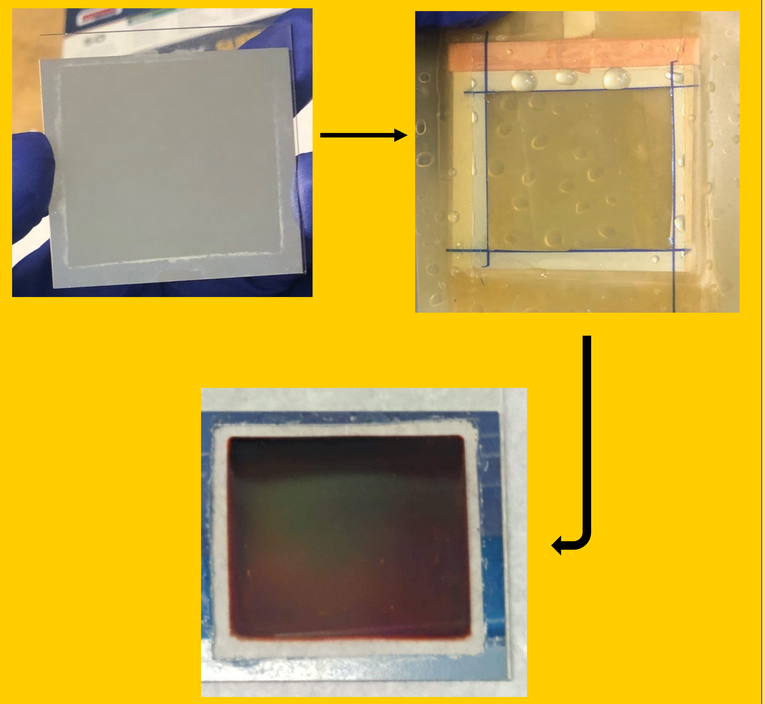

Figure 2 (Raw sample to anodization and deposition)

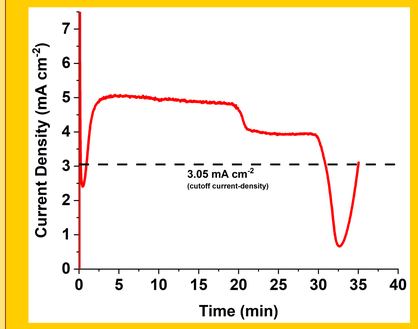

Figure 3 (Anodization curve)

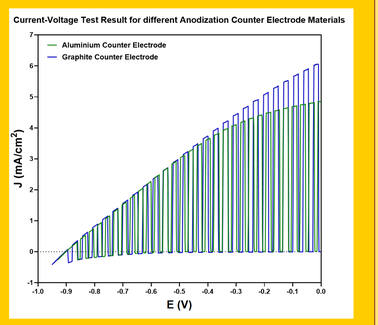

Figure 4 (PEC of samples anodized in graphite and aluminum)

Discussion

These results show a sample undergoing the typical anodization process. The initially reflective aluminum develops billions of nanopores, which results in a clear substrate. Semiconductive material is then deposited onto the sample which results in a darker color. The PEC results (Fig. 4) indicate that the samples anodized with graphite and aluminum counter electrodes did not yield significant differences in performance. This was concurrent with the hypothesis.

Next Steps

As there is no significant difference in performance, the next step in this research is to view the nanopores themselves using a high-resolution scanning electron microscope (SEM). If the nanopores show no difference in structure, the next step would be to test an aluminum oxalate buffer. The aluminum oxalate would act as a Bronsted-Lowry strong conjugate base and the solution would be highly resistant to pH changes. With both an aluminum working and counter-electrode the oxalic acid solution could maintain a high purity for many anodization runs, which would cut costs in a commercial setting.

Acknowledgements

Thanks to SunHydrogen, The University of Iowa, Belin Blank Center, the Mubeen Research Group, and Dr. Mubeen for making this research possible!

References

Kapoor, S., Ahmad, H., Julien, C. M., & Islam, S. S. (2019). Synthesis of highly reproducible CdTe nanotubes on anodized alumina template and confinement study by photoluminescence and Raman spectroscopy. *Journal of Alloys and Compounds.* https://doi.org/10.1016/j.jallcom.2019.151765

Nafaji, M., Ahmadi, R., Sham, T.-K., & Salimi, A. (2019). Electrochemical atomic layer deposition of cadmium telluride for Pt Decoration: Application as novel photoelectrocatalyst for Hydrogen Evolution Reaction. *Electrochimica Acta.* https://doi.org/10.1016/j.electacta.2019.134651

Singh, V. P., Singh, R. S., & Sampson , K. E. (2007). Thin-film solar cells based on nanostructured cds, Cis, CdTe and cu2s. *Nanostructured Materials for Solar Energy Conversion.* https://doi.org/10.1016/B978-044452844-5/50007-X

Modifying *piggyBac* transposon vectors for high efficacy Factor VIII gene transfer to mediate Hemophilia A phenotypic correction

Baochan Fan[1], Kevin Gubner[2], Danielle York[2], Janice Staber, MD[2]

[1]Hamilton High School, Chandler, Arizona; [2]Department of Pediatrics, University of Iowa Stead Family Children's Hospital, Iowa City, Iowa

Introduction

Hemophilia A

- X-linked genetic disorder affecting ~1:5000 males.
- Characterized by deficient Factor VIII (FVIII) protein levels.

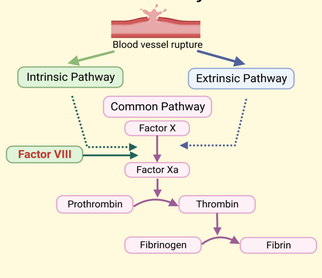

Blood coagulation cascade. FVIII is a cofactor in the pathway, initiating the conversion of thrombin for the development of the platelet-fibrin plug in response to injury.

- If Hemophilia A is left untreated, resulting hemorrhagic and excessive bleeding events may lead to death.
- **Current treatments have limitations:**
  - Intravenous FVIII protein replacement therapy: Limitations: frequent injections, costly, inhibitor formation
  - FVIII gene transfer via viral vectors:

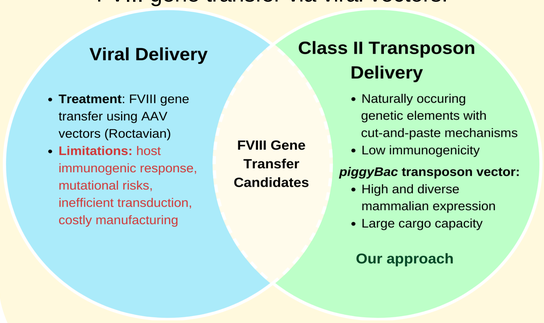

Benefits of transposon delivery over viral delivery for FVIII gene transfer.

***piggyBac* transposon-mediated gene transfer of FVIII is a promising treatment avenue for Hemophilia A.**

Objectives

- From the previously developed *piggyBac* transposon vector carrying a codon-optimized B-domain deleted human FVIII gene from more than a decade ago (**PB-coFVIII-BDD**), we re-codon-optimized the FVIII gene (**2023PB-coFVIII-BDD**).
- We corrected a sequence with the MluI restriction enzyme site (**PB-coFVIII-BDD-MluI.fix**) and engineered the *piggyBac* vector to carry the full-length FVIII insert (**PB-FLFVIII**) as vehicles for FVIII gene transfer.
- We compare FVIII activity levels between PB-coFVIII-BDD and the modified vectors in Hemophilia A mice.

Hypotheses

PB-FLFVIII
Although not required for FVIII coagulation functions, the FVIII B-domain plays crucial roles in decreasing ER stress, facilitating intracellular trafficking, and protecting against proteolysis. The inclusion of the B-domain may lead to safer FVIII gene transfer and increased activity.

PB-coFVIII-BDD-MluI.fix
PB-coFVIII-BDD has an introduced point mutation encoding for an MluI site, which could affect intracellular cleavage and FVIII activation. We hypothesize that the reversion of the mutated sequence back to the native sequence may lead to higher FVIII activity.

2023PB-coFVIII-BDD
Re-codon-optimization accommodates for up-to-date codon bias to further increase translational efficiency of the FVIII gene; thus, we expect higher FVIII activity in comparison to the older PB-coFVIII-BDD vector.

Methods

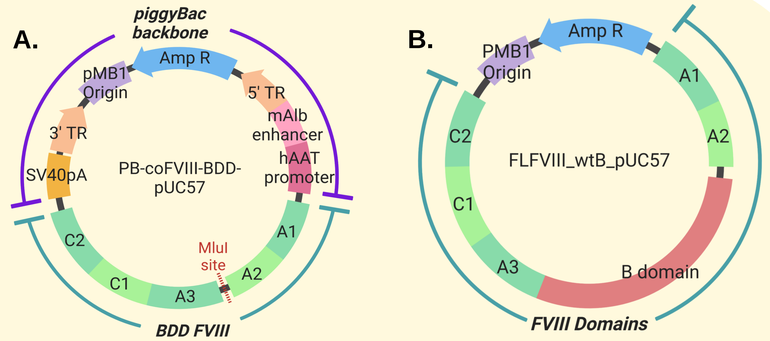

Image 1. FVIII Plasmids. A) *piggyBac* transposon vector expressing the codon-optimized FVIII gene with 14 amino acids in place of the B-domain. The MluI site of interest is shown. **B)** Full length FVIII with the A1-A2-B-A3-C1-C2 wild-type domain structure.

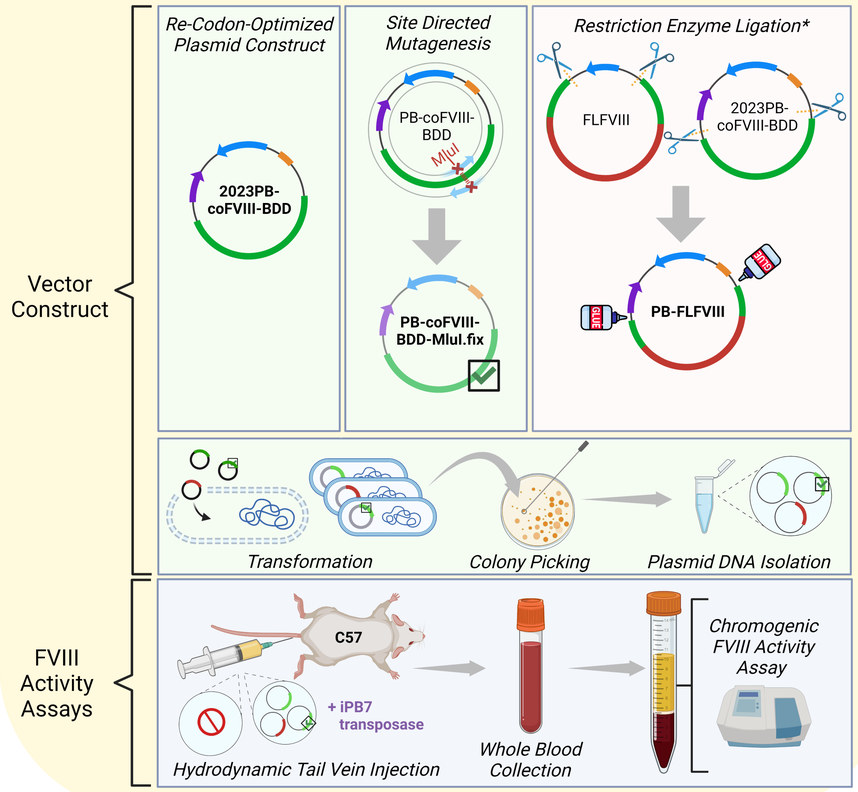

Results: Vector Construction

✓ Vector plasmid sequences confirmed via NGS following vector construction.
✓ Successful site directed mutagenesis to create PB-coFVIII-BDD-MluI.fix.
✗ Unsuccessful creation of the PB-FLFVIII vector.

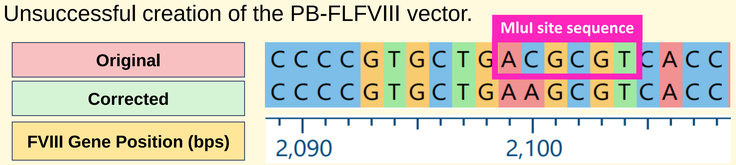

Image 2. Codon-optimized, B-domain deleted FVIII gene sequence showing successful site directed mutagenesis at base pair 2,100 in creation of the PB-coFVIII-BDD-MluI.fix vector. (Credit: Sequences were aligned and visualized using the DNASTAR Multiple Sequence Alignment program.)

Results: FVIII Activity

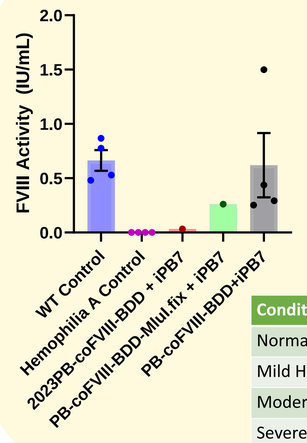

Fig 1. Hyperactive *piggyBac* transposase (iPB7) catalyzed integration of modified FVIII gene transfer vectors alters FVIII activity. The 2023PB-coFVIII-BDD and PB-coFVIII-BDD-MluI.fix vectors were delivered to Hemophilia A mice via hydrodynamic tail vein injection with a 1:1 (25 µg) vector-to-transposase injection ratio. A chromogenic activity assay was conducted to quantify FVIII activity levels from isolated plasma within three days post-injection in comparison to old PB-coFVIII-BDD vector activity. Wild type (WT) mice (C57 background) and Hemophilia A mice (C57 background) served as positive and negative controls, respectively. Data represent mean ± SEM; 1 IU/mL = 100% FVIII activity.

Condition	FVIII Activity Range (IU/mL)
Normal	>0.50
Mild HA	0.05-0.50
Moderate HA	0.01-0.04
Severe HA	<0.01

Table 1. FVIII activity ranges in relation to Hemophilia A (HA) severity level.

Conclusions

- Delivery of PB-coFVIII-BDD + iPB7 seems to increase FVIII activity levels in Hemophilia A mice back to normal, comparable to levels in wild-type mice.
- The old PB-coFVIII-BDD vector achieved greater FVIII activity than the newly modified vectors, suggesting that it confers the greatest FVIII gene transfer efficacy out of all tested vectors.

Challenges

- Restriction enzyme ligation and transformation for constructing PB-FLFVIII vectors yielded null colony counts, possibly due to the large size of the full length FVIII insert (7.1 kb) in comparison to the *piggyBac* vector (4.8 kb).
  - Next steps to take include ligating smaller sections of the insert into the vector at a time or adding dummy DNA to extend the vector backbone.

Limitations

- Small sample size per treatment in the chromogenic FVIII activity assay.
  - Because the modified vectors were tested in only one mice each, we cannot be certain of the significance of our findings from Fig 1.
- Inefficiency of vector delivery *in vivo*: hydrodynamic tail vein injections are not feasible for clinical use and is a source of variable liver delivery in mice.

Future Studies

- Conduct chromogenic FVIII activity assays over longer periods of time to evaluate the extent of FVIII expression in the long term.
- Further evaluate the prospects of Hemophilia A phenotypic correction through FVIII ELISA assays (antigen presence), aPTT tests (clotting efficiency), Bethesda assays (inhibitor formation), and tail clip assays (bleeding time).

Acknowledgements

Thank you to the Staber Lab for your generous mentorship, and the SSTP summer program for facilitating the research experience.
All images were created by the student using BioRender.com or Canva.
All graphs were created by the student using GraphPad Prism.

References

Hu, Z., Li, Z., Wu, Y., Zhao, J., Wu, L., Zhou, M., & Liang, D. (2022). Targeted B-domain deletion restores F8 function in human endothelial cells and mice. *Signal Transduction and Targeted Therapy*, 7(189). https://doi.org/10.1038/s41392-022-01016-9

Staber, Janice M, Pollpeter, M. J., Arensdorf, A., Sinn, P. L., Rutkowski, D. T., & McCray, P. B. (2014). piggyBac-mediated phenotypic correction of factor VIII deficiency. *Molecular Therapy - Methods & Clinical Development*, *1*, 14042. https://doi.org/10.1038/mtm.2014.42

Ward, N. J., Buckley, S. M., Waddington, S. N., VandenDriessche, T., Chuah, M. K., Nathwani, A. C., McIntosh, J., Tuddenham, E. G., Kinnon, C., Thrasher, A. J., & McVey, J. H. (2011). Codon optimization of human factor VIII cDNAs leads to high-level expression. *Blood*, *117*(3), 798–807. https://doi.org/10.1182/blood-2010-05-282707

Modifying Titanium Felt via Electrochemical Nitridation for Improved Electrocatalytic Performance during Oxygen Evolution Reaction

Ashley Fu [1], Prasoon Kumar [2], Abdulsattar H Ghanim PhD [2], Syed Mubeen PhD [2]

[1] Chaparral High School, AZ, [2] Department of Chemical and Biochemical Engineering, University of Iowa

Introduction

Water electrolysis ($2H_2O \rightarrow 2H_2 + O_2$) is highly regarded for its ability to transform renewable energy into green hydrogen fuel.
In acidic media, two half-cell reactions occur:

- Hydrogen evolution reaction (HER): $2H^+ + 2e^- \rightarrow H_2$
- **Oxygen evolution reaction (OER): $2H_2O \rightarrow O_2 + 4H^+ + 4e^-$**
  - Sluggish kinetics and the instability of available catalysts.
- Highly oxidative environment for supports (i.e., Ti, C, ATO).
  - Increases resistance.
  - Lowers activity and stability.
- Substrate can be coated with Au, Pt, or Ir to improve electrocatalytic performance.
  - Cost and availability of material is a concern.
- Electrochemical nitridation to coat Ti with TiN.
  - Good adhesion properties.
  - Lowers resistance.
  - Prevents TiO_2 formation.

Purpose

This study aims to investigate the effect of electrochemical nitridation on the overall electrocatalytic performance of iridium-based water oxidation catalysts.

Method

Sonicating:

1. Ti-felt was sonicated in C_3H_6O, CH_3OH, C_3H_8O for 20 minutes to remove organic impurities.
2. Ti-felt was sonicated in ultra-pure water for 20 minutes to remove inorganic impurities.

Etching:

1. Ti-felt was etched in concentrated HNO_3 for 45 minutes.

Electrochemical Nitridation:

1. Etched Ti-felt was electrochemically nitridated in 0.1M HNO_3 + 0.5M KNO_3 for two hours.

Electrodeposition

1. Electrochemically deposited Ir onto the TiN

Electrochemical Testing Techniques

- PEIS, LSV, CV

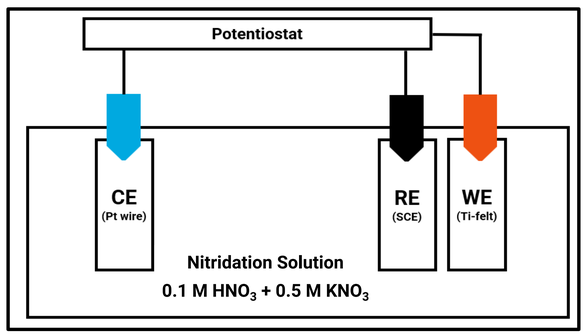

Fig 1. TiN samples were made and analyzed using a three-electrode system with a Pt wire counter electrode and a Hg/HgCl reference electrode.

Results

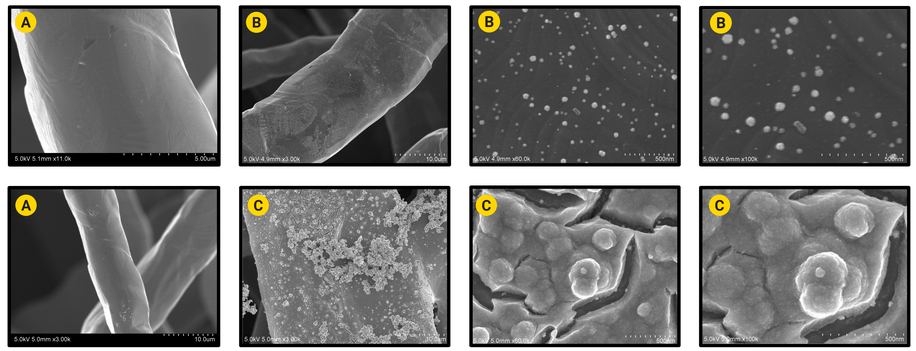

Fig 2. Sample A is a bare Ti-felt. Sample B was etched for 45 min. in HNO_3 and nitridated for two hours. Sample C had the same conditions as Sample B, but Ir was deposited on it and tested using LSV and CV (25 cycles) at a scan rate of 20 mV/s.

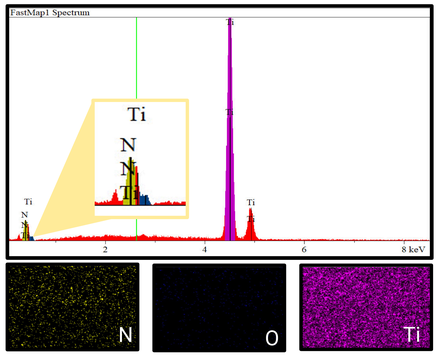

Fig 3. EDX elemental analysis of sample B (Fig 2) at x100K magnification.

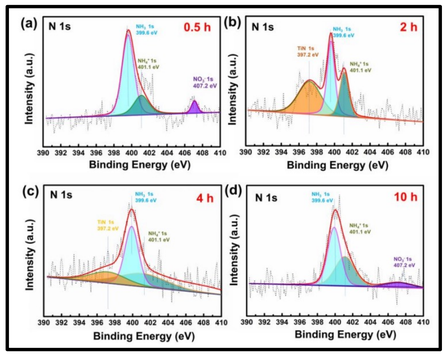

Fig 4. XPS of TiN formation at various nitridation periods (0.5, 2, 4, 10 h).[3]

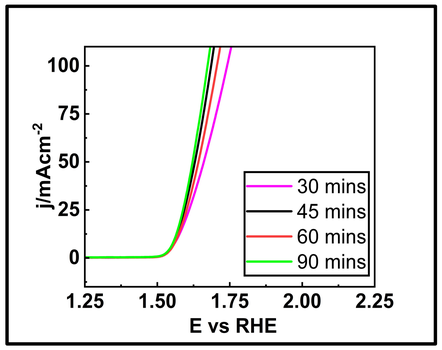

Fig 5. Polarization curves of IrO_x/TiN samples etched in HNO_3 at different times (30, 45, 60, 90 mins)

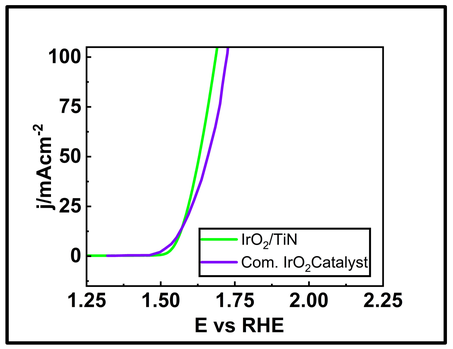

Fig 6. OER activity comparison of a IrO_x/TiN catalyst and a commercially available IrO_2 catalyst

Conclusions

- Samples etched for 45 and 90 minutes in concentrated HNO_3 performed similarly (**Fig 5**).
  - Higher activity and lower resistance.
  - Does not create enough roughness for effective Ir deposition.
- XPS of nitridated samples concluded that two hours of nitridation formed the highest amount of TiN (**Fig 4**).
  - TiN converts to NH_4^+ and NO_3^- as nitridation time increases.
- EDX confirmed the formation of TiN via electrochemical nitridation (**Fig 3**).
- After 25 cycles of OER activity testing at a scan rate of 20 mV/s, iridium begins to crack and fall off (**Fig 2**).
  - Indicates significant activity, but lack of stability
  - The similar surface structure of sample A and B lacks nanoscopic roughness
- IrO_x/TiN was found to be better in terms of electrochemical activity than commercially available IrO_2 catalysts (**Fig 6**).

Future Directions/Implications

- Etching Ti-felt in diluted HF or HCl may improve the electrochemical adhesion of the catalyst by creating more roughness.
  - HNO_3 does not provide enough surface area for Ir deposition.
  - Etching time in diluted HF and HCl must be explored.
- TiN is a robust material
  - Can be used to form dimensionally stable OER electrocatalysts under extreme oxidative conditions

Acknowledgments

Special thanks to Dr. Syed Mubeen, Prasoon Kumar, and the entire Mubeen lab for their patience and guidance necessary to complete this project. I would also like to thank the Belin-Blank Center for creating this amazing opportunity.

References

1. Cukman, D., & Vukovic, M. (1990). Electrochemical behavior of an electrodeposited iridium electrode in acid solution. *Journal of Electroanalytical Chemistry*, 279(1), 283–290. https://doi.org/10.1016/0022-0728(90)85183-6
2. Gao, J., Liu, Y., Liu, B., & Huang, K.-W. (2022). Progress of heterogeneous iridium-based water oxidation catalysts. *ACS Nano*, 16(11), 17761–17777. https://doi.org/10.1021/acsnano.2c08519
3. Liu, Y., Huang, S., Wang, D., Zhang, H., Shan, D., Peng, S., Shen, G., Wang, L., & Wang, X. (2022). Modifying Ti-based gas diffusion layer passivation for polymer electrolyte membrane water electrolysis via electrochemical nitridation. *ACS Applied Materials & Interfaces*, *14*(13), 15728–15735. https://doi.org/10.1021/acsami.1c22639
4. Reier, T., Oezaslan, M., & Strasser, P. (2012). Electrocatalytic oxygen evolution reaction (OER) on Ru, Ir, and Pt catalysts: a comparative study of nanoparticles and bulk materials. *ACS Catalysis*, 2(8), 1765–1772. https://doi.org/10.1021/cs3003098
5. Wu, D., Wang, X., & Wu, X. (2022). A study on the anodic electrodeposition of iridium oxide on different substrates. *Journal of the Electrochemical Society*, 169(9), 92503. https://doi.org/10.1149/1945-7111/ac8cb9

The Role of B-Cells in Granuloma Formation *in vitro*

A. Gowder, M. Hagner, L. Powers, T. Titterington, G. Necker, B. Bettis, N. Ganasemer, N. Hamzeh, A.A. Pezzulo
Department of Internal Medicine, Roy J. and Lucille A. Carver College of Medicine, The University of Iowa

Introduction: Sarcoidosis is a granulomatous disease

- Highly challenging to diagnose and treat
- Due to inhalation exposure in a susceptible host
- Characterized by noncaseating granuloma formation
- Granulomas can be modeled with immune cells in blood from patients with latent tuberculosis infections (LTBI) and sarcoidosis
- Cell types and mechanisms involved in the formation of these granulomas is poorly understood

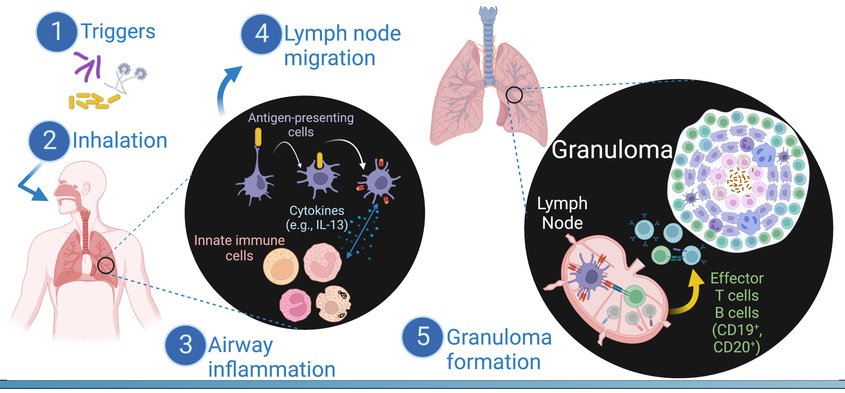

Hypothesis:

B-cell ($CD19^+$, $CD20^+$) depletion will cause a significant decrease in the granuloma formation observed in patients with LTBI

Experimental Approach:

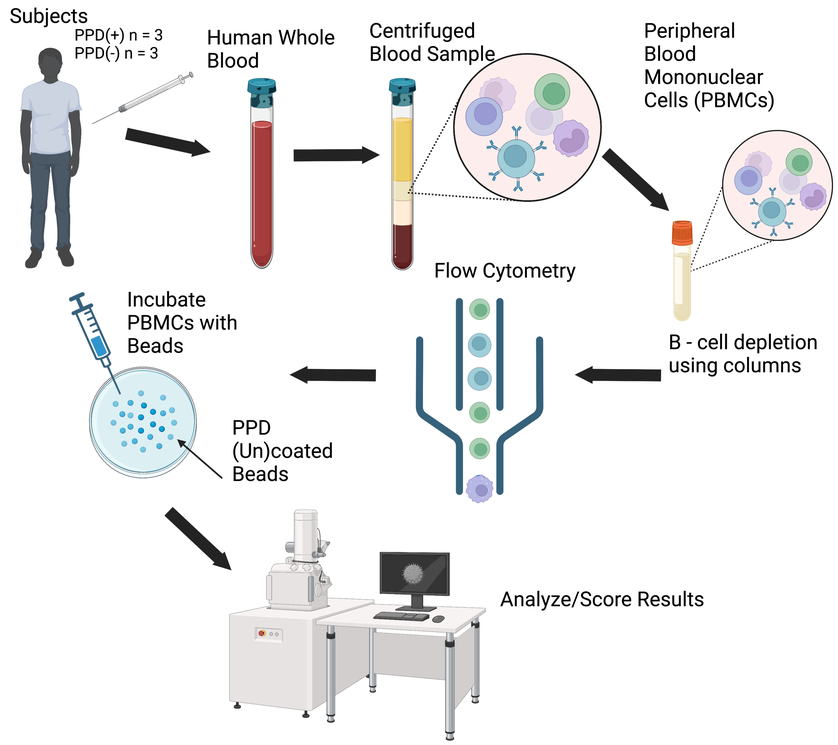

PBMCs from LTBI patients form granulomas *in vitro*

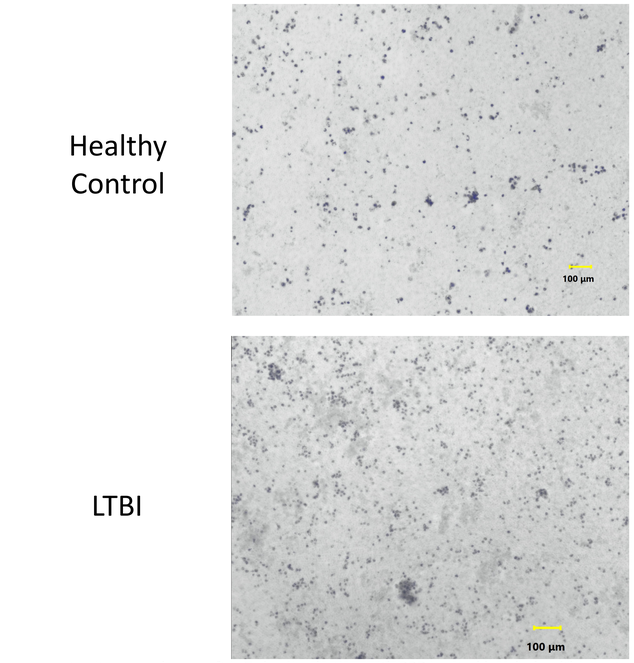

In vitro granulomas after 7-day incubation with PPD-coated beads, healthy control vs. LTBI sample. LTBI sample has granuloma formation and significantly more cellular aggregation than healthy control sample. n = 1

Freezing/Thawing does not affect granuloma formation in LTBI patients

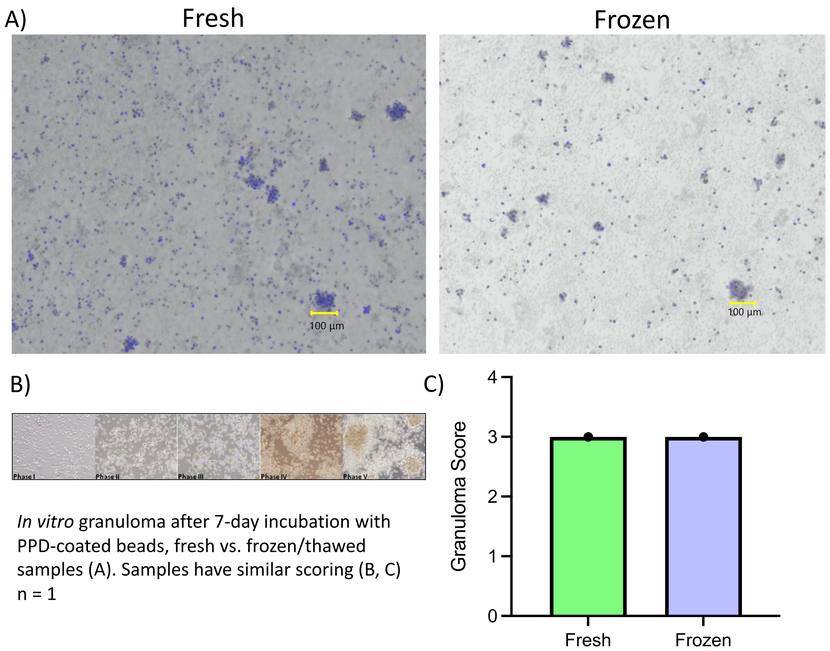

In vitro granuloma after 7-day incubation with PPD-coated beads, fresh vs. frozen/thawed samples (A). Samples have similar scoring (B, C) n = 1

B-cells are not essential for granuloma formation

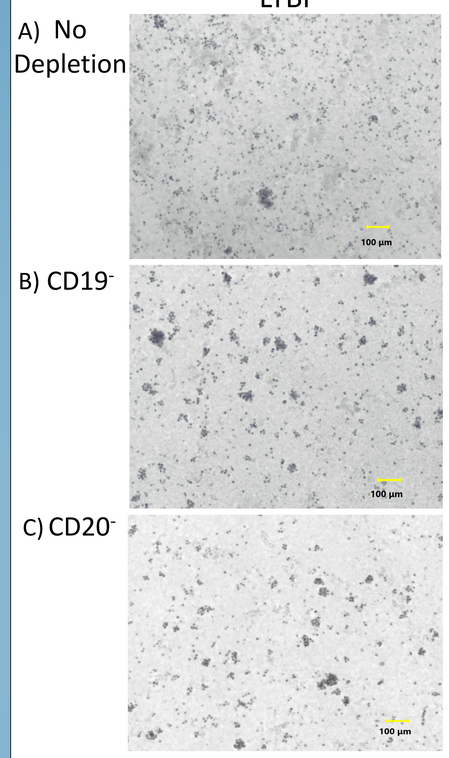

No Depletion sample has a few large and robust granulomas (A). CD19- sample has many more cellular aggregates that are generally smaller in size (B). CD20- sample has similar frequency and size of cellular aggregates to CD20- depletion (C).

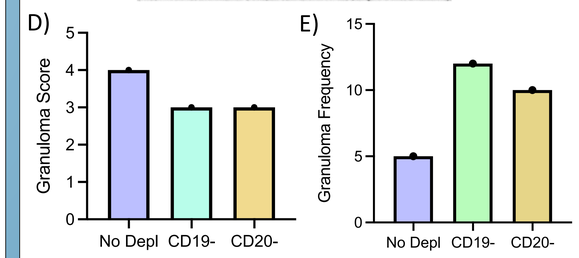

Bar Graphs show the difference in Granuloma Score between No depletion, CD19-, and CD20- (D) and difference in number of granulomas present (E).

Summary/Conclusion

- PBMCs from LTBI patients form robust granulomas when incubated with PPD coated beads
- Freezing and thawing process does not affect granuloma formation in model
- CD19 and CD20 B cells do not appear to be essential in LTBI granuloma formation *in vitro*
- PBMCs from LTBI patients, in the absence of CD19 and CD20 B cells, form smaller and more numerous granulomas when exposed to PPD coated beads
- The addition of granuloma frequency to granuloma size scoring may provide further insight into the role B cells are playing in granuloma formation

Contact: **arjungowder@gmail.com**

Project supported by:
-Ann Theodore Foundation Sarcoidosis Initiative
-NHLBI K01HL140261
-NHLBI R01HL163024
-Cystic Fibrosis Foundation K-boost and Iowa RDP

We thank our research subjects for participating and the Carver College of Medicine Cells and Tissue Core for excellent support.

PARAMETRICALLY-GENERATED SOLAR CONCENTRATORS:
METHODOLOGY, SIMULATION, AND TESTING

Contributors: Sebastian Hazlett, Reyna Alam, Dorothy Zhang, Leonard Maxwell. **Research Mentors:** Associate Professor Dr. Fatima Toor, Daniel Keefe, Rezwan Mohammed Sayeed.

Introduction:

Solar Concentrators found to increase solar cell efficiency by:

1. **Reducing reflections** in solar cell surface, busbars, and metal fingers
2. Increasing distance traveled/**absorbance for longer wavelengths** without increasing solar cell thickness
3. **Suppressing radiative recombination** (Hu *et al.*, 2023)

The purpose of this study was:

– 1. To **integrate** the most up-to-date research on solar concentrator **geometry, design, 3D printing, and reflective coating** to **construct** an **efficient small solar concentrator system** within 5 weeks.

– 2. To **refine** previous **scientific methodologies** in doing so.

Methods:

OpenSCAD Scripting Details:

OpenSCAD is **a programmatic CAD toolkit** by which **script code** generates **3D models.** Used math of Cooper et al. to generate **polygonal parabolic compound concentrator (PPCC) 3D models** via OpenSCAD scripting (Cooper *et al.,* 2013). OpenSCAD scripts for each of the **individual concentrator variations** (see **Fig. 1**) **automatically generated from template file via a shell script.**

Optical Simulations of Concentrators Via Radiance:

We used an **open-source command-line ray-tracing software** called **Radiance** to simulate top-down (**0° acceptance angle**) sunlight hitting our concentrators (loaded into the program via **STL models** exported from OpenSCAD).

The ray-tracing scenarios thus described followed **instructions in shell files** executed by Radiance, with lux results **in W/m^2 exported to High-Dynamic-Range (HDR) image files.**

3D Prints & Reflectivity Testing:

3D-printed 12 concentrators listed in **Fig. 2,** chemically smoothed them w/XTC-3D coating. Metals sprayed on 3D-printed, smoothed flat pallets. Controls set as default smoothed pallets**. Chromium most reflective, 70-77%.** Sprayed our twelve concentrators in Chromium.

Solar simulator:

Tested concentrators under **PV Measurements small-area solar simulator** using **Sunnytech 3.19" x 2.91" x 0.51" solar mini-module** using setup below. **Control solar cell current density** (*no concentrator, just 10-mm radius aperture*) was **0.0345 mA/cm^2.**

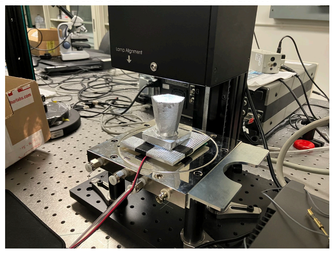

Fig 1: Concentrator Testing Setup

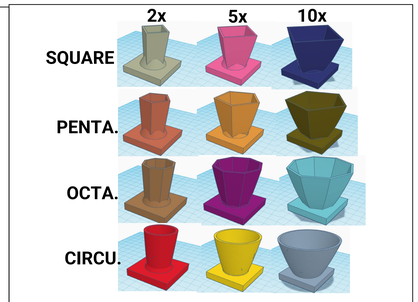

Fig. 2: 3D Polygonal Parabolic Concentrators Generated Using OpenSCAD Scripting (height=60mm, radius-bottom=10mm)

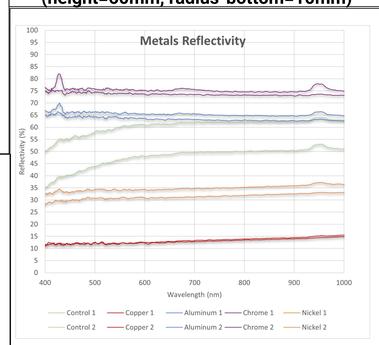

Fig. 5: Reflectivities of metals sprayed onto smoothed 3D-print pallets (control = smoothed pallets, no spray).

Fig. 6: OpenSCAD & MATLAB code base for concentrator generation and testing.

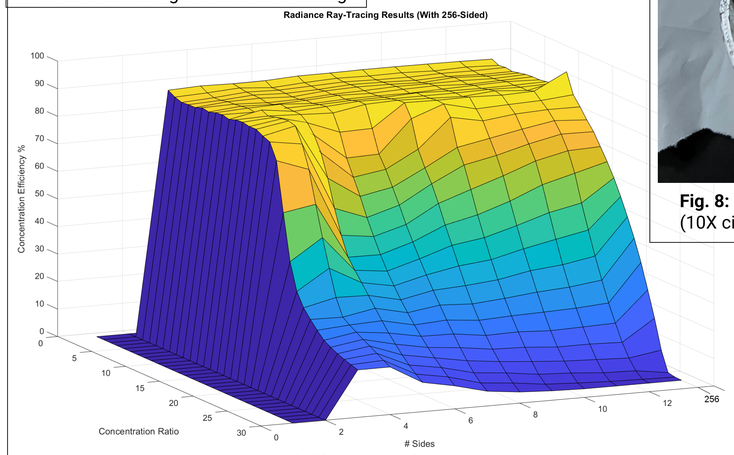

Fig. 7: Optical efficiencies of concentrators according to Radiance ray-tracing simulation results

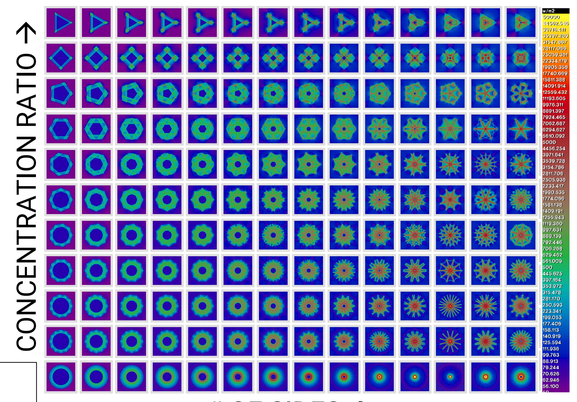

Fig. 3: Radiance Ray-Tracing Luminosity Results for Concentrator Matrix 3 Sides->256 Sides x 2X->13X (= higher lux, = lower lux)

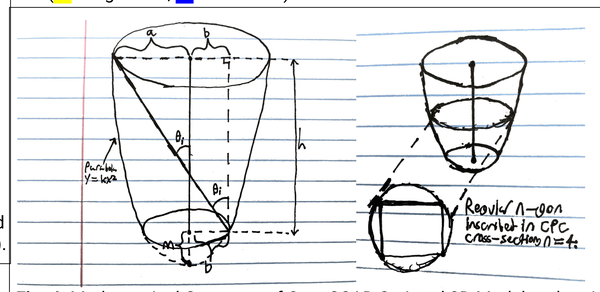

Fig. 4: Mathematical Geometry of OpenSCAD Scripted 3D Models, wherein $(1)\ a+b=h*tan(\Theta_i)\ (2)\ m=kb^2\ (3)\ h+m=ka^2$ and $(4)\ h=k(a^2-b^2)$

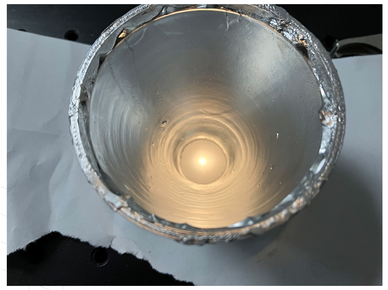

Fig. 8: Solar Simulator testing light pattern (10X circular parabolic concentrator).

Results:

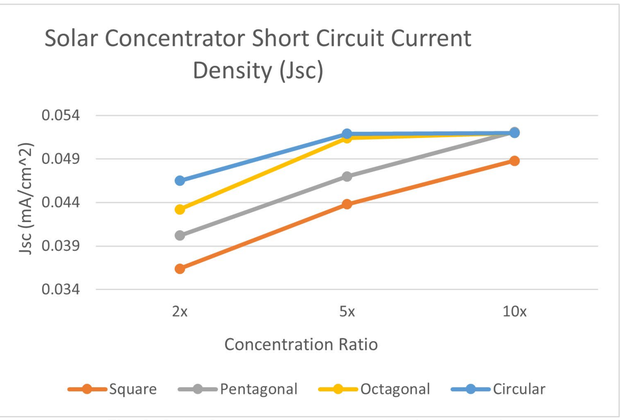

Fig. 9: Solar Concentrator current density generation results from solar simulator tests seen in **Fig. 1.**

Analysis:

Cooper *et al.* vindicated by n->infinity superior light concentration performance for PPCCs. 5X and 10X Pentagonal PPCCs more effective than 5X and 10X square PPCCs**, vindicating Radiance tests but contradicting Cooper *et al.*'s findings.**

Radiance tests have 2X pentagonal as lower-performing relative to 2X square PPCCs. **Solar simulator results have opposite.**

Radiance also estimates circle performance **incorrectly** as lower than 8-sided PPPCs for 2X and 5X. However, **Radiance correctly estimates superior 10X circular performance versus 8-sided PPCC.**

Finally, Radiance estimates **a ring-shaped area of greatest luminosity** within the concentrator apertures, whereas the solar simulator clearly **shows a circle-area of greatest luminosity**. Most likely **surface imperfections not modeled in Radiance caused the light reflections to "diffuse" into this circle.**

Conclusion:

Our tests confirmed the repeatability of much of Cooper et al.'s work. However, divergences between different modes of testing (**digital and physical**) and from literature **suggest the desirability of a greater standardization and refinement of methodology** than even the significant progress we have made in the pursuit of such.

Acknowledgements:

Gracious thanks to the Belin-Blank Center, Toor Lab, Research Mentors for scientific and presentational guidance!

References:

Cooper, T., Dähler, F., Ambrosetti, G., Pedretti, A., & Steinfeld, A. (2013). Performance of compound parabolic concentrators with polygonal apertures. *Solar Energy*, *95*, 308-318.

Hu, T., Zhang, M., Mei, H., Chang, P., Wang, X., & Cheng, L. (2023). 3D Printing Technology Toward State-Of-The-Art Photoelectric Devices. *Advanced Materials Technologies*, *8*(4), 2200827.

IOWA

Unlocking the Cellular Gateway: Unraveling Superior Transfection Techniques

Junning Hu[1], Mikhail Vasilyev MD[2,3], Guiru Ma MD[5], Anastasiia Vasileva MD[2,4], Michael H. Tomasson MD[2,3,4], Melissa L. Bates PhD[2]

Department of Biology, Western Reserve Academy, Hudson, OH[1]; Department of Internal Medicine[2], Division of Hematology, Oncology, and Bone Marrow Transplantation[3], Health and Human Physiology[4], Department of Molecular Medicine[5], University of Iowa, Iowa City, Iowa, USA

Introduction

Multiple Myeloma (MM) is a type of B lymphocyte cancer. A common mutation t(4;14) occurs in around 25% of MM patients[1]. NSD2 gene is highly expressed due to this mutation[2]. Previous study shows that different sequences of NSD2 translocated can impact the mortality rate of MM patients[3]. However, most of them were done by knocking out the gene instead of knocking in. Our project aims to study whether different sequences of NSD2 translocated impact the protein stability and patient mortality through gene insertion. Retrovirus is a type of virus that can integrate the cDNA of its RNA into host cell genome and produce its own copy shown in figure 1. Retrovirus's ability to modify gene permanently[4] and efficiently makes it a common gene editing tool. Thus, we used Murine Stem Cell Virus (MSCV), a type of retrovirus, to insert different variants of NSD2 gene into B cells. For the establishment of methodology, we compared three transfection methods, lipofectamine, calcium phosphate, and PEI, shown in table 1, to find the most efficient method to produce MSCV.

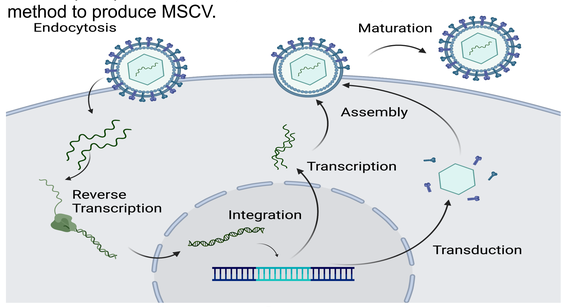

Figure 1: Retroviral Life Cycle[5]. The early stage and late stage of retrovirus replication cycle is shown.

Hypothesis

Lipofectamine will have the higher transfection efficiency for the transfection of MSCV IRES GFP NSD2 Full length plasmid (10,824 bp) into HEK293T cells compared to Calcium Phosphate and PEI.

Methods

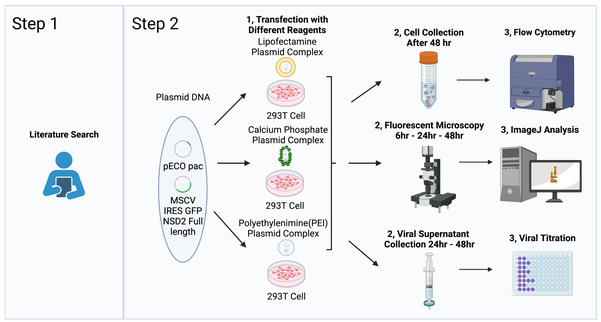

Figure 1: Experiment Overview. Virus and packaging plasmid were co-transfected with Lipofectamine 3000, Calcium Phosphate, and PEI into the target cells. Then, the GFP expression was observed using fluorescent microscope periodically, and viral supernatant was collected at certain timing. The images taken were analyzed by ImageJ[6]. After that, the cell will be collected and sent to flow cytometry to quantify GFP expression. The viral supernatant collected will be used for viral titration to determine the titer for future transduction.

Table 1: Overview of transfection methods[7]

Transfection Methods						
Method	**Virus**	**Biolistic**	**Microinjection**	**Lipofection (Lipofectamine)**	**Cationic Polymer (PEI)**	**Calcium Phosphate**
Cell Type	In vitro and vivo cells	In vitro and vivo cells	In vitro cells	In vitro and vivo cells	In vitro and vivo cells	In vitro cells
Benefit	Stable transfection	Time efficient	High efficiency	High efficiency	Cost effective	Inexpensive; High efficiency
Limitation	Possible Genotoxicity	High cost; Possible cell damage	Maximum of 100-200 cells	Limited cell types	Possible toxicity	Influenced by pH

Note. This table, conducted as a result of literature review, shows the common transfection methods.

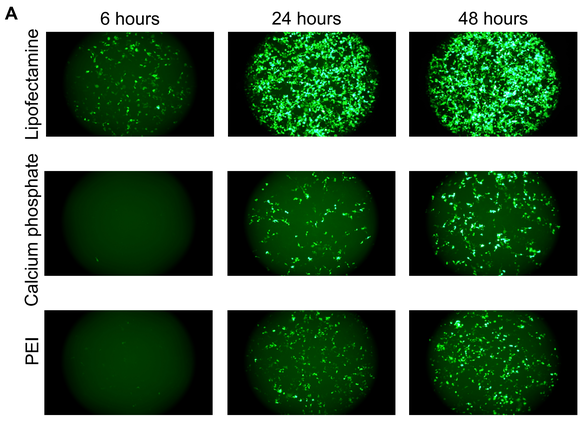

Figure 2: GFP expression in HEK293T cells. (A) Virus plasmid MSCV IRES GFP NSD2 Full length was co-transfected with packaging plasmid Eco pac in HEK293T cells with Lipofectamine 3000 (n=3), Calcium phosphate (n=3), or PEI (n=3), and cells were observed under fluorescent microscope. **(B)** The percentage and growth of GFP positive cells in HEK293T cells is measured by fluorescent microscopy and ImageJ[6]. The result is analyzed by ANCOVA test.

Results

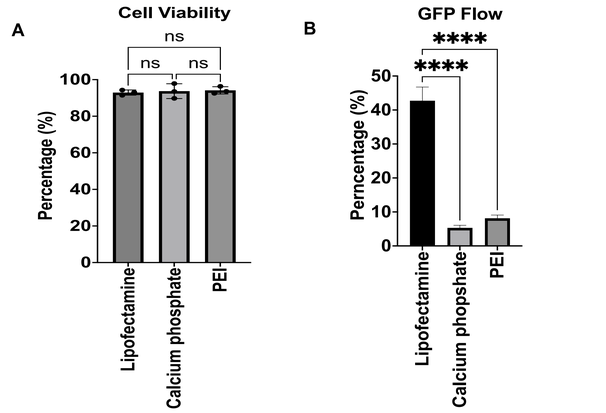

Figure 3: Cell Viability and GFP+ percentage of HEK293T cells. (A) The cell viability is measured by light microscope and trypan blue; the result is analyzed by one-way ANOVA followed by Bonferroni's multiple comparisons test. **(B)** The GFP positive cells after 48 hours is measured by flow cytometry and analyzed by one-way ANOVA and Bonferroni's multiple comparisons test.

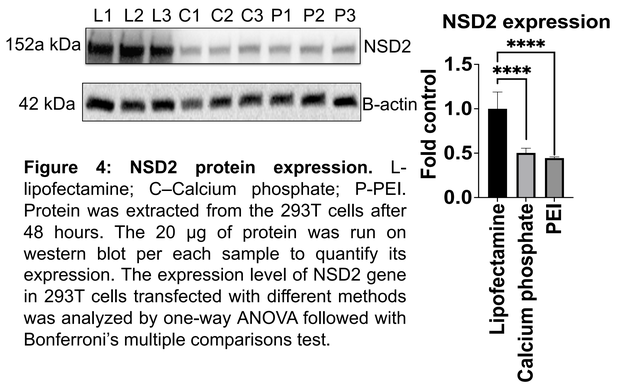

Figure 4: NSD2 protein expression. L-lipofectamine; C–Calcium phosphate; P-PEI. Protein was extracted from the 293T cells after 48 hours. The 20 μg of protein was run on western blot per each sample to quantify its expression. The expression level of NSD2 gene in 293T cells transfected with different methods was analyzed by one-way ANOVA followed with Bonferroni's multiple comparisons test.

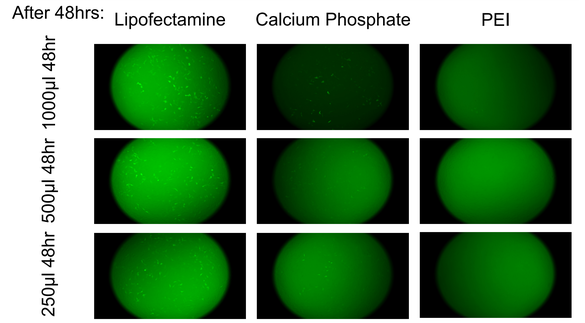

Figure 5: GFP expression under fluorescent microscopy. The 3T3 cells were transduced by MSCV produced with Lipofectamine 3000 (n=3), Calcium Phosphate (n=3), and PEI (n=3). GFP positive cell was recorded by fluorescent microscopy and counted by ImageJ[6].

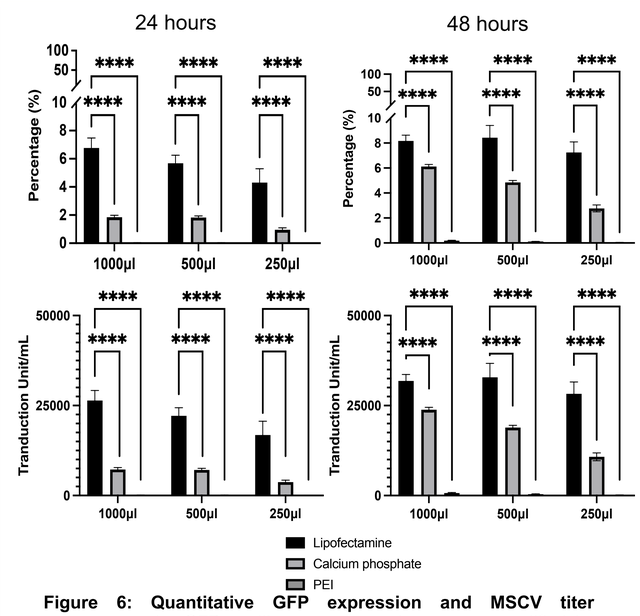

Figure 6: Quantitative GFP expression and MSCV titer measurements. GFP positive cells percentage were quantified by flow cytometry. The transduction unit per ml(TU/ml) was calculated using data from flow cytometry. GFP positive percentage and Viral titers were analyzed by two-way ANOVA and Bonferroni's comparisons test.

Conclusions

- HEK293T cells transfected with MSCV IRES GFP NSD2 Full length plasmid by lipofectamine has the highest transfection efficiency.
- All three methods have little cytotoxicity to HEK293T cells.
- MSCV produced by lipofectamine has the highest infection and transduction efficiency.
- The transduction efficacy has a positive correlation with volume of viral supernatant used.
- Viral supernatant collected after 48 hours has a higher transduction efficiency

Limitations

- The measurement of GFP+ cells by ImageJ can possibly produce imprecise results. Another cell counting software Cellprofiler developed by broad Institute will be used to improve the counting measurement.
- The viral supernatant will only be collected after 48 hours to increase the viral concentration.
- The experiments will be repeated in a larger scale to gain more accurate results and in more cell types to check the commonality

Acknowledgement

I would give my greatest thanks to Dr. Vasilyev, Dr. Ma, Dr. Tomasson, Dr. Bates, Dr. Vasileva, and rest members of IPG lab for offering me such a great learning experience. I would also thank SSTP for this precious opportunity.

References

Integrating VR and GPT-4 AI Paradigms for Augmenting Hydroinformatics Education, Research, and Operation

Anish Jain, Yusuf Sermet, Ramteja Sajja, Ibrahim Demir

Motivation

- Leverage cutting-edge technologies to foster a more **comprehensive learning experience** for flood researchers and students
- Improve operational personnel's capability to analyze data, monitor ongoing developments, and **make informed decisions in real-time**
- Provide a platform for seamless **communication** and knowledge sharing within the UIHI Lab

Introduction

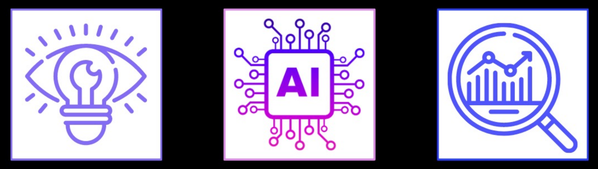

Virtual Reality Hydroinformatics Hub

Artificial Intelligence Chatbot

Real-Time Dynamic Data Feed

Methodology

- Utilize **WebXR API** to allow the development of the UIHI VR world using javascript
- Inference and implement a **multimodal language model** (GPT-4) for users to interact seamlessly using speech-to-text APIs
- Design **functional hubs** for Conferencing, Twitter Feeds, Research, and Brainstorming
- Optimize for commercial VR Headsets (e.g. Oculus, Holo Lens, etc.)

Preliminary Results/Prototype

Welcome Room - UIHI Engineering

Research Room - GPT-4 AI Assistant

Conferencing Room - IFIS Tracking

Twitter Room - Live Flood Updates

Outcomes/Discussion

- **Streamline** and improve the efficacy of **Hydrology research**
- Bridge gap between academia, research, and industry through a one-stop virtual hub
- Promote **interdisciplinary research** (Computer Engineering, Environmental Sciences, Hydroinformatics)
- Transcend traditional boundaries in education through technology
- Empower **global research collaboration** and environmental stewardship

Future Work

- Integrate **multi-user functionality**, facilitating collaborative learning for students
- Add an adaptive **"VirtualTA"** that could generate learning materials for hydrology and engineering students
- Create Research Rooms with interactive 3D models of the UIHI Lab's latest technology
- Host Virtual **Symposia** in the Conferencing Center

Acknowledgements

Special Thanks to:

- Belin-Blank Center and SSTP for providing the research opportunity
- Dr. Ibrahim Demir and UIHI Lab for mentorship and guidance
- Ramteja Sajja and Yusuf Sermet for aid in debugging/development
- Mozilla's HelloWebXR for World Template - https://hubs.mozilla.com/labs/
- Canva for design interface/iconography - https://canva.com

Effects of Numerical and Nonnumerical Magnitudes on Number and Area Discrimination in Pigeons

Jonathan Jose[1], Francisca Diaz[2], Edward Wasserman, Ph.D[2]
[1]Carroll Senior High School, [2]Department of Psychological and Brain Sciences, The University of Iowa

Introduction

Humans and animals alike use number to make complex decisions. Many theories aim to explain this fact. The Approximate Number System (ANS) proposes that organisms have evolved specialized mechanisms to process number (Brannon & Merritt, 2011). The Sensory-Integration model proposes that non-numerical magnitudes influence the behavioral control by number and that there is no specialized system to process number (Gebius, Kadosh, & Gevers, 2016).

To decide between these alternative theories, we trained pigeons in a discrimination task where size, area, and number were manipulated to see their differential impact on pigeon's discrimination.

Methods

Pigeon subjects (n=2) were trained in an experimental box (Figure 2) to discriminate the S+ (center of grid array; 9a/12n) from S- (anything but the center). The pigeons had experience with unrelated experiments and were kept to 85% of their free-feeding body weight.

Figure 2. Experimental Pigeon Box

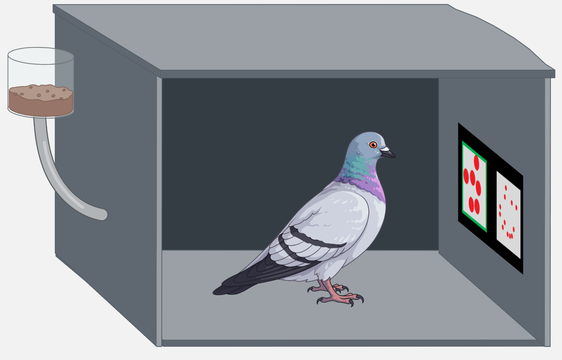

Created with BioRender

Figure 3. Trial Example

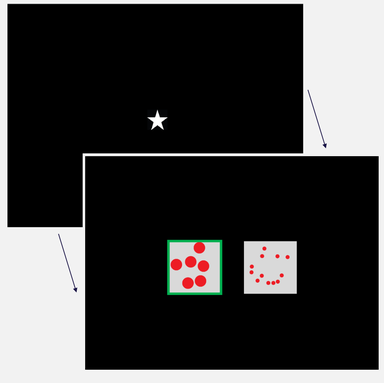

Procedures

Pigeons were trained in a 2-AFC discrimination task.

On each trial, a peck to the starting stimulus presented 2 response options on either side of the screen. Correct responses were reinforced with food pellets, but incorrect responses weren't.

Stimulus Matrix

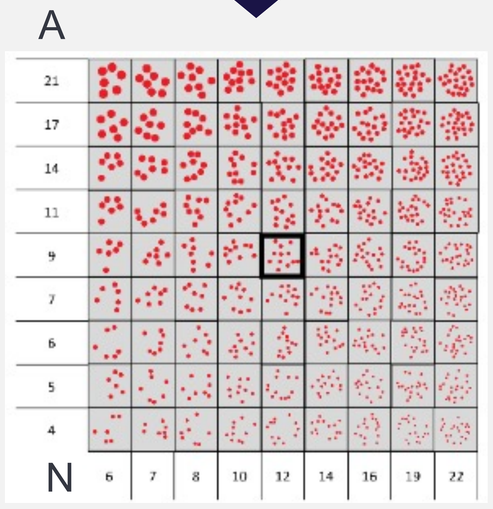

Figure 1. Full Matrix

The pigeons completed 160 trials per day, with the correct stimuli staying consistent as the center through the duration of the final experimental period. The x axis represents **number**; and the y-axis represents **area.** Hence, the middle of the 9x9 display would be 9 area by 12 number.

Results

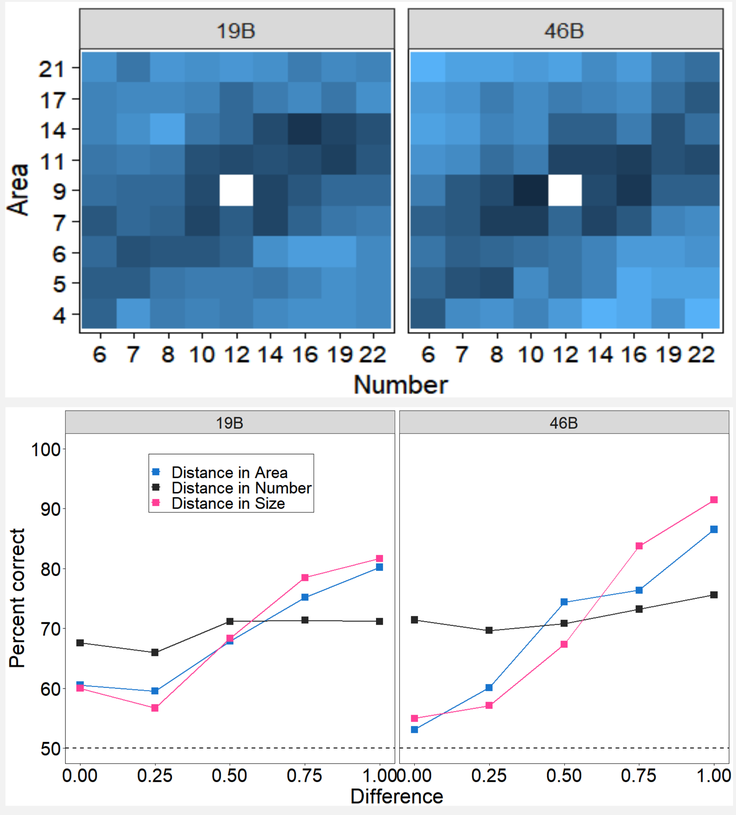

Figure 4. Accuracy Density Chart: This density chart represents the accuracies to each of the S- compared to the S+. Darker colors represent lower accuracy as the birds had a harder time distinguishing those squares from the center. As expected, on average, the darker squares concentrate closer to the center, which indicates that the birds had a harder time distinguishing squares like the center than squares dissimilar from it.

Figure 5. Size, Area, and Number: The 3 distinct lines represent changes accuracy as a function of differences in area, number, and size between the S+ and S-. The steepest and clearest lines are size and area, followed by number (which has a very flat line), symbolizing that size and area (nonnumerical) are relatively the most important out of the 3 magnitudes.

Conclusion

Overall, we saw that **nonnumerical magnitudes (size, area)** have more of an impact on number discrimination than **numerical magnitudes (number).** Further research should be focused on how these magnitudes **interact** and their importance in **other species, like humans** (Lourenco & Aulet, 2023).

Reference

Brannon, E. M., & Merritt, D. J. (2011). Evolutionary foundations of the approximate number system. *In Space, Time, and Number in the Brain,* 207–224. https://doi.org/10.1016/b978-0-12-385948-8.00014-1

Gebuis, T., Kadosh, R. C., & Gevers, W. (2016). Sensory-integration system rather than approximate number system underlies numerosity processing: A critical review. *Acta Psychologica*, *171*, 17–35. https://doi.org/10.1016/j.actpsy.2016.09.003

Lourenco, S. F., & Aulet, L. S. (2023). A theory of perceptual number encoding. *Psychological Review*, *130*(1), 155–182. https://doi.org/10.1037/rev0000380

Examining Differences Between Self-reported and Collateral Reports of Depression in Patients with Brain Lesions

Seunghyeon Kim[1], Amber Thomas, MA[2] , Aaron Boes, MD, PhD[3,4,5,6], Daniel Tranel, PhD[2,3]

[1] St. Mark's School, MA; [2] Department of Psychological and Brain Sciences, University of Iowa, Iowa City, IA; [3]Department of Neurology, University of Iowa, Iowa City, IA; [4]Department of Psychiatry, University of Iowa, Iowa City, IA; [5]Department of Pediatrics, University of Iowa, Iowa City, IA; [6]Iowa Neuroscience Institute, University of Iowa, Iowa City, IA

Background

Diagnosing depression is often dependent upon a patient's own report of their symptoms. Depression can also be measured by a collateral who knows the patient well, or a clinician. However, past studies have reported significant discrepancies between self and collateral reports of depression (Chopra et al, 2008). Particularly in patients with dementia, lower self-ratings in comparison to collateral and clinician ratings of depression was related to impaired insight (Ott et al, 1992, Burke et al., 1998). However, this difference has not been thoroughly examined in patients with brain damage.

Research Objective

The purpose of this study was to examine differences between self-reported and collateral reports of depression in patients with brain lesions and determine if insight plays a significant role in discrepant ratings. Patients with lower self-reported depression scores than collateral reports were hypothesized to have significantly impaired insight.

Methods

Participants were 138 patients from the Iowa Neurological Patient Registry. They were divided into four groups (Lowlow, Lowhigh, Highlow, Highhigh) based on their self-reported scores then their collateral reports of symptoms of depression (ex. Lowhigh group includes patients with low self-reported depression symptoms and high collateral reports)

1. **Self-reported depression** symptoms were measured with the **Beck Depression Inventory (BDI)**
   - Self-reported depression ratings were considered high when BDI was greater than 19.
2. **Collateral reported depression** and insight was measured with the **Iowa Scales of Personality Change (ISPC)**
   - Collateral rated depression and insight scores were considered high when ISPC ratings were greater than 4

Scan for sample demographics and lesion information by groups

SCAN ME

Results

A

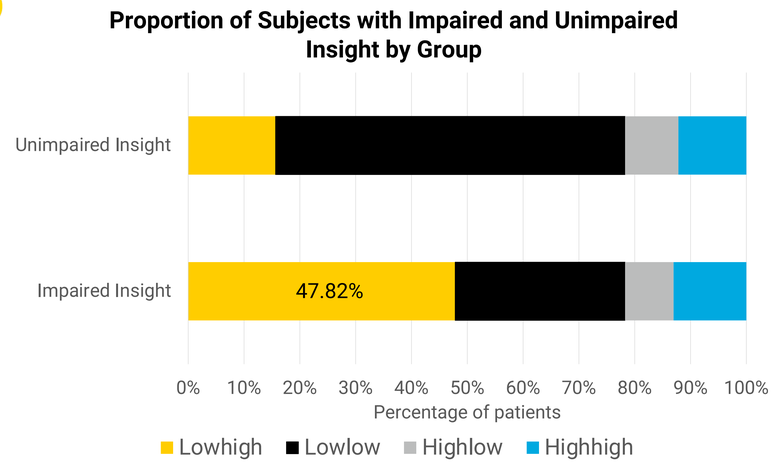

B

Chi-square analysis indicated that there was a significant relationship between insight and agreement of the BDI and ISPC, $\chi 2(3, N=138)=13$, $p=0.005$

- Post-hoc analysis (Bonferroni correction)

Lowhigh group has greater proportion of subjects with impaired insight ($p=0.004$)

Lowlow group has greater proportion of subjects with unimpaired insight ($p=0.035$)

Figure 1: Proportion of subjects with impaired and unimpaired insight by group

C

Multivariate lesion symptom mapping was used to investigate the neuroanatomical correlates of impaired insight in this Lowhigh group.

Patients in this group did not have brain damage that was significantly associated with their level of insight ($r = 0.19$, $p = 0.32$).

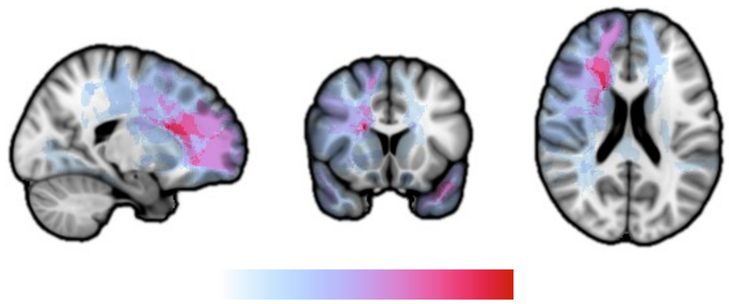

Figure 2: Lesion overlap map of patients in the Lowhigh group

Discussion

- In total, 30.43% of patients had discrepant self-report and collateral reports of depression (Lowhigh, Highlow), while 69.56% of patients had congruent BDI and ISPC depression now scores (Lowlow, Highhigh).
- Level of insight was significantly related to patients with brain lesions rating themselves low in depression while their collaterals rate them as highly depressed. Specifically, this group had a significantly higher proportion of patients with impaired insight compared to the other groups
- Reliance on self-reports of depression in patients with impaired insight might undermine their severity of depression. In this context, the ISPC insight subscale can be used as an indicator of impaired insight, and thus give the clinician an idea of the reliability of patient-reported depression scales.

Limitations

•Time between lesion onset and date of ISPC rating (interval) may influence how collaterals report personality disturbances in patients.

ANOVA analysis showed that in our sample, there is no significant difference of interval in the 4 groups [$F(3, 133) = 1.21$, $p=0.31$].

•Sample size for Lesion Symptom Mapping was small (N=29).

Acknowledgments

I would like to thank Amber Thomas, Dr. Boes, Dr. Tranel, and the Tranel Lab for their guidance on this project. I would also like to thank the Belin-Blank Center for providing me with this opportunity.

References

1. Chopra, M. P., Sullivan, J. R., Feldman, Z., Landes, R. D, & Beck, c. (2008). ;Self-, collateral-, and clinician assessment of depression in persons with cognitive impairment. *Aging & Mental Health*, 12(6), 675-683. https://doi.org/10.1080/13608608019724l2
2. Ott, B. R., & Fogel, B. S. (1992). Measurement of depression in dementia: Self vs clinician rating. *International Journal of Geriatric Psychiatry*, 7(12), 899-904. https://doi.org/10.1002/gps.930071209
3. Burke, W. J., Roccaforte, W. H., Wengel, S. P., McArthur-Miller, D., Folks, D. G., & Potter, J. F. (1998). Disagreement in the reporting of depressive symptoms between patients with dementia of the Alzheimer type and their collateral sources. *The American Journal of Geriatric Psychiatry: Official Journal of the American Association for Geriatric Psychiatry*, 6(4), 308–319. https://pubmed.ncbi.nlm.nih.gov/9793579/

Effects of Bone Density on Implant Stability in Total Ankle Replacement

Ruby Kolesar[1], Gabriel Clarke[2], Donald Anderson PhD[2]

[1]Fiorello H. LaGuardia HS, New York City, NY, [2]University of Iowa Department of Orthopedics and Rehabilitation, Iowa City, IA

Introduction

- Osteoarthritis is marked by the degeneration of an articular joint, which leads to disabling pain and loss of function.
- Total Ankle Replacement (TAR) is a surgical treatment for patients with end-stage osteoarthritis.
- TAR involves removing the damaged ends of the bones and cartilage from the ankle joint and replacing them with an implant.
- Success of contemporary TAR hinges on achieving early stability.

Objective

This study is based on the prediction that bone density around the implantation site influences tibial component stability. The goal is to use computed tomography (CT) scans to find bone density and simulate virtual implantation to determine how density affects the implant's behavior and stability.

Structure

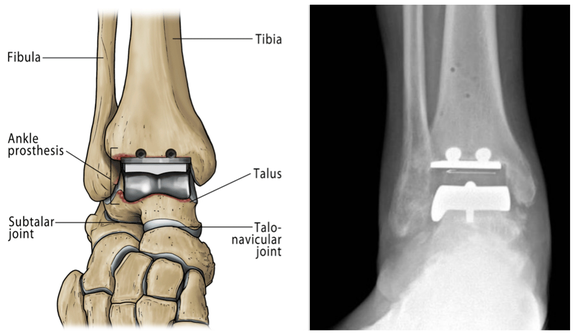

Figure 1: *(left) Graphical illustration of a total ankle replacement and (right) an x-ray of the ankle following implantation.[3]*

- Tibial component of TAR is implanted in the distal tibia (Figure 1)
- These prostheses are typically implanted with press-fit, relying upon elastic recoil of the bone to hold the implants more strongly and prevent early micromotion.
- Ability of bone to sustain press-fit is related to its density, which varies across individuals and can be compromised.
- Measuring bone density near where the tibial component is implanted provides a basis for evaluating how stable the implant will be following surgery.

Process

- CT scans provide a map of the radiodensity of tissues within a field of view, expressed in Hounsfield unit (HU) values.
- In prior research, mathematical equations have been derived that relate HU values to bone density (Figure 2).[5]
- These equations are a basis for computing the mechanical response of bone models to applied loads (flowchart below).

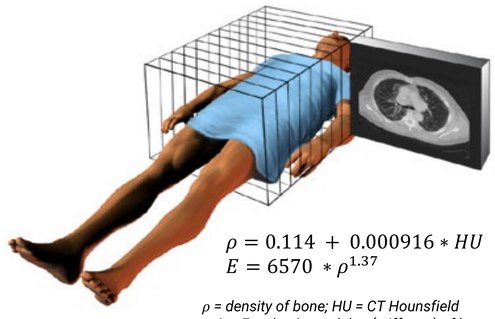

$$\rho = 0.114 + 0.000916 * HU$$
$$E = 6570 * \rho^{1.37}$$

ρ = density of bone; HU = CT Hounsfield units; E = elastic modulus (stiffness) of bone

Figure 2: *During a CT scan, an x-ray beam scans thin slices of the body, creating a 3D image of the internal structure through volumetric reconstruction.[1]*

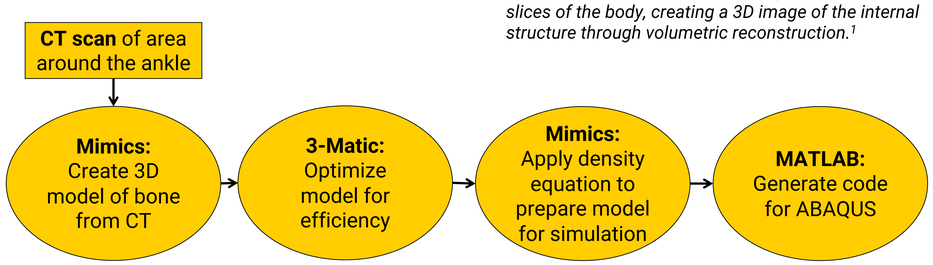

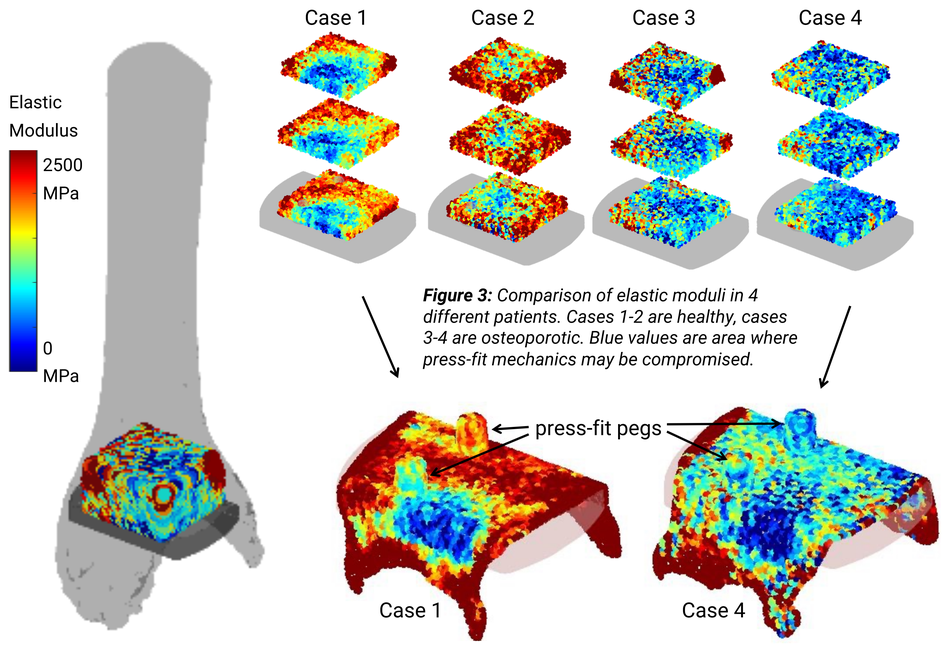

Figure 3: *Comparison of elastic moduli in 4 different patients. Cases 1-2 are healthy, cases 3-4 are osteoporotic. Blue values are area where press-fit mechanics may be compromised.*

Figure 4: *Elastic modulus values plotted in region of interest above tibial component of TAR.*

Figure 5*: Elastic moduli of implant contact surface in healthy and osteoporotic patients.*

Application

- Once the model has assigned properties, it can be put into ABAQUS, finite element analysis software.
- ABAQUS computes the mechanical response of a virtual implant in bone subjected to externally applied loads. Bones with varying density yield different results in implant-bone micromotion.
- Micromotion is an indicator of failure risk; when micromotions exceed 150 µm, fibrous ingrowth can occur instead of bony ingrowth, making it harder for the implant to succeed.

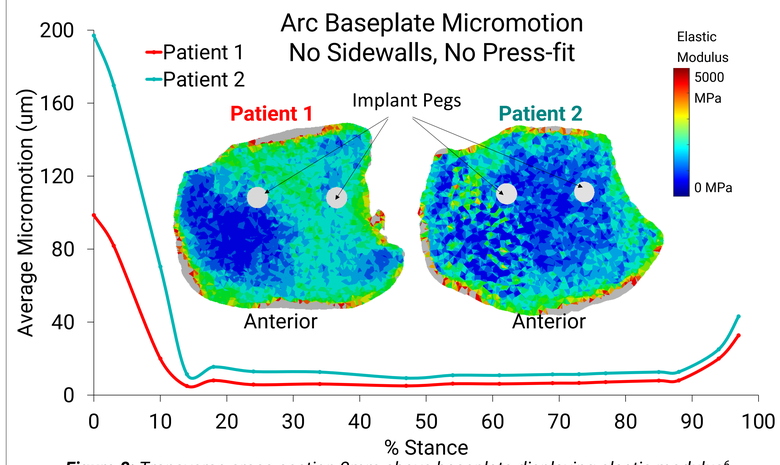

Figure 8: *Transverse cross-section 2mm above baseplate displaying elastic modulus[6] shows how lower bone density leads to higher micromotion*

Conclusions

- Through testing the virtual implants and analyzing differences in micromotion, bone density was shown to influence implant stability.
- Bones with a larger elastic modulus are more stiff, which helps keep the implant in place and reduce movement. This means that having higher bone density is correlated with greater stability.

Acknowledgments

I would like to thank Gabriel Clarke for his guidance, Dr. Don Anderson for the opportunity to work in his lab, and the University of Iowa for the access provided by the SSTP program.

References

1. Mayo Clinic. (2022, Jan 6). *CT Scan,* Mayo Clinic.
2. Florida Orthopedic. (n.d.). *Ankle Replacement Rapidly on the Rise.*
3. *My Ankle. (n.d.). Ankle Replacement.*
4. DenOtter, T.M, et al. (2023, March 6). *Hounsfield Unit.* StatPearls.
5. Rho, J. Y., et al. (1995). *Med Eng Phys*, *17*(5), 347–355.
6. Clarke, Gabriel. (n.d) *ASB Abstract ID 146189 [Abstract].* University of Iowa.

Platelet Function in Ehlers-Danlos Syndrome

Michelle Lee[1], Mariia Kumskova[2], Gagan D. Flora[2], Anil Chauhan[2]

[1]Henry M. Gunn High School, Palo Alto, CA; [2]Department of Internal Medicine, University of Iowa, Iowa City, IA

University of Iowa Carver College of Medicine
University of Iowa Health Care

Introduction

- Ehlers-Danlos Syndrome (EDS) is a heritable connective tissue disorder that often involves defects in collagen.
- There are 13 subtypes of EDS; most common types are hypermobile (hEDS) and classical (cEDS).
- Common symptoms: joint hypermobility, skin hyperelasticity, skin fragility, chronic pain.
- Easy bruising is a major criterion in four EDS types (classical-like, cardiac-valvular, dermatosparaxis, and musculocontractura) and a minor criterion in five EDS types (classical, vascular, arthrochalasia, kyphoscoliotic, and periodontal).

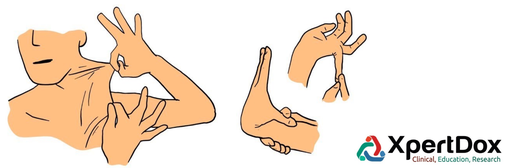

Hypothesis

The bleeding diathesis in EDS patients is due to dysfunction of platelet collagen receptors GPVI and integrin α2β1.

Methods

ISTH-BAT

- Screening tool used to assess 14 different bleeding symptoms on a scale of 0-4.
- Used to characterize bleeding symptoms in the human study population.

Light Transmission Platelet Aggregation

- Checks how well platelets clump together to form blood clots.
- Platelet-rich plasma sample with 2 x 108 platelets/mL.

Flow Cytometry

- Used to analyze the activation and function of the integrin αIIbβ3.
- Platelet-rich plasma sample with 2 x 108 platelets/mL.

Western Blotting

- Used to determine the level of protein phosphorylation in EDS subjects compared to healthy subjects.
- Washed platelets samples with 4 x 108 platelets/mL.

Human samples were excluded if subjects took medication with antiplatelet, anticoagulant, or prothrombotic effects within 7-10 days prior to the blood draw.

Results

Fig. 1 | ISTH-BAT of healthy and EDS subjects

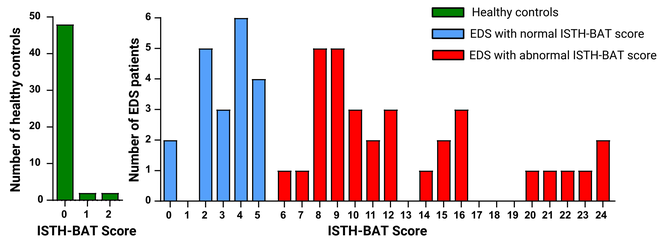

Fig. 2 | Bleeding symptoms

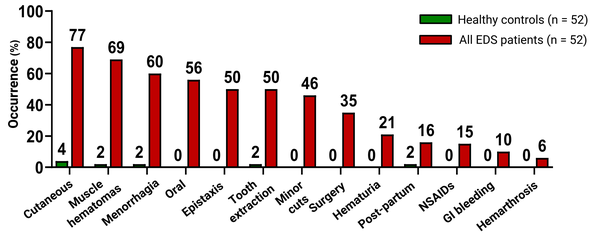

Fig. 3 | Platelet aggregation and αIIbβ3 activation in EDS patients

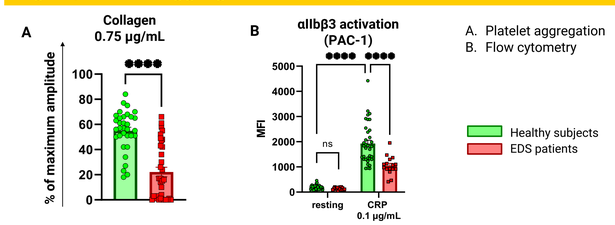

Fig. 4 | Platelet aggregation and αIIbβ3 activation in COL5a1-deficient mice

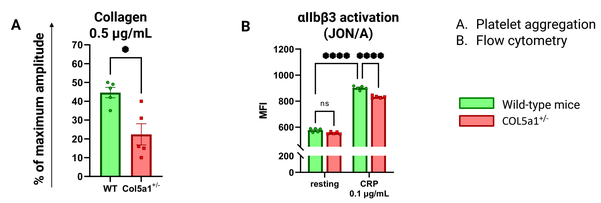

Fig. 5 | Collagen-induced platelet signaling in EDS patients

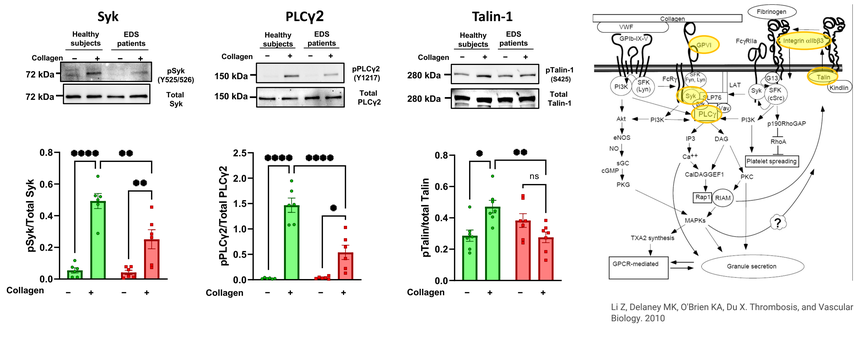

Li Z, Delaney MK, O'Brien KA, Du X. Thrombosis, and Vascular Biology. 2010

Study Population

Human cohort

	Healthy subjects, *n* = 52	EDS patients, *n* = 52
Demographics		
Age (median, range)	36 (16 - 61)	33 (16 - 69)
Gender		
Female (n, %)	50 (96%)	50 (96%)
Male (n, %)	2 (4%)	2 (4%)
Types of EDS		
hypermobile (n, %)	—	25 (48%)
classical (n, %)	—	14 (27%)
classical-like (n, %)	—	11 (21%)
vascular (n, %)	—	2 (4%)

Table 1 | Characterization of the human study population

EDS mouse model

COL5a1$^{+/+}$

Wild type (WT) littermate control

COL5a1$^{+/-}$

EDS classical type

- No known mutation of hEDS

Discussion & Conclusion

- EDS as a congenital connective tissue disorder that carries a high risk of hemorrhagic complications.
- Overall, 62% of patients with EDS demonstrated an abnormal bleeding score.
- The most frequent bleeding symptoms included bruising, muscle hematomas, menorrhagia, epistaxis, bleeding from the oral cavity, and bleeding after tooth extraction.
- Collagen-induced inside-out signaling and integrin αIIbβ3 activation are impaired in EDS patients.
- Platelet function impairment in COL5a1+/− mice mimics that in EDS patients.

Acknowledgements

I would like to thank Dr. Chauhan and the members of the Chauhan Lab for allowing me to have this opportunity, as well as Dr. Kumskova and Dr. Ghatge for their invaluable guidance.

References

1. Artoni A, Bassotti A, Abbattista M, Marinelli B, Lecchi A, Gianniello F, Clerici M, Bucciarelli P, La Marca S, Peyvandi F. Hemostatic abnormalities in patients with Ehlers–Danlos syndrome. Journal of Thrombosis and Haemostasis. 2018; 16: 2425-31.
2. Jesudas R, Chaudhury A, Laukaitis CM. An update on the new classification of Ehlers-Danlos syndrome and review of the causes of bleeding in this population. Haemophilia. 2019; 25: 558-66.
3. Kumskova M, Flora GD, Staber J, Lentz SR, Chauhan AK. Characterization of bleeding symptoms in Ehlers–Danlos syndrome. Journal of Thrombosis and Haemostasis. 2023; 21: 1824-30.
4. Malfait F, Francomano C, Byers P, Belmont J, Berglund B, Black J, Bloom L, Bowen JM, Brady AF, Burrows NP. The 2017 international classification of the Ehlers–Danlos syndromes. American Journal of Medical Genetics Part C: Seminars in Medical Genetics: Wiley Online Library, 2017, 8-26.
5. Rodeghiero F, Tosetto A, Abshire T, Arnold D, Coller B, James P, Neunert C, Lillicrap D, VWF ISj, Group PPHSW. ISTH/SSC bleeding assessment tool: a standardized questionnaire and a proposal for a new bleeding score for inherited bleeding disorders. J Thromb Haemost. 2010; 8:2063–5.

Parametrically Generating and Testing *n-sided* 3D-Printed Parabolic Solar Concentrators

Maxwell Leonard, Sebastian Hazelett, Dorothy Zheng, Reyna Alam, Daniel Keefe, Rezwan Sayeed, Fatima Toor

All code developed for this project is open-source and freely licensed

Introduction

3D-printed solar concentrators have the potential to make solar panels cheaper and easier to produce while potentially increasing the efficiency of solar panels by reducing recombination and surface reflection losses. Our research focused on expanding current work on 3D-printed parabolic solar concentrators, simulating and testing several hundred potential concentrator configurations to determine which were more efficient.

Process

We first characterized the reflectivity of several different metal-based paints in order to determine which paint would be used to coat the concentrators. Following the results shown in Figure 1, we chose a chromium-based paint and used its reflectivity to model a material in Radiance.

We then used OpenSCAD, a script-based CAD modeling application, to model 319 different solar concentrators, using the design and equations established in the Al-Shidhani et al proceeding.

```
g_concentration_ratio = 4;
g_num_sides = 3;
g_bottom_aperture_radius = 10;
g_concentrator_shell_thickness = 3.2;
g_parabolic_resolution = 0.2;
```

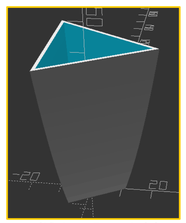

Concentrator modeling was primarily done by modifying 5 variables; the values shown to the left create the 4X triangular concentrator shown on the right.

We then simulated each concentrator using Radiance's photon mapping-based raytracing (depicted in Figure 2). A montage of the generated images can be seen in Figure 3.

After all images were rendered, we used MATLAB to determine the concentrating efficiency for each model.

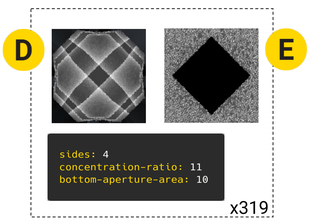

Fig 4. This image depicts all of the information used to determine the concentrating efficiency of a given parabolic concentrator. D is an illuminance image, and E is a luminance image used to determine the aperture location.

Using the results shown in Figure 5, we selected the 4 and 9X square, octagonal, and circular concentrators for further testing. These models were 3D printed, chemically smoothed, and coated, before being tested in a solar simulator, netting the results shown in figure 6.

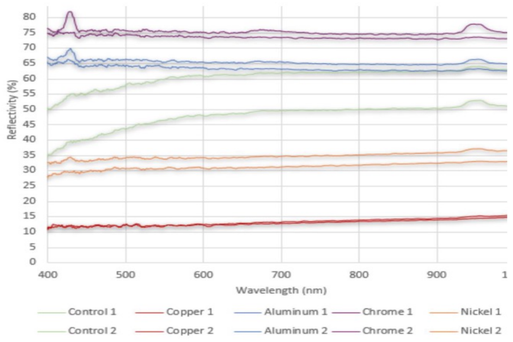

Fig 1. Several squares were printed, chemically smoothed, and coated, then tested in a spectrometer.

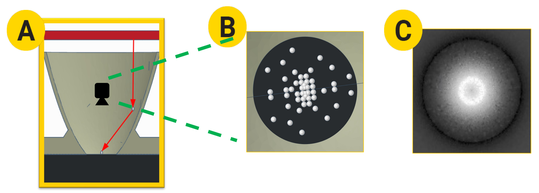

Fig 2. Depiction of photon mapping, the two-pass rendering algorithm used to simulate solar concentrators.
In the first pass, depicted in image A, photons are traced from a photon port until they are either absorbed or reflected from the scene. In the second pass, depicted in images B and C, photons are gathered from the photon map and used to render an image from a specific viewpoint.

Results

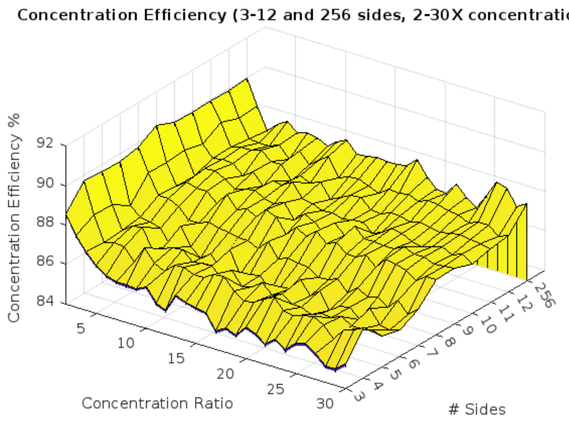

Fig 5. Relatively higher efficiencies were noticed at 4, 8, and 256 sides, and were used to select concentrators for further analysis.

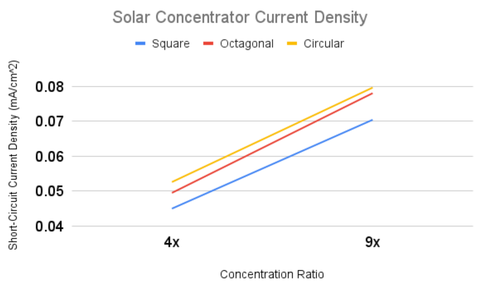

Fig 6. Concentrators were simulated by placing them directly below a solar concentrator, then focusing their output onto a solar cell and recording the short-circuit current.

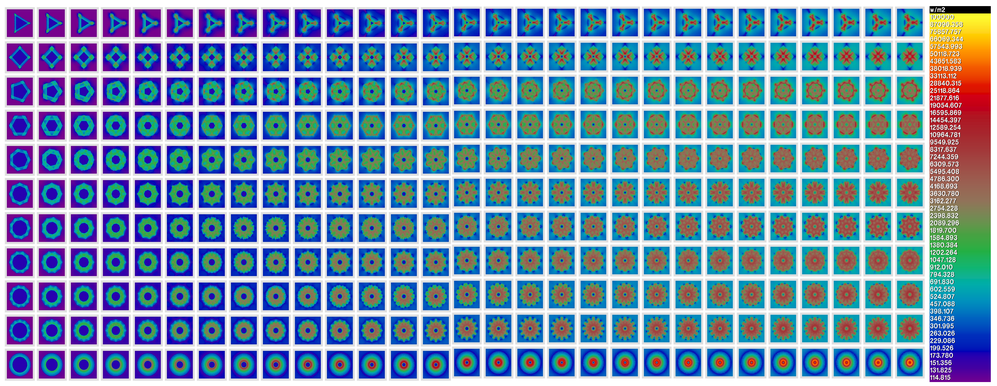

Fig 3. A montage of false-color illuminance images of our simulated concentrators. Concentration (2-30x) increases left to right, and number of sides (3-12, 256) top to bottom.

Analysis

- Circular concentrators appear to be the most efficient in real-world scenarios
- However, concentrators with lower numbers of sides more effectively disperse light rather than focusing it on the center
- Real-world testing was limited in scope, and further research is needed to better understand how concentration ratio and shape affect photovoltaic power output.

Impact

Over the course of the project, we traced over 500 million individual photons and used around 95 hours of whole-processor CPU time.
Given the power output of the processor at full load (80 watts) plus a rough estimate for cooling and other components, computing for this project likely emitted around

$$.11\,kW \times 95\,hours \times \frac{947^{[3]}\,lbs\,CO_2}{1\,MWh} \times \frac{1\,MWh}{1000\,kWh} = 9.90\,lbs\,CO_2$$

While this may be negligible, we hope to establish a precedent for future projects; photon mapping is notoriously computationally expensive,[2] and future projects may choose to take on a larger scope.

Acknowledgments

I'd like to thank my stellar research group for their work, Dan, Rezwan, Caleb, and Nick for their help and support in the lab, and, of course, Professor Fatima Toor.

References

1. Al-Shidhani, M., Al-Najideen, M., Rocha, V. G., & Min, G. (2018). Design and testing of 3D printed cross compound parabolic concentrators for LCPV system. *AIP Conference Proceedings*. https://doi.org/10.1063/1.5053489
2. Schregle, R. (2022). The RADIANCE Photon Map Extension User Manual. CC Envelopes and Solar Energy, 68–69. https://doi.org/10.13140/RG.2.1.4330.8405/1
3. U.S. Energy Information Administration. (2022, November 10). Iowa Electricity Profile 2021. https://www.eia.gov/electricity/state/iowa/

IOWA

How The American Civil War Impacted Migration Patterns

Kelvin Liu[1]; Maryam Torkashvand[2]; Caglar Koylu, PhD[2]

Choate Rosemary Hall, Wallingford CT[1]; Department of Geographical and Sustainability Sciences, University of Iowa[2]

Introduction

- Disruptive events substantially alter spatial and social interactions of humans.
- Although existing studies have thoroughly examined the volumetric, temporal, and spatial impact of disruptive events on human activities, the changes in structural patterns of human movement remain relatively unexplored.
- The American Civil War drastically changes the way people lived, worked, and interacted with one another, and had immediate and long-lasting impacts on the structure and functioning of social and spatial networks.
- Migration regions are groups of spatial units with a high degree of connection internally but low interaction with other subsystems.

Objective

- Investigate the American Civil War's impact on human migration.
- Understand how to utilize the Louvain method.

Methods

- Utilized Known Node-Correspondence (KNC) to examine the changes in community structures in pre- and post-war networks.
- Employed Louvain algorithm to identify migration network regions across the continental United States. Used these regions within the US to examine the structural changes in spatial migration networks between pre- and post-war periods.
- Used a series of quantitative comparisons to quantify the similarity of regions between partitions of pre- and post-periods of each network including Adjusted Rand Index, z-Rand coefficient, Rand coefficient, and Jaccard coefficient.

Results

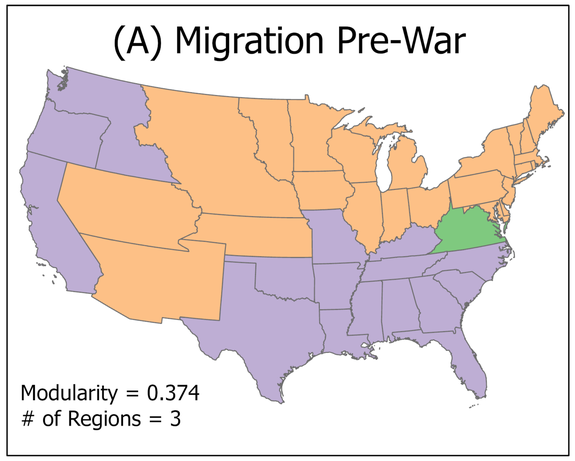

Figure 1 Migration Regions in (A) Pre- and (B) Post-War Periods

Network	Pre-Period	Post-Period	z-Rand	Rand	Adj. Rand	Jaccard
Family Tree	1840-1861	1865-1900	2.65	0.56	0.06	0.20

Table 1 Partition quantified data of pre- and post-war migration network

- Regions increased from 3 to 4 in the post-period, with significant changes. All 4 regions in the post-period were substantial in size. Notably, Region 2, which originally consisted of the Virginias, expanded northwards.
- Modularity shifted from 0.374 in pre-war to 0.349 in post-war period. While similar modularity values suggest similar connectedness in migration networks, the post-war modularity indicates that states in that period were less densely connected in terms of migration flows, possibly due to the Settlement of the West and longer-distance moves.
- The z-Rand score of 2.65 is significant when compared with the z-Rand scores of 18.11 (for 1850-60 and 1860-70) and 13.85 (1860-70 and 1870-80) found in Koylu et al. (In Review), indicating dissimilarity between the pre- and post-war regions.
- The Jaccard coefficient of 0.20 indicates a significant overlap between the two partitions.

Conclusion

- This study demonstrates that the American Civil War led to a notable reduction in migration connections within regions while increasing long-distance migration flows between regions in the post-war period. Regardless of these differences, regions derived from migration flows generated a significantly similar regional structure in the US.
- The data used in this study accurately represents the native-born white population, but not others such as Blacks, Native-Americans, or Mexicans.

References

Scan this QR Code to check out the full list of references!

Acknowledgments

I would like to thank Dr. Caglar Koylu and Maryam Torkashvand for their mentorship and guidance in my research in the Geo-Social Lab at the University of Iowa. I would also like to thank the Secondary Student Training Program and Belin-Blank for giving me this unforgettable opportunity.

Selected References

Koylu, C., Guo, D., Huang, Y., Kasakoff, A., & Grieve, J. (2020). Connecting family trees to construct a population-scale and longitudinal geo-social network for the U.S. *International Journal of Geographical Information Science*, *35*(12), 2380–2423. https://doi.org/10.1080/13658816.2020.1821885

Koylu, C., Torkashvand, M., Kwon, H., & Kasakoff, A. B. (2022). Mapping migration regions and their evolution from population-scale family trees. *Proceedings of the 6th ACM SIGSPATIAL International Workshop on Geospatial Humanities*. https://doi.org/10.1145/3557919.3565814

Evaluating the Radicals Involved in Organic Solid-State [2+2] Photocycloaddition Reactions

Katherine M. Lu, Samantha J. Kruse, Dr. Leonard R. MacGillivray
University of Iowa, Department of Chemistry, Iowa City, IA 52242

Background & Purpose

[2+2] photocycloaddition reactions are cycloaddition reactions where two molecules combine to form a cyclobutane-containing compound. Cyclobutanes are a versatile and essential building block, holding paramount importance across different scientific disciplines (i.e., pharmaceuticals, optoelectronics, and natural product synthesis).[1] Cyclobutanes are reported to be difficult to form synthetically using traditional methods, particularly in aqueous phases; however, solid-state [2+2] photocycloaddition reactions offer benefits such as they are environmentally friendly due to the lack of solvents used, thus significantly reducing the waste produced, and notably forms products in a quantitative yield (100% yield) (Scheme 1). This is an ideal outcome in chemical reactions, as it ensures the maximum utilization of reactants and minimizes waste, making the reaction extremely efficient, environmentally friendly, and economically favorable.

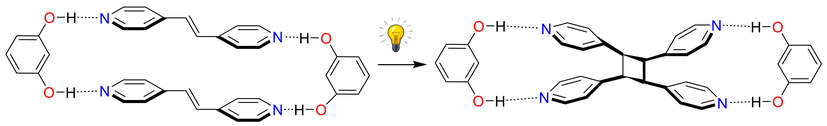

Scheme 1. Schematic of a solid-state organic [2+2] photocycloaddition using 1,3-dihydroxybenzene (**res**) and *trans*-1,2-bis(4-pyridyl)ethylene (**4,4'-bpe**).

Overall Project Goals

Although very useful, scientists are still studying the mechanism of how this reaction takes place in the solid state. While there are general assumptions, the exact specifics of how the reaction initiates and progresses are still unknown. Thus, the purpose of this study is to explore how a solid-state [2+2] photocycloaddition reaction occurs, specifically how they are initiated through radical production.

A variety of techniques were employed to evaluate the photoreactive cocrystal (**4,4'-bpe**)·(**res**)[2] that forms *rctt*-tetrakis(4-pyridyl)cyclobutane (**tpcb**), including nuclear magnetic resonance (^{1}H NMR) spectroscopy, electron paramagnetic resonance (EPR) spectroscopy, and powder X-ray diffraction (PXRD).

Experimental Methods

Synthesis

4,4'-bpe and **res** were weighed out in a 1:1 stoichiometric ratio, added to a 20 mL scintillation vial, and fully dissolved in ethanol. Vials were wrapped in foil and covered in parafilm, allowed to slowly evaporate overnight to form white plate-like crystals.

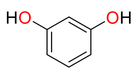

1,3-dihydroxybenzene (**res**)

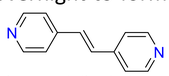

trans-1,2-bis(4-pyridyl)ethylene (**4,4'-bpe**)

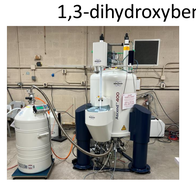

^{1}H NMR was collected to evaluate the progress of the photoreaction.

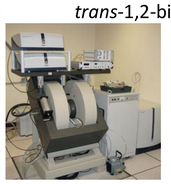

EPR was used to collect dose studies to evaluate radical formation.

PXRD was used to characterize materials before and after photoreaction.

Results: ^{1}H NMR Spectroscopy, Powder X-ray Diffraction, & EPR Spectroscopy

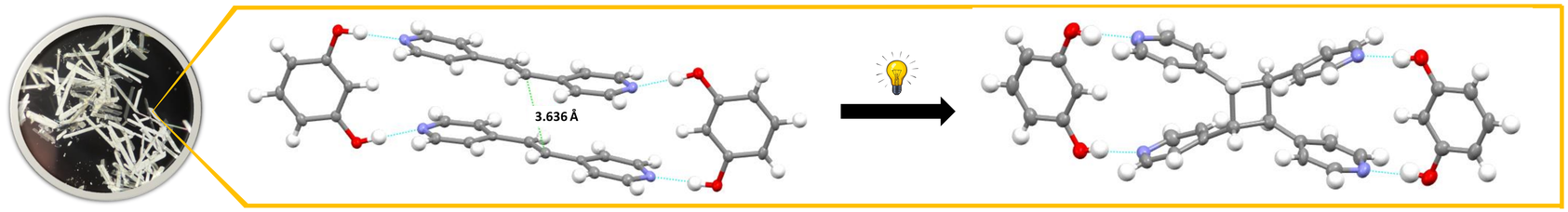

Figure 1. Left - Single crystals of (**4,4'-bpe**)·(**res**) at 10x objective under a microscope. Middle – 3-D model representation of (**4,4'-bpe**)·(**res**). Right – 3-D model representation of **tpcb**.

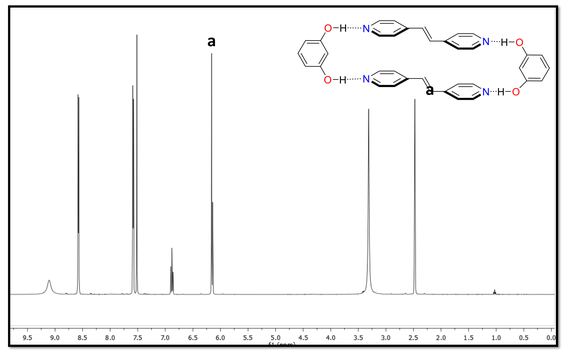

Figure 2. ^{1}H NMR spectrum of (**4,4'-bpe**)·(**res**).

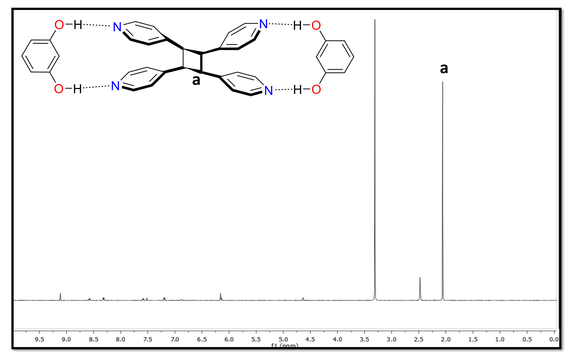

Figure 3. ^{1}H NMR spectrum of (**4,4'-bpe**)·(**res**) after photoreaction forming **tpcb.**

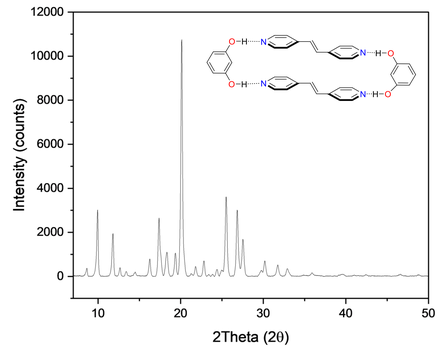

Figure 4. PXRD pattern of (**4,4'-bpe**)·(**res**).

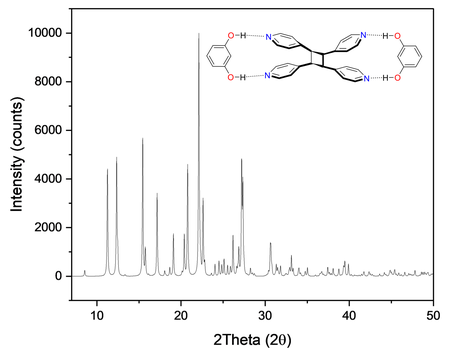

Figure 5. PXRD diffractogram of (**tpcb**)·(**res**)

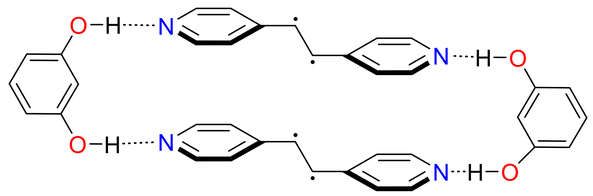

Scheme 2. Wire representation- of potential radicals formed in (**4,4'-bpe**)·(**res**) upon exposure to UV light.

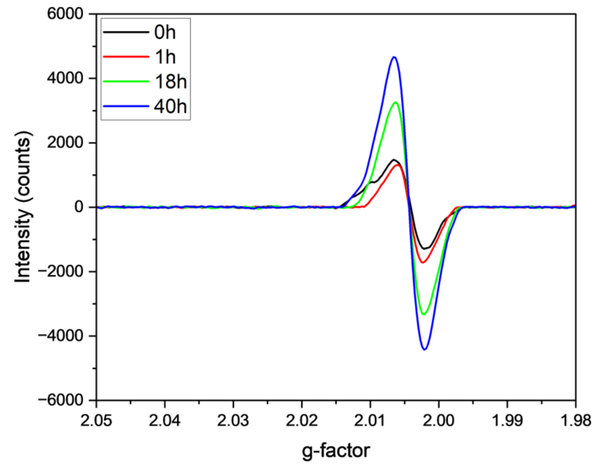

Figure 6. EPR Spectroscopy of the dose study for (**4,4'-bpe**)·(**res**). Carbon-centered radicals grow in as exposure to UV light increases.

Conclusion & Future Directions

Conclusion

- EPR shows the ingrowth of radical species in the solid-state [2+2] photoreaction.
- Only carbon-centered radicals are present in the photoreaction associated with the bridging double bond of the **4,4'-bpe**.
- A suite of characterization techniques paired with EPR allows us to monitor the exact points of this reaction and what/how many radicals are formed.

Future Directions

- EPR temperature studies – would evaluate which type of radical is present during the photoreaction (singlet diradical or triplet diradical). This will allow us to understand the first steps in a solid-state [2+2] photocycloaddition reaction.

Acknowledgements

Special thanks to:
The Belin Blank Center, the Secondary Student Training Program (SSTP), the Department of Chemistry, the MacGillivray research group, and the Forbes research group for their guidance and resources during this project.

References

[1] None Akhtaruzzaman, Khan, S., Dutta, B., Tamil Selvan Kannan, Goutam Kumar Kole, & Mohammad Hedayetullah Mir. (2023). Cocrystals for photochemical solid-state reactions: An account on crystal engineering perspective. 483, 215095–215095. https://doi.org/10.1016/j.ccr.2023.215095
[2] MacGillivray, L. R., Reid, J. L., & Ripmeester, J. A. (2000). Supramolecular Control of Reactivity in the Solid State Using Linear Molecular Templates. Journal of the American Chemical Society, 122(32), 7817–7818. https://doi.org/10.1021/ja001239i
[3] Rath, B. B., & Vittal, J. J. (2022). Photoreactive Crystals Exhibiting [2 + 2] Photocycloaddition Reaction and Dynamic Effects. Accounts of Chemical Research, 55(10), 1445–1455. https://doi.org/10.1021/acs.accounts.2c00107

Differences in Knee Joint Space Width Distribution Between Flexed vs. Extended Weight Bearing CT Scans

Connor Meng,[1] Tyce C. Marquez,[2] Donald D. Anderson[2]

[1]College of Education, [2]Departments of Orthopedics & Rehabilitation and Biomedical Engineering

Introduction

- Joint space width (JSW) is the bone-to-bone distance across an articular joint
- JSW narrowing is a defining feature of post-traumatic osteoarthritis (PTOA) [1]
- Around 50% of patients with ACL injury develop PTOA of their knee within 10-20 years post-injury [2]
- Weight bearing CT (WBCT) evaluates joints in functional loaded positions, offering greater sensitivity and accuracy than radiographs [3]
- We believe the screw-home mechanism (SHM) causes JSW distribution in the knee joint to be different in flexed vs. extended pose

Figure 1. Screw-home mechanism, by Kevin Tokoph, 2021. Retrieved from https://youtu.be/lyyv_4M2C3A.

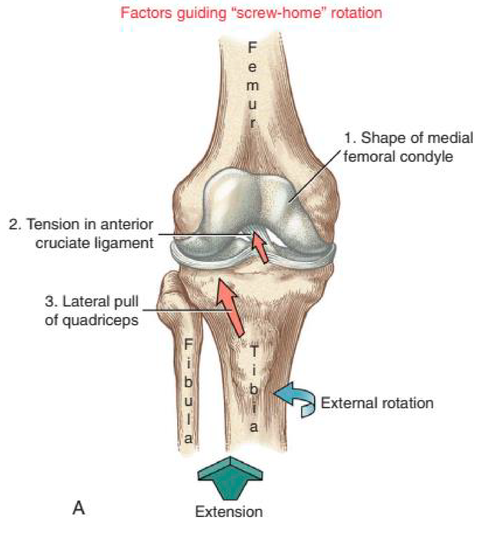

Purpose

Investigate differences in JSW distributions between flexed vs. extended in intact and ACL reconstruction (ACLR) WBCT scans of the knee.

Significance

- The knee is often evaluated in an extended pose
- Our research suggests the lowest JSW values are in different locations when knee is flexed due to SHM
- Analysis of JSW in a flexed and load-bearing pose may allow us to monitor the risk of PTOA more effectively in ACLR patients

Methods

- WBCT scans of the knee acquired for 43 patients ≥ 14-years old
  - 34 flexed scans and 19 extended scans obtained three months post ACLR
- 3D JSW maps and models of the articulating surfaces were generated using a fully-automated method (Figure 2) [1]
- Defined centroid of lowest 10% of JSW values as center of contact (COC)
- Measured the distance between COC in flexed vs. extended pose to assess the effect of SHM

Figure 2
Sample 3D JSW Maps

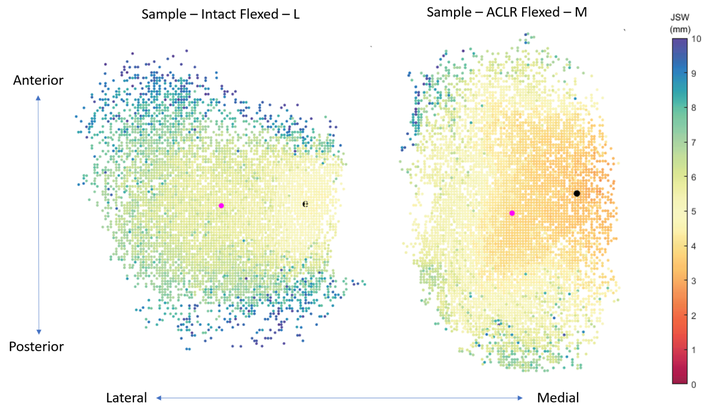

Note. Pink dot represents the overall centroid, black dot represents COC

Results

- In both compartments, COC is positioned more anteriorly in the extended than the flexed pose (Figures 3 and 4); it is placed more medially in the lateral compartment and vice versa
- In ACLR knees, the average distance between COC in flexed vs. extended pose is slightly larger than that of intact knees
- In ACLR knees, COC is in a slightly more anterior position than in intact knees (Figure 5)

Figure 3
Sample tibial articulating surface - lateral compartment

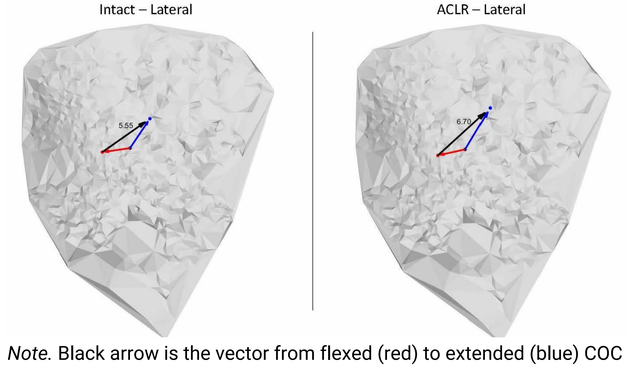

Note. Black arrow is the vector from flexed (red) to extended (blue) COC

Figure 4
Sample tibial articulating surface - medial compartment

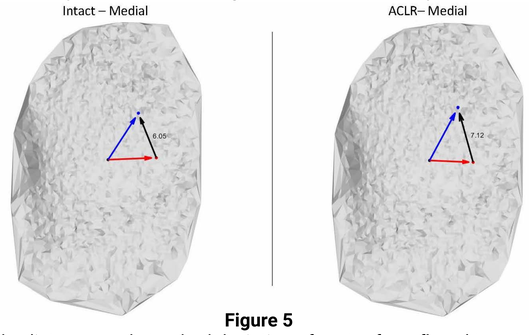

Figure 5
3D magnitude, distance, and standard deviation of vector from flexed to extended COC. Adapted from "Knee Joint Menisci Are Shock Absorbers: A Biomechanical In-Vitro Study on Porcine Stifle Joints" by A. Seitz et al., 2022. Retrieved from https://pubmed.ncbi.nlm.nih.gov/35372324/.

	3D Magnitude				
	x	y	z	Distance	SD
Intact - Lateral	4.48	-3.15	0.92	5.55	2.90
ACLR - Lateral	4.90	-4.47	0.95	6.70	2.89
Intact - Medial	-2.25	-5.59	0.52	6.05	2.27
ACLR - Medial	-1.90	-6.84	0.54	7.12	2.37

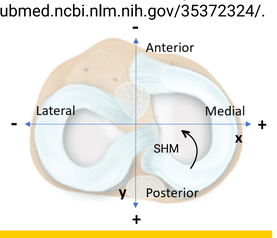

Conclusion

- The difference in the location of COC is consistent with the tibia's external rotation caused by SHM, meaning SHM likely changes where the narrowest JSW values occur in flexed vs. extended pose
- Observed difference between intact and ACLR knees is minimal and inconclusive, but this is at an early follow-up time point
- Follow-up is ongoing, and more WBCT scans will be obtained at one-year post-ACLR

Acknowledgements

This research was supported by a grant from the Arthritis Foundation (Award #851789).

References

[1] McFadden, E., Dibbern, K., Segal, N.a., Lynch, J.a., Felson, D.t., & Anderson, D. (2022). Fully automated 3D joint space width analysis of the tibiofemoral joint from weight bearing CT. Osteoarthritis and Cartilage, 30, S284-S285. https://doi.org/10.1016/j.joca.2022.02.382

[2] Lohmander, L. S., Englund, P. M., Dahl, L. L., & Roos, E. M. (2007). The long-term consequence of anterior cruciate ligament and meniscus injuries. The American Journal of Sports Medicine, 35(10), 1756-1769. https://doi.org/10.1177/0363546507307396

[3] Segal, N.a., Nevitt, M.c., Morales aquino, M., Mcfadden, E., Ho, M., Duryea, J., Tolstykh, I., Cheng, H., He, J., Lynch, J.a., Felson, D.t., & Anderson, D.d. (2023). Improved responsiveness to change in joint space width over 24-month follow-up: Comparison of 3D JSW on weight-bearing CT vs 2D JSW on radiographs in the MOST study. Osteoarthritis and Cartilage, 31(3), 406-413. https://doi.org/10.1016/j.joca.2022.12.002

Characterizing Mutations of the PKA Complex in Marbach-Schaaf Neurodevelopmental Syndrome

Aryan Pandey[1], Alexander Glebov-McCloud[2], Stefan Strack[2]
[1]Mount Juliet High School, Mount Juliet, TN
[2]Department of Neuroscience and Pharmacology, University of Iowa, Iowa City, IA

Introduction

Neurodevelopmental syndromes can range from manifesting through things like ADHD, ASD, global developmental delay, and motor skill deficits. Consequently, they often worsen the quality of life for afflicted patients along with their families putting socioeconomic strain on them.

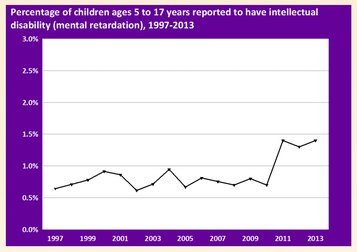

Figure 1. Data from the National Health Interview Survey showcasing the prevalence of children with intellectual disability rising from .9% in 1997-2012 to 1.3-1.4 in 2011-2013.

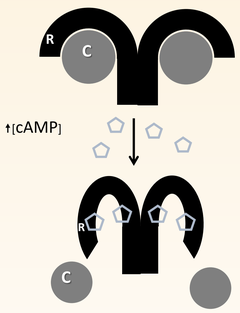

Figure 2. Protein Kinase A (PKA) is inactive in its tetramer form. 3'5'-cyclic adenosine monophosphate (cAMP) binds to the regulatory subunits in this form activating the catalytic subunits. This translates to the phosphorylation of downstream targets and gene transcription regulation.

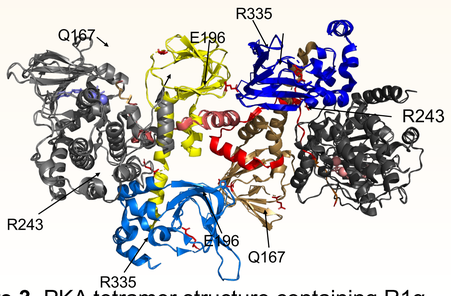

Figure 3. PKA tetramer structure containing R1α regulatory subunit and Cα catalytic subunit. R335 PKA R1β mutated residue is mapped to R1α subunits. The PKA R1α and R1β an 81% sequence identity with R335 being identical in both subunits. Cα = Gray, DD = Green, IS = Orange, CNA = Yellow, CNB = Blue.

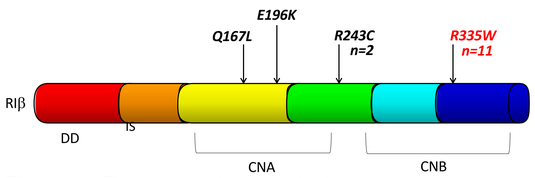

Figure 4. Representation illustrating all neurodevelopmental mutations respective to position on the PKA R1β subunit.

Methods and Results

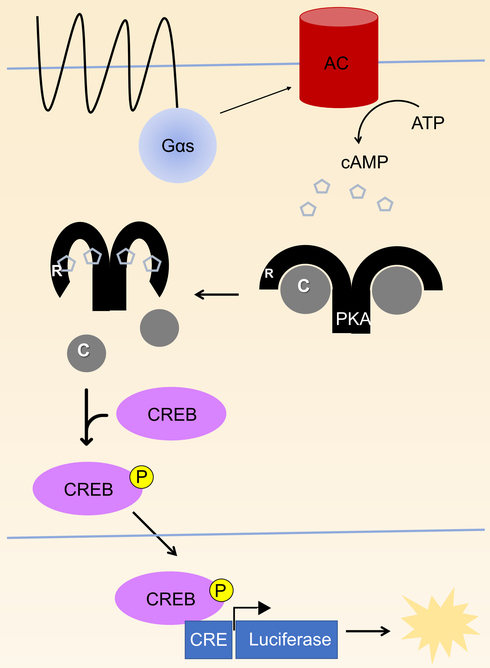

Figure 5. Diagram depicting molecular events upon stimulation of the PKA signaling pathway that contribute to bioluminescence. This can be used in a luciferase reporter assay to make determinations regarding transcriptional activity based on the expression of luciferase.

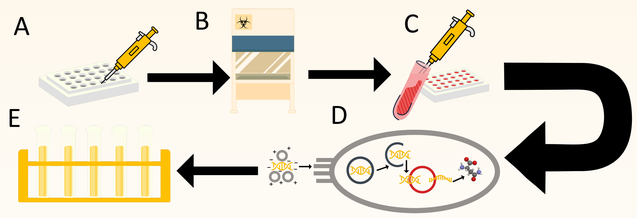

Figure 6. Diagram depicting procedures utilized when culturing neurons. **A,** Coat 24 well plates with polylysine. **B,** UV radiate plates to sterilize them. **C,** Insert neurons into plate wells. **D,** After waiting two days, use lipofectamine to transfect neurons. **E,** After waiting two more days, do luciferase reporter assays recording collected data.

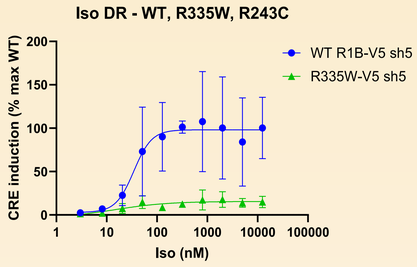

Figure 7. Luminescence generated by luciferase upon stimulation with isoproterenol in hippocampal and cortical cells. R335W-V5 sh5 displays a severe reduction in transcriptional activity as compared to WT R1B-V5 sh5. N=1

Condition	Emax ("Top", % max WT)		
	Experiment 1	Experiment 2	Experiment 3
WT R1B	100	100	100
L50R	78.25	75.7	83.75
R335W	6.667	4.062	8.269
R243C	13	11.71	16.09
Q167L	57.61	59.79	71.71
E196K	45.62	52.12	56.59
YC155	158.4	145.5	85.54

Figure 8. Table containing the proportions of maximum excitatory response with different conditions when compared to WT in percentage form. All conditions except YC155 consistently display reduced maximum response relative to WT.

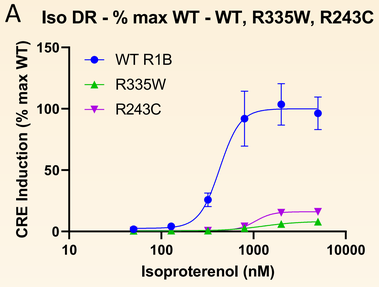

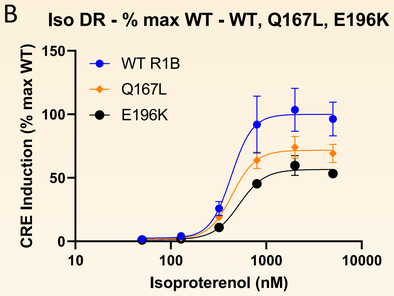

Figure 9. A, Luminescence generated by luciferase upon stimulation with isoproterenol in HEK394 R1A KO cells. R335W and R243C show a severe reduction in transcriptional activity relative to WT R1B. N=3. **B,** Luminescence generated by luciferase upon stimulation with isoproterenol in HEK394 R1A cells. Q167 and E196K show a moderate reduction in transcriptional activity relative to WT R1B. N=3.

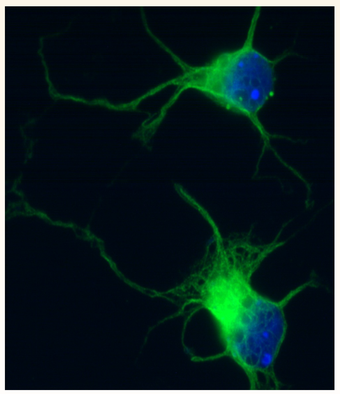

Figure 10. Image of the hippocampal and cortical neuronal cell culture. This is stained with beta III tubulin a neuronal marker confirming that they are definitely neurons. The image is representative of what was on the culture slide.

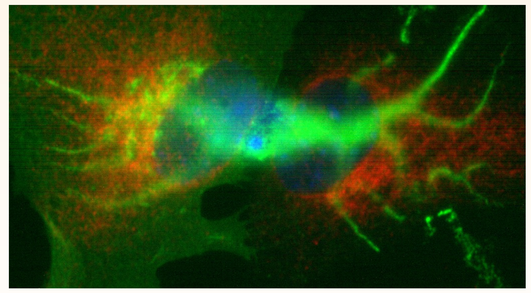

Figure 11. Image of hippocampal cortical neuronal cell culture. This was stained with Glial Fibrillary Acidic Protein (GFAP), a glial marker, along with beta III tubulin as a neuronal marker. These were the only glia we found indicating that there were very few glia in our culture.

Objective

The objective is to investigate how different variations the PKA tetramer compare in transcriptional activity in order to learn more about PKA's function and implications that changes to it can have. This information is to be expanded on a larger scale to better understand PKA's role in neurodevelopmental disorders as a whole along with their mechanisms.

Hypothesis

Given PKA's role in learning and memory along with the previously found presence of its variants in neurodevelopmental disorders, the hypothesis is that cells that are non-WT will display relatively reduced transcriptional activity in response to the isoproterenol.

Conclusions and Future Directions

Conclusions:

- The R1α KO cells and hippocampal neurons with the R335W have severely reduced transcriptional activity.
- The Q167L and E196K mutants display a moderate reduction for transcriptional activity in the R1α KO cells examined.

Future Directions:

- Assess if these results are reflective of smAKAP's ability to bind with R1β.
- Determine the underlying mechanism contributing to neurodevelopmental disorders in a mouse model of the conditions.

References

EPA. America's Children and the Environment, Third Edition. (2013).

Sandal, P., Jong, C. J., Merrill, R. A., Song, J., & Strack, S. (2021). Protein phosphatase 2A - structure, function and role in neurodevelopmental disorders. Journal of cell science, 134(13), jcs248187. https://doi.org/10.1242/jcs.248187

Acknowledgements

I would like to thank Dr. Strack, Mr. Glebov-McCloud, and everyone in the Strack lab for all of the mentorship, guidance, and support they graciously provided me throughout this project.

Envisioning the Coiled-Coil Domain on ANGPTL3

Sarah Park[1], Sydney Walker[2], Shwetha Shetty[2], Kelli Sylvers-Davie[2], Brandon S. Davies[2]

[1]Ames High School, IA; [2]Department of Biochemistry and Molecular Biology, University of Iowa

Introduction

Lipoproteins: responsible for transporting such lipids like triglyceride and cholesterol in bloodstream

- **HDL:** carries cholesterol
- **Chylomicrons/VLDL:** carries dietary TG

Lipases regulate lipoproteins through hydrolyzing free fatty acids into tissue

- **Endothelial Lipase (EL):** HDL
- **Lipoprotein Lipase (LPL):** triglycerides

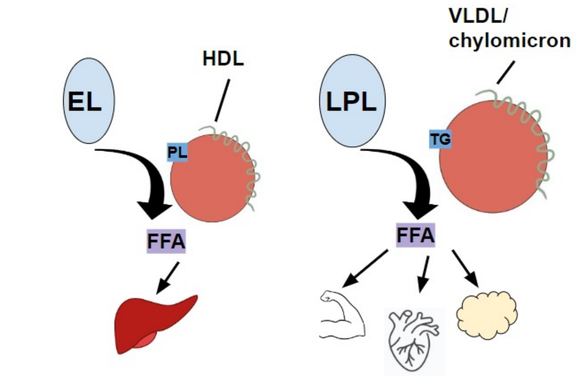

ANGPTL3: inhibits EL , LPL, increasing plasma TG levels

- Forms complex with ANGPTL8 to inhibit LPL (Chen et al, 2020).
- A3 expression decreases HDL and increases chylomicron, VLDL

Implications:

- High plasma TG levels and decreased HDL are risk factors in cardiovascular diseases.
- Low ANGPTL3 levels

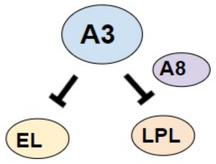

Objective

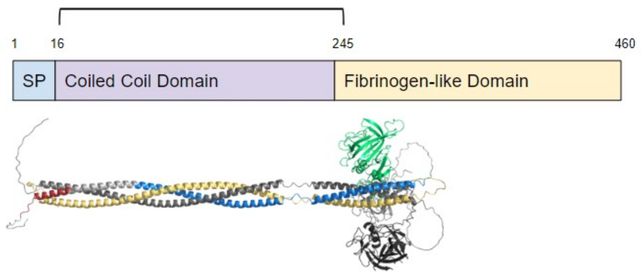

Identify the amino acid mutations on the coiled-coil domain of ANGPTL3 that are essential for EL and LPL binding and inhibition.

- Mutations L120A N121A (*pA42*), R139A L141A (*pA51*)
- Inward facing leucine

Methods

- **Mutant Protein Expression**
  - Site-Directed Mutagenesis of Plasmids
  - HEK293 Culturing, Transfections and Harvesting
  - SDS Page Gel Western Blots: quantify and visualize individual protein expression
- **EL Inhibition Assay**: serially diluted protein media, EL, and EL substrate added to fluorescence plate reader
- **NanoBiT Luciferase EL Binding Assay**: measure luminescence emitted from LgBiT tagged EL binding to SmBiT tagged proteins
- **Native Blue Gel Oligomerization Western Blot**

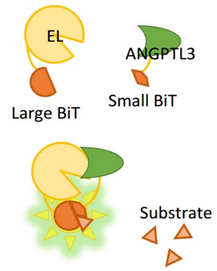

SDS Page Western Blot

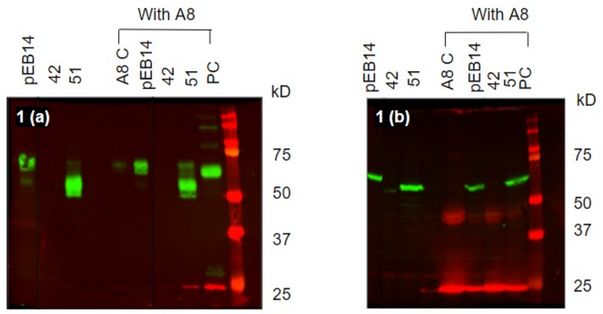

Figure 1 (a) and (b). Conditioned cell media (left) and cell lysate (right) western blot of ANGPTL3 expression in green and ANGPTL8 expression in red. From left to right: pEB14 WT, L120A N121A (pA42), R139A L141A (pA51), ANGPTL8 control, all with ANGPTL8 on the right, positive control, protein ladder. Lower bands implicate additional cleavages.

EL Inhibition Assay

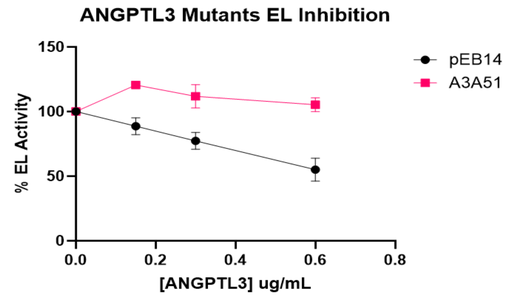

Figure 2. EL activity measured by fluorescence emitted through hydrolysis of phospholipids on substrate with increasing concentrations of pEB14 WT and R139A L141A at 37℃ for 30 minutes. Given values then divided by EL control and multiplied by 100 for the percentages. R139A L141A cannot inhibit EL.

EL Binding Assay

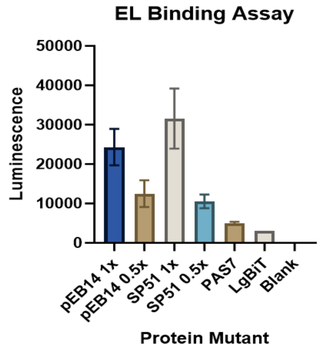

Figure 3. Emitted luminescence from doubled samples of pEB14 WT and R139A L141A and 50% dilutions of both measured with plate reader under 37℃ for 30 minutes. Given similar values of R139A L141A (A3A51) compared to WT, it does seem to bind to EL.

Native Blue Gel Oligomerization Western Blot

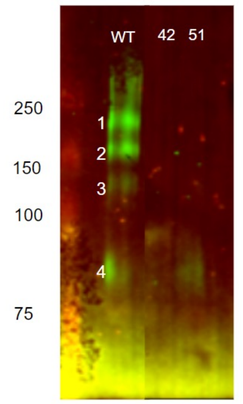

Figure 4. Conditioned cell media Native Blue Gel western blot of Poly A3 tagged ANGPTL3 mutant expression. From left to right: protein ladder, pEB14 WT, L120A N121A, R139A L141A. Top band represents trimers of full length, bands 2 and 3 represent trimers with 1 or 2 cleaved proteins respectively, bottom band represents monomers.

Conclusion

- ANGPTL3 mutant L120A N121A cannot express protein and thus cannot be assessed for EL and LPL binding and inhibition. However, mutant R139A L141A can bind to EL, though not inhibit.
- ANGPTL3 mutant R139A L141A cannot oligomerize.

Future Directions

- Perform RNA isolation and qPCR on L120A N121A and LPL Binding/Inhibition Assays on both mutants.
- Finish performing assays on the rest of the mutants on the alanine scan table.
- Generate a mutant mouse model to separating EL and LPL functions in a physiological context.

Acknowledgements

I would like to thank Dr. Davies and his lab for their mentorship and guidance. Special thanks to the Belin Blank Center and the University of Iowa Department of Biochemistry and Molecular Biology for this opportunity.

References

1. Chi, X., Britt, E. C., Shows, H. W., Hjelmaas, A. J., Shetty, S. K., Cushing, E. M., Li, W., Dou, A., Zhang, R., & Davies, B. S. J. (2017). ANGPTL8 promotes the ability of ANGPTL3 to bind and inhibit lipoprotein lipase. *Molecular Metabolism*, *6*(10), 1137–1149. https://doi.org/10.1016/j.molmet.2017.06.014
2. Chen, Y. Q., Pottanat, T. G., Siegel, R. W., Ehsani, M., Qian, Y.-W., Zhen, E. Y., Regmi, A., Roell, W. C., Guo, H., Luo, M. J., Gimeno, R. E., van't Hooft, F., & Konrad, R. J. (2020). Angiopoietin-like protein 8 differentially regulates ANGPTL3 and ANGPTL4 during postprandial partitioning of fatty acids. *Journal of Lipid Research*, *61*(8), 1203–1220. https://doi.org/10.1194/jlr.ra120000781
3. Sylvers-Davie, K. L., Segura-Roman, A., Salvi, A. M., Schache, K. J., & Davies, B. S. J. (2021). Angiopoietin-like 3 inhibition of endothelial lipase is not modulated by angiopoietin-like 8. *Journal of Lipid Research*, *62*, 100112. https://doi.org/10.1016/j.jlr.2021.100112
4. Shimizugawa, T., Ono, M., Shimamura, M., Yoshida, K., Ando, Y., Koishi, R., Ueda, K., Inaba, T., Minekura, H., Kohama, T., & Furukawa, H. (2002). ANGPTL3 decreases very low density lipoprotein triglyceride clearance by inhibition of lipoprotein lipase. *Journal of Biological Chemistry, 277*(37), 33742–33748. https://doi.org/10.1074/jbc.m203215200
5. Lee, E.-C., Desai, U., Gololobov, G., Hong, S., Feng, X., Yu, X.-C., Gay, J., Wilganowski, N., Gao, C., Du, L.-L., Chen, J., Hu, Y., Zhao, S., Kirkpatrick, L., Schneider, M., Zambrowicz, B. P., Landes, G., Powell, D. R., & Sonnenburg, W. K. (2009). Identification of a new functional domain in angiopoietin-like 3 (ANGPTL3) and angiopoietin-like 4 (ANGPTL4) involved in binding and inhibition of lipoprotein lipase (LPL). *Journal of Biological Chemistry, 284*(20), 13735–13745. https://doi.org/10.1074/jbc.m807899200

The Effects of a Common Plastic Additive on Mating Behavior

Nadia Patel[1], Yiyi Tu[2], Bryan Guevara[3], Maurine Neiman[3]
[1]Cedar Falls High School, [2]The Bishop School, [3]Department of Biology
University of Iowa, Iowa City, IA

How do plastic additives affect behavior?

- Our environment is filled with chemical additives that could plausibly influence health and behavior.
- New Zealand Mud Snail (*Potamopyrgus antipodarum*) are very sensitive to water environments and are thus a powerful aquatic ecotoxicology model system.
- Dimethyl Phthalate (DMP), a chemical reagent of phthalates, is common in variety of household items. It is also a known endocrine disruptor.

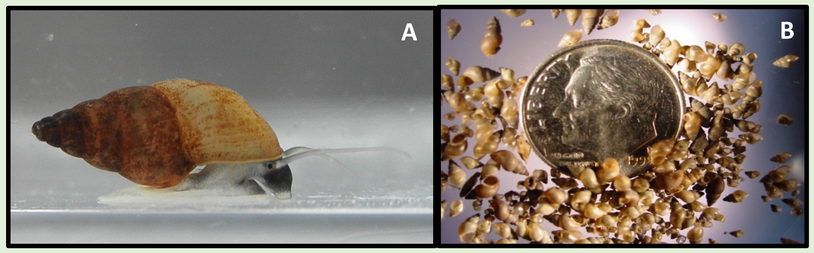

Fig 1. The New Zealand mud snail (*Potamopyrgus. antipodarum*) relative to a US dime. (A) Lateral view of mud snail. (B) Multiple mud snails surrounding a US dime.

New Zealand Mud Snails offer great models for studying ecotoxicology

Using a snail model to assess plastic toxicity

- How does DMP (Dimethyl Phthalate) affect the reproductive behavior of New Zealand Mud Snails?
- Relevant to human health concerns as well as ecosystem health.
- Use experimental approach to expose *P. antipodarum* to varying levels of DMP and assess reproductive behavior.

Hypothesis:

DMP negatively affects male reproduction because it represses androgen production, decreasing sexual behavior.

Prediction:

Frequency and duration of mating attempts by males will decrease with increased DMP concentration.

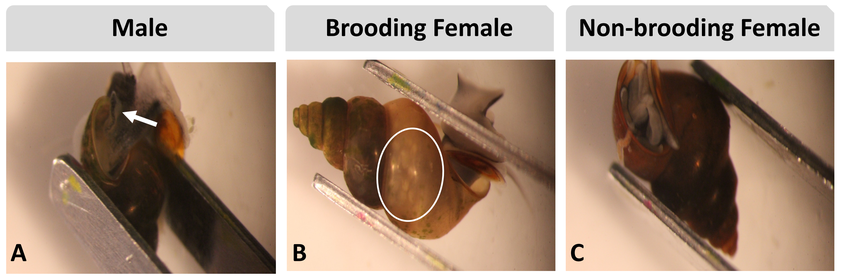

Fig 2. Snail Sexes and Embryo Brooding (A) Male mud snail rotating head left revealing penis—highlighted by the white arrow. (B) Brooding female snail with embryos visible from exterior of shell. Embryos are highlighted inside the white circle. (C) Non-brooding female with no embryos visible from exterior of shell.

Quantifying DMP effects on behavior

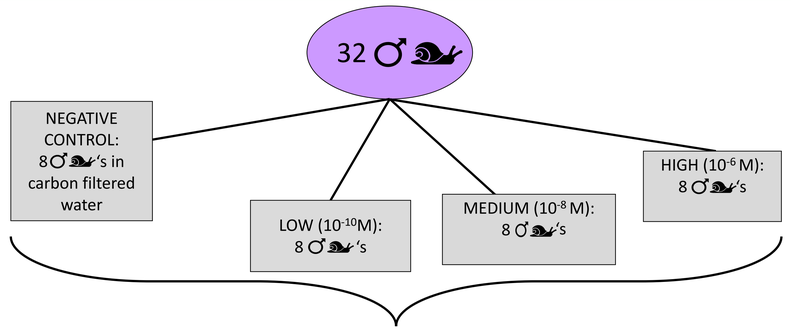

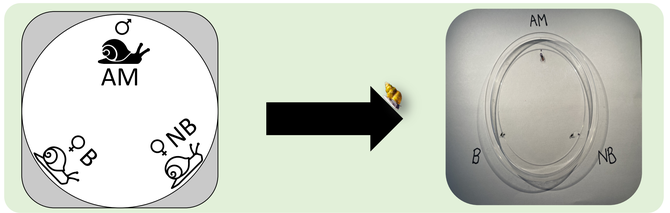

Fig 3. Model for Assessing Male Reproductive Behavior Post-DMP Exposure. Male (M) is placed equidistant from brooding (B) female and non-brooding (NB) female. The snails are given 2 hours to mate within the 4" diameter petri dish. The frequency of mating attempts and the mating duration are calculated per 2-hour interval.

Fig 4. Closer Look at the Mating of New Zealand Mud Snails. The male snail moves his aperture in alignment with the aperture of the female; mating takes place under the shell.

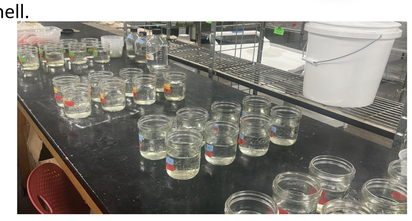

Fig 5. Photos of the 5-week exposure of DMP for New Zealand Mud Snail Males, with four treatment groups containing eight sexual male snails each.

DMP treatment affects mating behavior

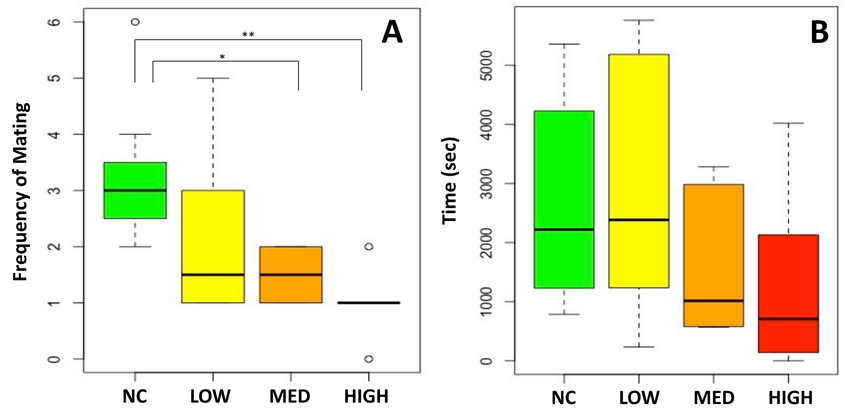

Fig 6. DMP Effects on Mating Behavior. (A) There was significantly more mating in the no-exposure (negative control) group relative to the medium and high groups. * = $p < 0.05$, ** = $p < 0.005$ (B) There was a trend towards decreased mating duration as DMP dose increased.

Males mated more with brooding females

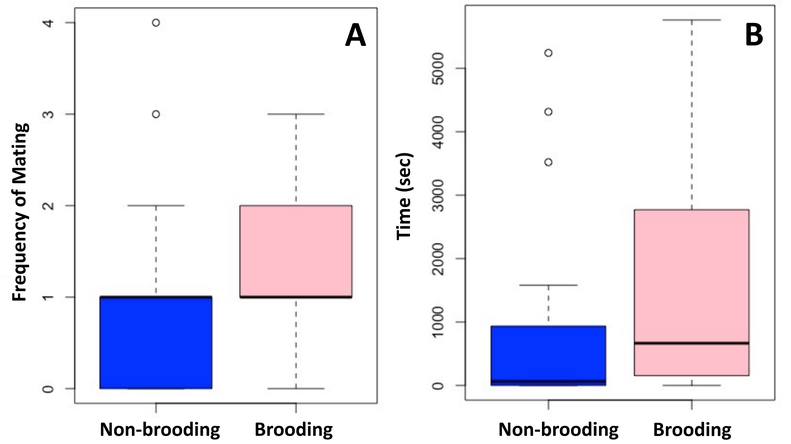

Fig 7. Male Preference During Mating Trials. (A) Males had the ability to choose between mating with a non-brooding or brooding female. Males preferred to mate with brooding vs. non-brooding females. (B) Males mated with brooding vs. non-brooding females for significantly longer durations.

Reproduction is influenced by a plastic behavior additive

- DMP negatively affects mating behavior in *P. antipodarum;* effects increase with dose.
- There could be consequence of DMP exposure for reproductive behavior in other organisms such as humans.

- Males preferred mating with brooding over non-brooding females, and they mated for longer durations with the former.
- Why is unclear but could be linked to higher fertility of brooding females and/or greater propensity of brooding females to mate.

Future Directions

- How would male snail reproductive behavior change at even higher concentrations of DMP?
- Will reproductive behavior in brooding vs. non brooding snails be differentially affected by DMP? What about embryos produced after DMP exposure?
- How do other reagents of phthalates affect reproductive behavior?
- Could DMP affect humans? How?

Acknowledgements

Special thanks to Bryan Guevara for actively mentoring and supporting me through this project, Maurine Neiman for guiding me through this research journey, and Yiyi Tu for her moral support. We also thank the Belin Blank Center for this incredible research opportunity and funding.

References

M;, S. S. J. (n.d.). *Evidence for stronger discrimination between conspecific and heterospecific mating partners in sexual vs. asexual female freshwater snails*. PeerJ. https://pubmed.ncbi.nlm.nih.gov/36447513/
The R project for statistical computing. R. (n.d.). https://www.r-project.org/
Time-lapse video recording software. VideoVelocity. (n.d.). http://www.candylabs.com/videovelocity

Top2A is a Novel Progesterone Receptor Repressor in Endometrial Cancer

University of Iowa Holden Comprehensive Cancer Center

Aarthi Raghavan[1]; Xiangbing Meng, PhD[2]; Shujie Yang, PhD[2]

[1]American High School, CA; [2]Department of Pathology, University of Iowa

Belin-Blank Center, College of Education, The University of Iowa

I. Background

Progesterone Receptor (PR) Expression

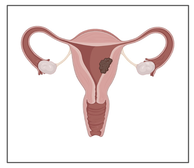

Figure 1: Diagram of uterus with endometrial cancer. The brown mass depicts the tumor.

- Endometrial cancer is located in the uterus (Figure 1)
- Estrogen promotes endometrial cancer cell proliferation
- Progesterone is another hormone
- Progesterone negatively regulates estrogen-driven tumor growth and is an ultimate tumor suppressor in endometrial cancer
- MYC is a proto-oncogene and reported as a PR downstream gene

★ PR expression is significantly downregulated in endometrial cancer patients

Top2A

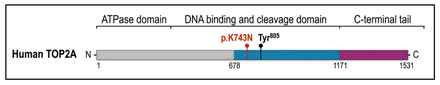

Figure 2: Diagram of the Top2A structure (each section is labeled above)

- Topoisomerase 2A (Top2A) is a human enzyme that controls and alters the topologic states of DNA during transcription (Figure 2, 3)
- In cancer cells, trapped TOP2 enzymes block the essential steps in DNA replication, overwhelming the DNA damage repair mechanisms

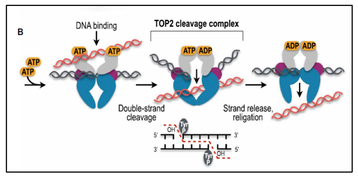

Figure 3: Diagram of TOP2A function. TOP2 binds helix-helix crossovers of DNA as a homodimer that cleaves both strands of duplex DNA and forms TOP2cc by covalently attaching tyrosine (Tyr) to the 5'-ends of the cleaved DNA. TOP2cc allows the passage of the uncleaved helix and the subsequent seamless religation of the DNA breaks. Overall, Top2A relieves DNA torsional stress during transcription.

- Top2A is more heavily expressed in primary tumors over the normal tissues

★ Top2A seems to have a reverse correlation with PR expression (Figure 4)

★ Increased expression of Top2A predicts unfavorable survival in endometrial cancer patients (Figure 5)

★ The tissue samples from 6 patients shown below confirm that Top2A and PR expression are negatively correlated (Figure 6)

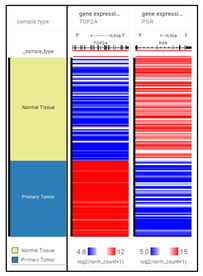

Figure 4: Patient data of Top2A levels and PR expression in normal and primary EC tissues. Adapted from Xena Browser.

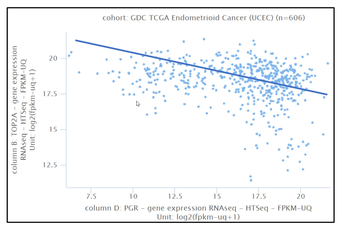

Figure 5: Xena Browser patient data showing correlation between Top2A levels and PR expression in endometrial cancer. Line of best fit is shown. r=-0.2668 and p=5.868e-11

Patient	#2173, Age 75	#2118, Age 70	#2339, Age 79	#1881, Age 86	#2113, Age 67	#1164, Age 66
	None	None	Moderate	Weak	None	Strong
PR	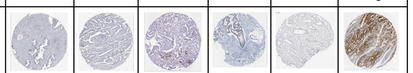					
	Strong	Strong	Strong	Medium	Medium	<25%
Top2A	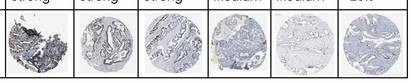					

Figure 6: Patient data showing the levels of PR and Top2A in tissue. The results show that as the PR expression becomes strong, Top2A expression becomes weaker. Adapted from Human Protein Atlas.

II. Objectives

#1 Analyze PR expression trend in Top2A knockdown (kd) cells

#2 Inhibit Top2A activity and then measure PR expression

#3 Measure the cell growth in the Top2A kd cells

III. Methods

1

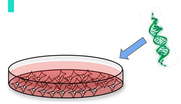

Knockdown Top2A using siRNA & shRNA

- siRNA: transfect cells twice
- shRNA: lentivirus transfection
- passage to TC100
- wait 48-72 hours

2

Use Top2A inhibitors on cells

- used Idarubicin and Mitoxantrone
- tested both MYC and PR expression

3

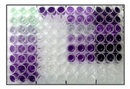

BCA assay to determine the loading volumes

- 25 ml total in each well
- standards (25 µL), water (22.5 µL), samples (2.5 µL)

4

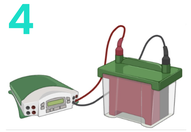

WB and capturing the final images

- used both 7.5% and 12% gel
- transfer ON
- use filter paper and the NC membranes

IV. Results

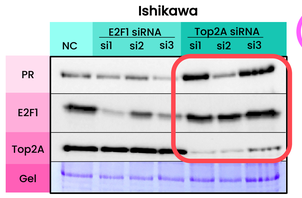

Figure 7: First experiment of siRNA-transfection with E2F1 and Top2A in Ishikawa. E2F1 did not impact PR expression and was thus excluded.

- The Top2A siRNA1 and siRNA3 knockdown Top2A well – it's barely visible (Figure 7)
- Clear increase in PR expression for Top2A siRNA1 and siRNA3 when compared to the negative control (Figure 7)

- Top2A siRNA1 and siRNA3 knockdown Top2A in Ishikawa (Figure 8)
- All Top2A siRNAs knock down Top2A in ECC1 (Figure 8)
- There is a clear increase in PR expression for the above samples

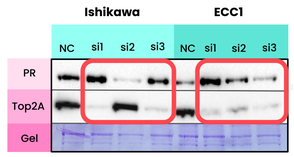

Figure 8: Second experiment of Top2A siRNA transfection in Ishikawa and ECC1. The gel loading is also shown for comparison to the expression levels.

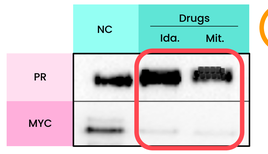

Figure 9: Drug testing with Idarubicin and Mitoxantrone to inhibit Top2A in Ishikawa and examine the effect on MYC and PR expression.

- Both Top2A inhibitors Idarubicin and Mitoxantrone increase PR expression
- At the same time, MYC expression clearly reduces (Figure 9)

Results (Continued)

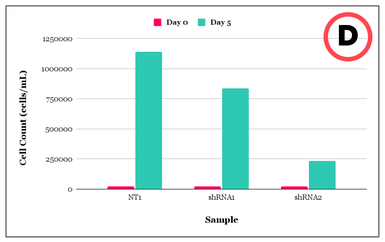

Figure 10: Measuring cell proliferation in Top2A knockdown cells with shRNAs 1 and 2 over five days. All samples started with 25000 cells per mL.

- The shRNA1 and shRNA2 samples have lower growth than the negative control (Figure 10)
- Doubling rates: 21.77 hrs (NT1), 23.69 hrs (shRNA1), and 37.23 hrs (shRNA2)

- shRNA1 and 2 knockdown Top2A and increase PR (Figure 11)
- shRNA 2 levels are more extreme

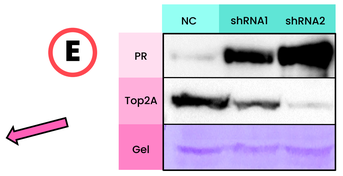

Figure 11: Confirming that shRNA1 and shRNA2 knockdown Top2A in Ishikawa

V. Conclusion/Future Directions

- Top2A knockdown increases PR expression in siRNA1 and siRNA3 in Ishikawa and all siRNA in ECC1
- Top2A inhibitors Idarubicin and Mitoxantrone increase in PR expression
- The knockdown of Top2A in Ishikawa reduces cell growth
- It is likely that Top2A is a bonafide PR repressor in endometrial cancer cells
- Future studies should determine the mechanism for Top2A repressing PR
- Future experiments could involve Top2A inhibition and knockdown in mice endometrial cancer tumor cells
- Our data overall suggests Idarubicin and Mitoxantrone can be potential treatments for endometrial cancer patients based on Top2A inhibition

VI. Acknowledgements

I would like to extend my gratitude to the Belin Blank Center for providing this incredible opportunity and to Dr. Meng and Dr. Yang for their valuable guidance and mentorship in these five weeks. This project was supported by NIH R37-CA238274 (SY) and the Department of Pathology Start-Up Fund (SY).

VII. References

[1] Kavlashvili, T., Jia, Y., Dai, D., Meng, X., Thiel, K. W., Leslie, K. K., & Yang, S. (2016). Inverse relationship between progesterone receptor and Myc in endometrial cancer. PLOS ONE, 11(2). https://doi.org/10.1371/journal.pone.0148912

[2] Kim, J. & Chapman-Davis, E. (2010). Role of progesterone in endometrial cancer. Seminars in Reproductive Medicine, 28(01), 081–090. https://doi.org/10.1055/s-0029-1242998

[3] Mayo Foundation for Medical Education and Research. (2021, May 20). Endometrial cancer. Mayo Clinic. https://www.mayoclinic.org/diseases-conditions/endometrial-cancer/symptoms-causes/syc-20352461

[4] Odiegwu C.N.C., Ukaejiofo E.O., Tothill I.E., Chianella I., & Okey-Onyesolu C.F. (2020). Purification and characterisation of lectin isolated from nigeria Achatina Achatina snail. GSC Advanced Research and Reviews, 5(3), 001–009. https://doi.org/10.30574/gscarr.2020.5.3.0095

[5] Ramamoorthy, M., Tadokoro, T., Rybanska, I., Ghosh, A. K., Wersto, R., May, A., Kulikowicz, T., Sykora, P., Croteau, D. L., & Bohr, V. A. (2011a). RECQL5 cooperates with topoisomerase II alpha in DNA decatenation and cell cycle progression. Nucleic Acids Research, 40(4), 1621–1635. https://doi.org/10.1093/nar/gkr844

[6] Uusküla-Reimand, L., & Wilson, M. D. (2022). Untangling the roles of top2a and top2b in transcription and cancer. Science Advances, 8(44). https://doi.org/10.1126/sciadv.add4920

[7] Yang, S., Thiel, K. W., & Leslie, K. K. (2011a). Progesterone: The ultimate endometrial tumor suppressor. Trends in Endocrinology & Metabolism, 22(4), 145–152. https://doi.org/10.1016/j.tem.2011.01.005

Endocannabinoid Receptor 1 in Sensory Neurons Affects Body Weight and May Contribute to Bariatric Surgery Outcome in Mice

Sana Rajesh [1], Yi Chu, PhD [2], Mohamad Mokadem, MD, PhD [2]

1. Gretchen Whitney High School, Cerritos, CA
2. Department of Internal Medicine, Division of Gastroenterology and Hepatology, University of Iowa, Iowa City

BACKGROUND

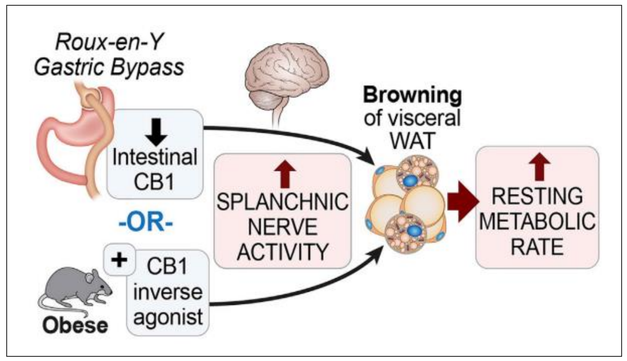

This study focuses on the endocannabinoid receptor 1 (CB1), a key regulator of energy signals along the gut-brain axis located in both the central nervous system (CNS) and peripheral nervous system (PNS), and its effects on metabolism. The goal is **to understand the effects of CB1 receptors in sensory neurons of mice fed with a high-fat diet (western diet) and how this receptor may determine the outcome of RYGB surgery.**

METHODS

We used Wildtype (WT) & Knockout (KO) mice to explore fluctuations in Body Weight (BW) and Food Intake (FI) after high-fat diet (HFD) feeding over a span of 20 days.

Breeding Schematic:

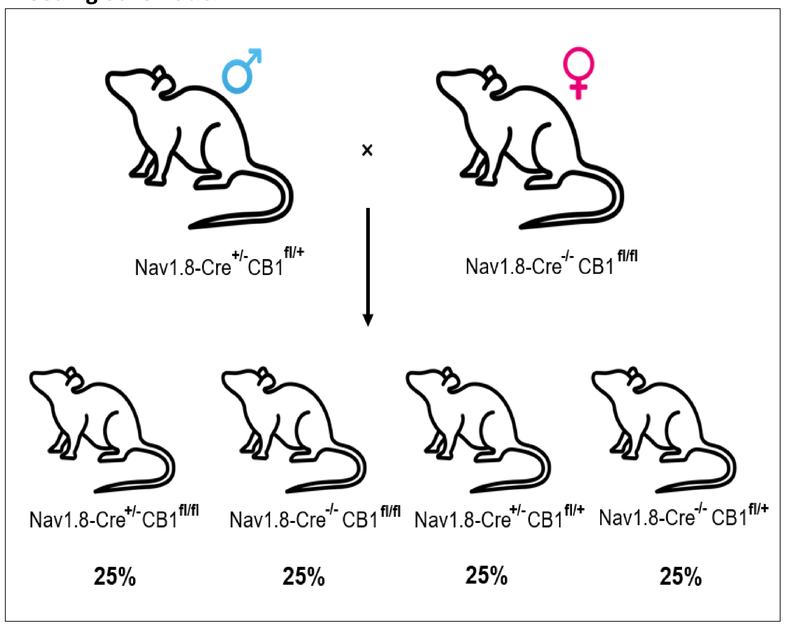

Figure 1. When breeding, looking for Nav1.8-Cre$^{+/-}$ CB1 $^{fl/fl}$ as "knock-out" for the CB1 gene while the rest are used as control during experimentation.

RESULTS

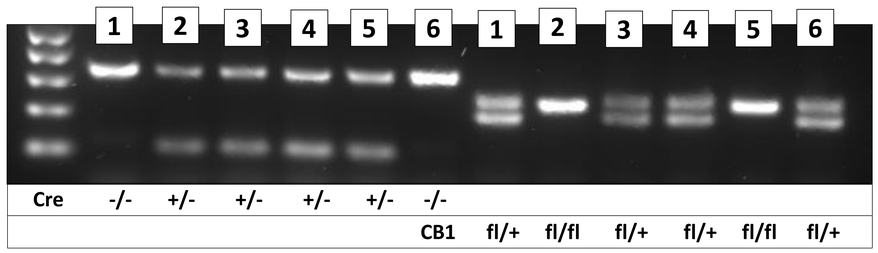

Figure 2. Cre control band weight (360 bp). Cre positive band weight (100 bp). CB1 Flox band weight (233 bp). CB1 Wild-type band weight (197 bp). In this litter, Mice #2 and #5 are KO, the others are Control. 2 out of 6 mice being KO is higher than expected.

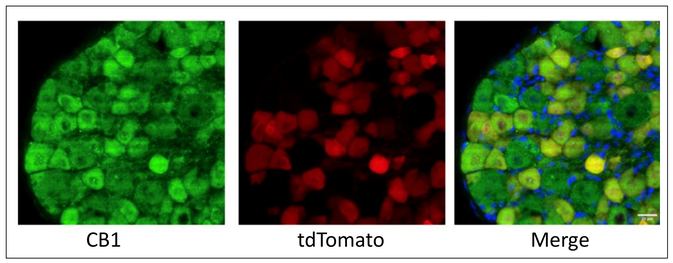

Figure 3. Stained CB1 using a tdTomato protein marker and analyzed through fluorescence microscopy. CB1 is expressed in all Nav1.8 $^{+}$ neurons in Dorsal Root Ganglion.

Figure 4. Whereas CB1 (red) is present in the DRG of the control mouse, it is not present in DRG of the KO (Nav1.8-Cre$^{+/-}$ CB1$^{fl/fl}$) mouse. This differentiation is what is utilized in the lab to determine the effects of CB1 on metabolism.

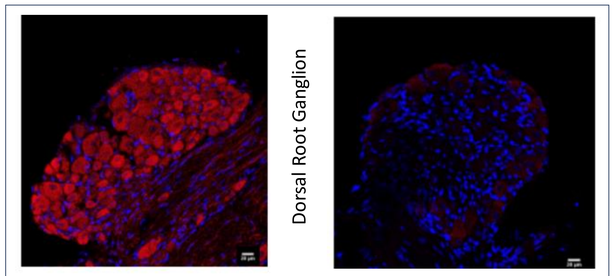

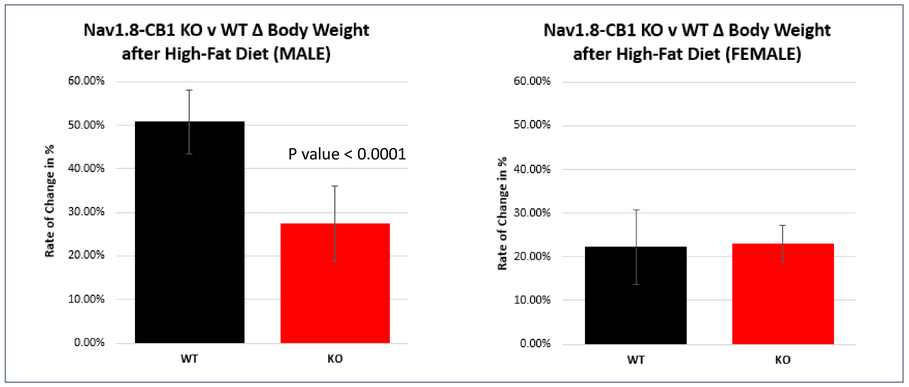

Figure 5. Male KO mice have a statistically significant lower ROC for body weight than control with the avg. for WT being 50% and the avg. for KO only being 28%

Figure 6. WT and KO female mice have around the same avg. ROC for body weight (22%). Female mice are more resistant to weight fluctuations.

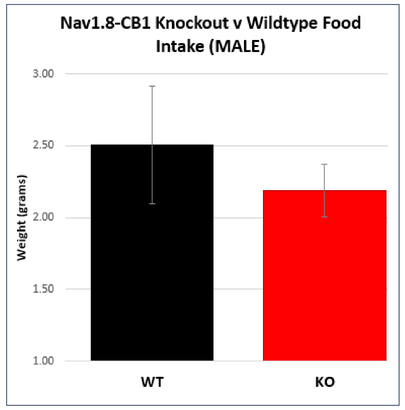

Figure 7. The average food intake for WT Males (2.5 g) is higher than that of KO Males (2.3 g). This suggests that in males, the CB1 receptor does have an influence on gastric behavior as it leads to an increase in food intake which is not present in the KO mice.

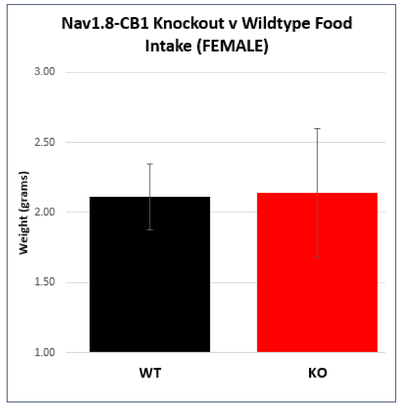

Figure 8. In females, the average between the WT females (2.2 g) and KO females (2.25 g) is significant yet small. As also proved in **Fig 6**, females are more resistant to gastric behavioral changes and did not experience as large as an impact because of the CB1 receptor in comparison to the male mice.

CONCLUSION

1. We were able to successfully breed sensory neuron-specific endocannabinoid receptor 1 "knock-out" mice, (Nav1.8-Cre$^{+/-}$CB1$^{fl/fl}$) which we were able to utilize in experiments with control mice to observe the impact of this receptor.
2. Preliminary findings of the Rate of Change of Body Weight Experiment/Food Intake Experiment: Male KO mice had a significantly less increase of body weight during the experiment than Control. Female KO mice had similar rates to Control, both resistant to HFD confirmed when compared with Male Control.

Future Work:

1. Increase *n* to obtain a more accurate statistical significance
2. After mice weigh ≥ 40g, RYGB will be performed and Rimonabant, a CB1 antagonist drug, will be applied to mice to conclude whether sensory neuron CB1 is fully or partially responsible for the previous findings that CB1 mediates effects of bariatric surgery.

ACKNOWLEDGEMENTS

I would like to thank Dr. Yi Chu for his mentorship and guidance, Dr. Mohamad Mokadem for the opportunity to conduct research in his lab, as well as the entire Mokadem Lab, and the Belin-Blank Center for making this opportunity possible.

REFERENCES

Mutations of the ANGPTL3 Coiled-coil Domain and their Impacts on Oligomerization and EL/LPL Binding and Inhibition

Param Sampat[1], Sydney Walker[2], Shwetha Shetty[2], Kelli Sylvers-Davie PhD[2], Brandon Davies PhD[2]

[1]Cedar Falls High School; [2]Department of Biochemistry and Molecular Biology, University of Iowa

THE UNIVERSITY OF IOWA

Background

Lipids are essential to the human body:
- Hormone precursors
- Digestive aids
- Energy stores
- Metabolic fuels
- Components of Cell Membrane

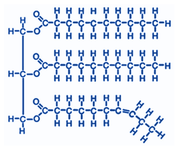

Relevant classes of lipoproteins
- Chylomicrons/Very low-density lipoproteins (VLDLs)
  - Transport fats in bloodstream to tissues
- HDL (High density lipoproteins)
  - "Good" cholesterol
  - Scavenges excess cholesterol back to liver

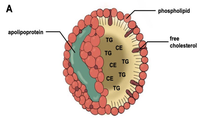

ANGPTL3
- Expressed by liver
- Inhibits EL and LPL
- Forms complex with ANGPTL8 to efficiently inhibit GPIHBP1 bound LPL
- Humans lacking functional ANGPTL3 have
  - Hypolipidemia
  - Protection from cardiovascular disease
  - Protection from type-2 diabetes

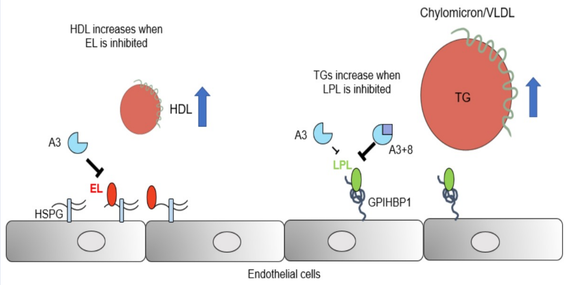

Objective of Study

Mutate ANGPTL3 proteins and analyze impact of said mutations on EL and LPL binding and inhibition to deduce regional function

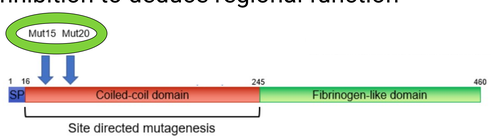

Methodology

Protein Expression:
- Culture cells
- Transient transfection
  - Nucleic acids artificially introduced into cells to produce proteins
- Protein harvesting
  - Cells dislodged/lysed & media and lysate collected
- Western Blotting (SDS & Native-page)
  - Protein separated using GE.
  - Separated proteins then transferred to membrane
  - Antibodies added and membrane imaged

Functional analysis:
- EL Inhibition Assay
  - Various concentrations of ANGPTL3 prepared
  - EL substrate added
  - Machine measures fluorescence
  - Decreased fluorescence = Increased activity
- LPL Inhibition Assay
  - Same as EL Inhibition assay except with LPL
- EL Binding Assay
  - LgBit on EL binds to smBit on ANGPTL3 when ANGPTL3 binds to EL
  - Luminescence produced illustrates whether binding properly occurs

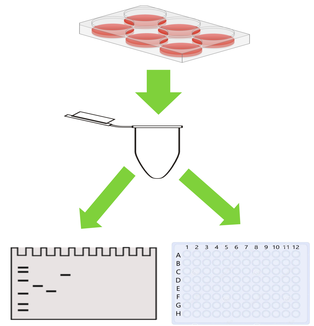

Western Blot Results

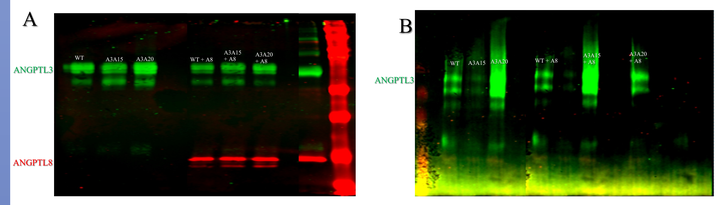

Figure 1. (A) *SDS-page Western blot of pEB14 (wild type), mutant pA15s (G66A Q67A), mutant pA20s (N76A I77A), and all cotransfected with ANGPTL8.* ***(B)*** *Native-page blot of aforementioned mutants and cotransfections. Trimer is maintained & all-look similar to wild-type, weak to no protein ANGPTL8 protein expression/visibility in blot.*

EL and LPL Inhibition Assay Results

Figure 2. (A) *EL Lipase activity after incubation at 37 C with increasing concentrations of wild-type or mutant ANGPTL3* ***(B)*** *LPL activity after incubation with increasing concentrations of wild type or mutant ANGPTL3*

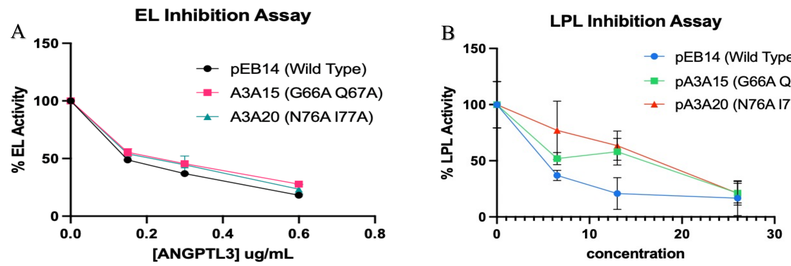

EL Binding Assay Results

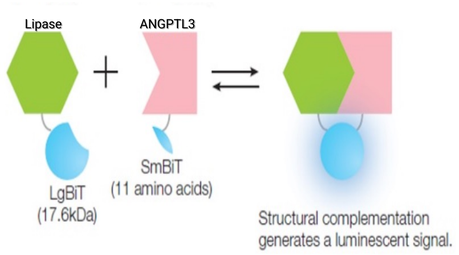

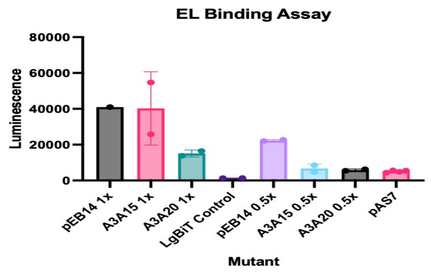

Figure 3. *Luminescence intensity indicates amount of binding in between EL and ANGPTL3. 1x A15 is very similar to WT, but A20 has significantly less binding in comparison to 1x WT*

Conclusions

ANGPTL3 Mutant G66A Q67A:
- Retained ability to inhibit LPL and EL
- Adequately bound to LPL
- Retained trimer

ANGPTL3 Mutant N76A I77A:
- Retained ability to inhibit EL
- Reduced ability in inhibiting LPL
- Retained trimer
- Appeared to suffer in EL binding

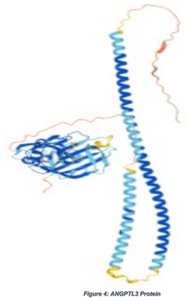

Figure 4: ANGPTL3 Protein

Broader Implications

- Step in the correct direction for Type-2 Diabetes and CVD sufferers.
- This research coupled with advancements later on may allow for specific mutagenic targeting of ANGPTL3 in order to decrease EL and LPL levels in a person to varying degrees.

Future Directions

- Perform LPL Binding Assays
- Continue analyzing different mutants within coiled-coil domain to expand scope of understanding
- Utilize KO drugs to analyze ANGPTL3 mutant impacts on live organisms

Acknowledgements

Belin-Blank Center, College of Education, The University of Iowa

I'd like to thank Dr. Davies and his lab, The Department of Biochemistry and Molecular Biology, and the University of Iowa

References

6. 2: What are lipids? (2018, April 13). Medicine LibreTexts. https://med.libretexts.org/Courses/American_Public_University/APUS%3A_Basic_Foundation_of_Nutrition_for_Sports_Performance_(Byerley)/06%3A_Lipids_Basics_-_Another_Energy_Source_for_the_Athlete/6.02%3A_What_Are_Lipids

Ahmad, Z., Banerjee, P., Hamon, S., Chan, K.-C., Bouzelmat, A., Sasiela, W. J., Pordy, R., Mellis, S., Dansky, H., Gipe, D. A., & Dunbar, R. L. (2019). Inhibition of angiopoietin-like protein 3 with a monoclonal antibody reduces triglycerides in hypertriglyceridemia. *Circulation*, *140*(6), 470–486. https://doi.org/10.1161/CIRCULATIONAHA.118.039107

Chen, Y. Q., Pottanat, T. G., Siegel, R. W., Ehsani, M., Qian, Y.-W., Zhen, E. Y., Regmi, A., Roell, W. C., Guo, H., Luo, M. J., Gimeno, R. E., Van't Hooft, F., & Konrad, R. J. (2020). Angiopoietin-like protein 8 differentially regulates ANGPTL3 and ANGPTL4 during postprandial partitioning of fatty acids. *Journal of Lipid Research*, *61*(8), 1203–1220. https://doi.org/10.1194/jlr.RA120000781

Chi, X., Britt, E. C., Shows, H. W., Hjelmaas, A. J., Shetty, S. K., Cushing, E. M., Li, W., Dou, A., Zhang, R., & Davies, B. S. J. (2017). ANGPTL8 promotes the ability of ANGPTL3 to bind and inhibit lipoprotein lipase. *Molecular Metabolism*, *6*(10), 1137–1149. https://doi.org/10.1016/j.molmet.2017.06.014

Dewey, F. E., Gusarova, V., Dunbar, R. L., O'Dushlaine, C., Schurmann, C., Gottesman, O., McCarthy, S., Van Hout, C. V., Bruse, S., Dansky, H. M., Leader, J. B., Murray, M. F., Ritchie, M. D., Kirchner, H. L., Habegger, L., Lopez, A., Penn, J., Zhao, A., Shao, W., … Baras, A. (2017). Genetic and pharmacologic inactivation of angptl3 and cardiovascular disease. *The New England Journal of Medicine*, *377*(3), 211–221. https://doi.org/10.1056/NEJMoa1612790

Feingold, K. R. (2000). Introduction to lipids and lipoproteins. In K. R. Feingold, B. Anawalt, M. R. Blackman, A. Boyce, G. Chrousos, E. Corpas, W. W. de Herder, K. Dhatariya, K. Dungan, J. Hofland, S. Kalra, G. Kaltsas, N. Kapoor, C. Koch, P. Kopp, M. Korbonits, C. S. Kovacs, W. Kuohung, B. Laferrère, … D. P. Wilson (Eds.), *Endotext*. MDText.com, Inc. http://www.ncbi.nlm.nih.gov/books/NBK305896/

Lee, E.-C., Desai, U., Gololobov, G., Hong, S., Feng, X., Yu, X.-C., Gay, J., Wilganowski, N., Gao, C., Du, L.-L., Chen, J., Hu, Y., Zhao, S., Kirkpatrick, L., Schneider, M., Zambrowicz, B. P., Landes, G., Powell, D. R., & Sonnenburg, W. K. (2009). Identification of a new functional domain in angiopoietin-like 3 (Angptl3) and angiopoietin-like 4 (Angptl4) involved in binding and inhibition of lipoprotein lipase (Lpl). *The Journal of Biological Chemistry*, *284*(20), 13735–13745. https://doi.org/10.1074/jbc.M807899200

Sylvers-Davie, K. L., Segura-Roman, A., Salvi, A. M., Schache, K. J., & Davies, B. S. J. (2021). Angiopoietin-like 3 inhibition of endothelial lipase is not modulated by angiopoietin-like 8. *Journal of Lipid Research*, *62*, 100112. https://doi.org/10.1016/j.jlr.2021.100112

Tarugi, P., Bertolini, S., & Calandra, S. (2019). Angiopoietin-like protein 3 (Angptl3) deficiency and familial combined hypolipidemia. *Journal of Biomedical Research*, *33*(2), 73–81. https://doi.org/10.7555/JBR.32.20170114

Tikka, A., & Jauhiainen, M. (2016). The role of ANGPTL3 in controlling lipoprotein metabolism. *Endocrine*, *52*(2), 187–193. https://doi.org/10.1007/s12020-015-0838-9

Development of ESP-8266 IoT device for efficient and low-cost transmission of hydrological data

Satvik Sandru[1], Yusuf Sermet[2], PhD, Muhammed Sit, PhD[2], Ibrahim Demir[2], PhD
[1]American High School, [2]University of Iowa, Department of Hydroinformatics

Belin-Blank Center
College of Education
The University of Iowa

UIHILAB
hydroinformatics.uiowa.edu

Introduction:

- **Hydroinformatics** is a field of informatics that encompasses hydrology and decision support systems
- **IoT devices** connect to the internet or other services & transmit or obtain data

Motivation:

- **Limited efficiency** in communicating hydrological information to researchers/workers
- **Insufficient coverage** of ESP 8266 board in the hydroinformtics field and K-12 setting
- Current general smart assistants **can not** comfortably provide **specific hydrological data** such as **stream height data** at a particular location

Fig. 5

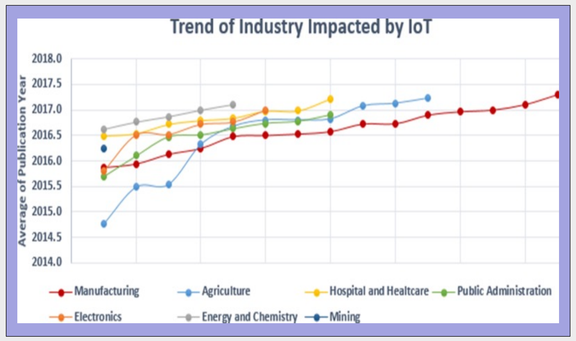

(Dachyar et al., 2019)

Outcome/Result:

- **Successfully developed** basic prototype that is appealing to K-12, & relays flood alert level with live time data streaming
- Utilized Node/Express.Js in order to communicate information from National Weather Service website (NWS) & United States Geological Survey webservice (USGS) & **effectively display this information on low-cost IoT device**

What promise does the implementation of Internet of Things (IoT) technology demonstrate in the domain of Hydrology and as an educational tool in order to expose K-12 to hydroinformatics?

Prototyping/Developmental Process & Future:

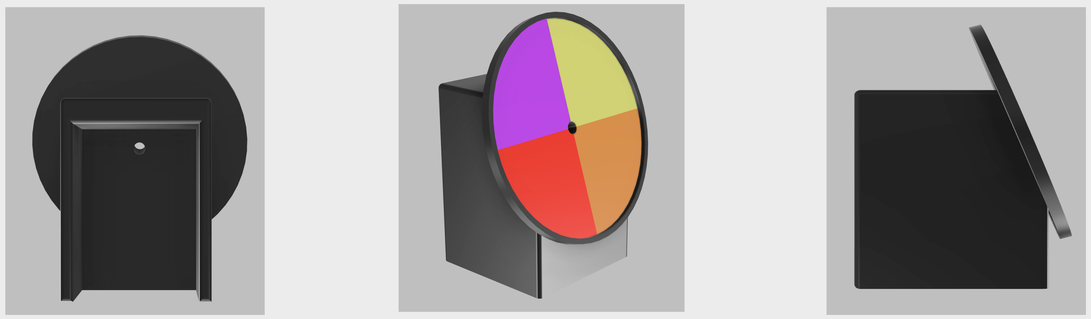

Fig. 1

```
**** START OF THE FLOW ****
USGS API URL: https://waterservices.usgs.gov/nwis/iv/?format=json&sites=05454500&parameterCd=00065
        Query string vals usgscode:05454500, threshold:1000, streamHeight:9.88
        Reading foreign_Id1 value from short file - 5454500:iowi4
NWS Full URL: https://water.weather.gov/ahps2/hydrograph.php?wfo=dvn&gage=iowi4
        Major Flood Stage alert value:26
        Moderate Flood Stage alert value:24.5
        Flood Stage alert value:23.5
        Action Stage alert value:21
        Low Stage (in feet) alert value:-9999
        Final alertVal:1
**** END OF THE FLOW ****
```

Fig. 2

This screenshot provides information gathered by the Node.Js server about live flood alert data and stream height values

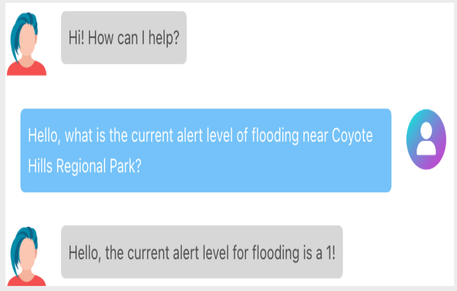

Fig. 3 Future example of user communication + ai capabilities

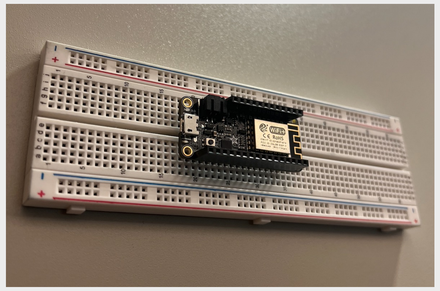

Fig. 4 ESP-8266 Board on Breadboard

Methodology

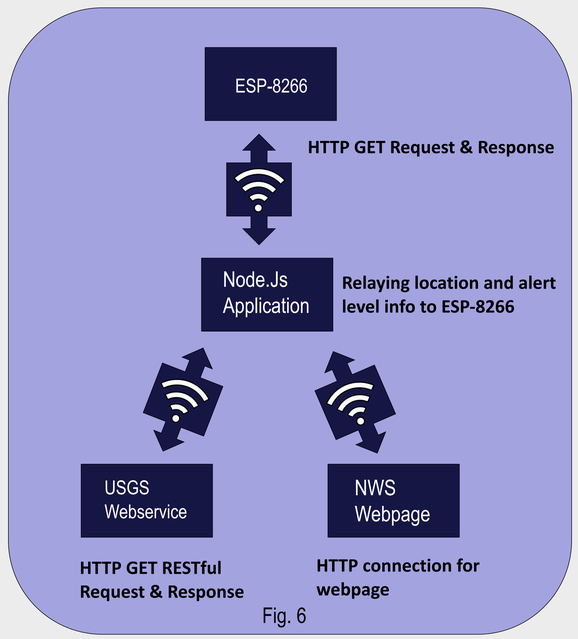

Fig. 6

Future Goals:

- Develop a more advanced ESP-8266 device with more hydrological data output capabilities, and **voice input integration** for researchers/workers

Fig. 7

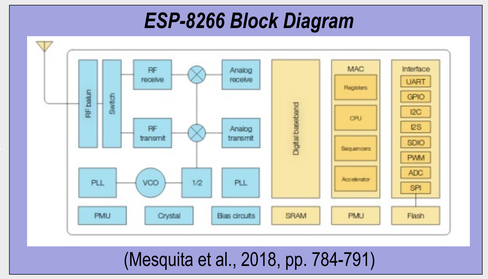

(Mesquita et al., 2018, pp. 784-791)

- Construct a simple IoT kit that will educate K-12 about IoT technology/hydroinformatics in a **beginner friendly** manner

References

https://docs.google.com/document/d/1xCqCMSym2nbfSiu5jRsYNEOb00tfZGgY0hADigBJSik/edit?usp=sharing/

Special Thanks To:

- SSTP and the Belin-Blank center for this opportunity
- Dr. Ibrahim Demir and the UIHI Lab for close mentorship
- Yusuf Sermet and Muhammed Sit for assisting me with innumerable technical issues

Synthesis and Characterization of a Series of Polymers with Conjugated -NS- and -NSS- Backbones

Atman Shah[1], Jolene Cao[2], Shanari Wickremsinghage[3], Ned B. Bowden, Ph.D.[3]

[1]Archbishop Mitty High School, [2]Smithtown High School East, [3]Department of Chemistry, University of Iowa

Introduction

Polythiazyl, first synthesized in 1910, is an inorganic polymer composed entirely of alternating nitrogen and sulfur atoms. Its characteristics include superconductivity at low temperatures (critical point of 0.3K) and a conjugated backbone. However, polythiazyl is also liable to decomposition in air (McDiarmid et al., 1976).

Previous work has shown that modifications to the poly(NS) backbone yield more stable polymers. The polymerization of anilines to yield poly[(N,N-amino)sulfide] polymers revealed that the color depended on the conjugated backbone (Paudel et al., 2023). Additionally, our lab has reported the synthesis of poly[N,N-(phenylamino) disulfides], yielding polymers with a poly(NSS) backbone. The color of these polymers was dependent on the substituents around the aromatic ring (Grace et al., 2021).

Another application is hydrogen sulfide (H_2S) release. H_2S is an important gasotrasmitter and has been shown to promote crop growth, but it is toxic at high concentrations. N-S bond-containing compounds have been shown to release H_2S in the presence of thiols (Grace et al., 2021). Poly(NS) polymers have backbones made exclusively of N-S bonds, making H_2S release an area of significant interest.

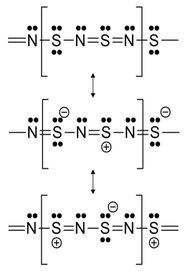

Fig. 1: Resonance structure of polythiazyl

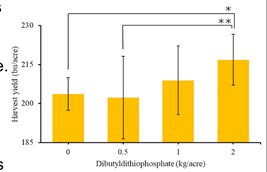

Fig. 2: H_2S release promotes crop growth (Grace et al., 2021)

Methods

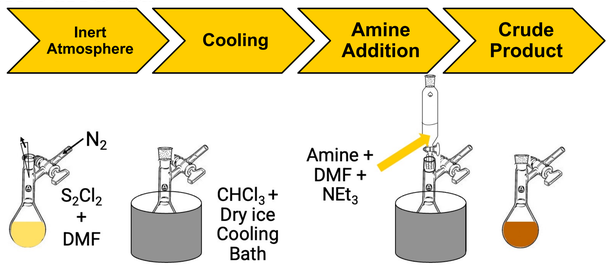

Fig. 3: DMF is used to convert S_2Cl_2 into SCl_2, before the amine is added dropwise to create the polymer.

Fig. 4: Purification of the polymers begins with vacuum filtration, followed by aqueous workup and *in vacuo* concentration.

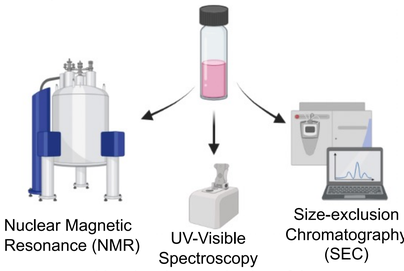

Fig. 5: Spectroscopy enables the characterization of the structure, color, and size of our polymers.

Results

General Monosulfide Polymerization Scheme

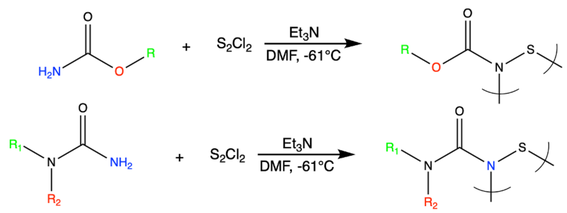

Fig. 6: Monosulfide polymers were synthesized in DMF at -61°C.

Monomers Studied

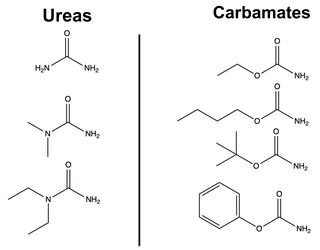

Fig. 7: Three ureas and four carbamates were studied.

Effects of Varying Substituents On Polymerization

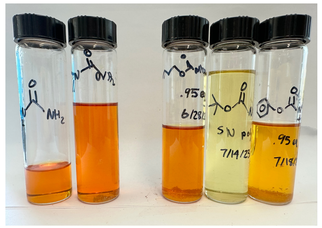

Fig. 8: From left to right, urea, 1,1-dimethylurea, butyl carbamate, *t*-butyl carbamate, phenyl carbamate

Deprotection of the -NS- Backbone

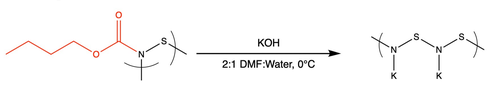

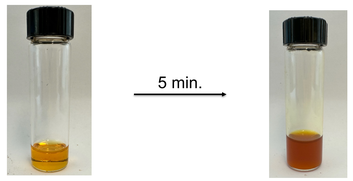

Fig. 9: Butyl carbamate polymer changes color within five minutes of KOH addition

Effects of Different Molar Ratios of Amine:S_2Cl_2 On Polymerization

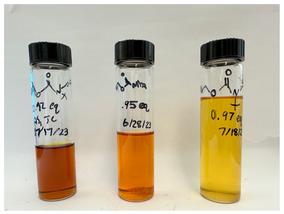

Fig. 10: From left to right, 0.92, 0.95, and 0.97 equivalences of butyl carbamate

Molar Ratios (Amine : S_2Cl_2)	Color	Solubility
0.92:1	Dark red	Soluble in brine and water
0.95:1	Orange	Insoluble in brine and water
0.92:1	Yellow	Soluble in brine and water

Rapid Polymerization Enables 2-D Printing

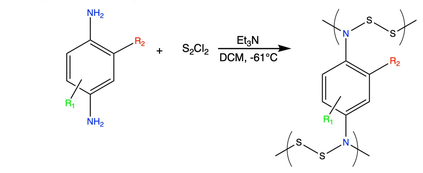

Fig. 11: General diamine disulfide polymerization scheme.

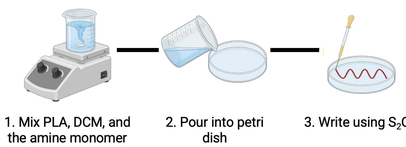

Fig. 12: Workflow for 2-D Printing through rapid polymerization of amines in the presence of S_2Cl_2.

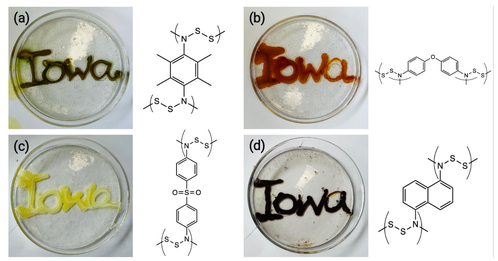

Fig. 13: -NSS- polymers synthesized from the following monomers (a) 2,3,5,6-Tetramethyl-1,4-phenylenediamine (b) 4,4'-Oxydianiline (c) 4,4'-sulfonyldianiline (d) 1,5-Diaminonaphthalene.

NMR Spectra

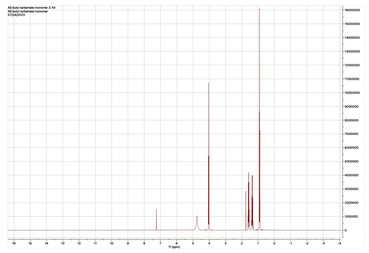

Fig. 14: NMR spectra of butyl carbamate monomer. Peaks are clearly defined, and the amine singlet and alkyl chain multiplets are visible.

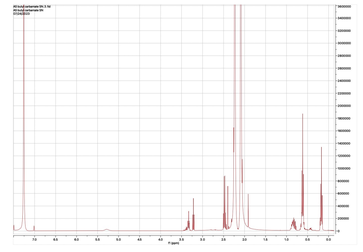

Fig. 15: NMR spectra of butyl carbamate polymer. Peak broadening is observed. Solvent (DMF) is also present.

Conclusions

- We report the synthesis of polymers with conjugated –NS– and –NSS– backbones.
- The colors of these polymers arise from energy band gaps in the conjugated backbone.
- Different equivalences of amine affect polymer characteristics and yield.
- Cross-linked –NSS– polymers enable rapid 2D printing

Future Work

- Cleaving off R-groups from the -NS- backbone
- Quantifying the rate of hydrogen sulfide release of the polymers
- Doping the polymers with oxidants (e.g., Br_2) and testing electrical conductivity.
- Synthesizing polycyclic polythiazyl derivatives

Acknowledgements

I would like to thank Professor Bowden and Shanari for their mentorship during this program. I also thank the University of Iowa and the SSTP program for giving me this opportunity, as well as the other members of the Bowden Group for their support.

References

1. Grace, J. P., & Bowden, N. B. (2021). Synthesis and hydrogen sulfide releasing properties of Diaminodisulfides and dialkoxydisulfides. *ACS Omega*, *6*(27), 17741–17747. https://doi.org/10.1021/acsomega.1c02585
2. Grace, J. P., Flitz, E. S., Hwang, D. S., & Bowden, N. B. (2021). Polymerization of aniline derivatives to yield poly[n,n-(phenylamino)disulfides] as polymeric auxochromes. *Macromolecules*, *54*(22), 10405–10414. https://doi.org/10.1021/acs.macromol.1c01548
3. Guo, B., Glavas, L., & Albertsson, A.-C. (2013). Biodegradable and electrically conducting polymers for biomedical applications. *Progress in Polymer Science*, *38*(9), 1263–1286. https://doi.org/10.1016/j.progpolymsci.2013.06.003
4. MacDiarmid, A. G., Mikulski, C. M., Saran, M. S., Russo, P. J., Cohen, M. J., Bright, A. A., Garito, A. F., & Heeger, A. J. (1976). Synthesis and selected properties of polymeric sulfur nitride, (polythiazyl), $(SN)_x$. *Inorganic Compounds with Unusual Properties*, 63–72. https://doi.org/10.1021/ba-1976-0150.ch006
5. Paudel, A., Campbell, E. J., Van Benschoten, W. Z., Otting, G. W., Shepherd, J. J., & Bowden, N. B. (2023). Polymerization of primary amines with sulfur monochloride to yield red polymers with a conjugated SN Backbone. *Macromolecules*, *56*(10), 3721–3730. https://doi.org/10.1021/acs.macromol.2c02507

Bibliometric Analysis of Hydrology Research Using Automated Data Mining and TF-IDF With Latent Dirichlet Allocation

Kevin Song[1], Carlos Erazo Ramirez[2], M.Sc., Yusuf Sermet[2], PhD., Ibrahim Demir[2], PhD.
[1]Deerfield High School, Deerfield, IL, [2]Stanley Hydraulics Laboratory, College of Engineering, University of Iowa, Iowa City, IA

Introduction

Environmental and hydrological sciences have been enriched by hardware and software research output over the past decades. New technologies and developments making significant impacts every year.

Technology such as sensors and physical modeling have been used for centuries to analyze river flow, landslides, and remote sensing. However, the recent boom in computing, artificial intelligence, and other innovations just in the last decade has caused significant changes in research methodologies and led to novel solutions to modern problems. Especially with the alarming rise in climate change, rise in sea levels, and conflict over water scarcity, it is more important than ever for hydrology research to constantly look for new options, as well as analyze the successes and failures of past research.

Editors of various hydrological journals allow us to efficiently obtain article, journal, and author metadata through the use of APIs and automated data mining.

Research Goals

This study aims to understand the technological adoptions in the field of hydrological science and the contexts in which they are employed. We also seek to analyze past and future trends in their uses, as well as collaborations between institutions and across international borders through hydrological research.

By discovering connections between specific technology and which hydrological fields they are employed, our research hopes to uncover potential uses of technology in fields that have not yet used them to their full potential. We also hope to use contextualize popular technologies that are currently being explored with their past employment.

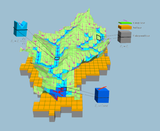

Fig 1.1: Satellite used for hydrological scanning and mapping
Fig 1.2: Drone employed in remote sensing and aerial data collection
Fig 1.3: A 3-D surface model and simulation of watershed river flow

Methodology

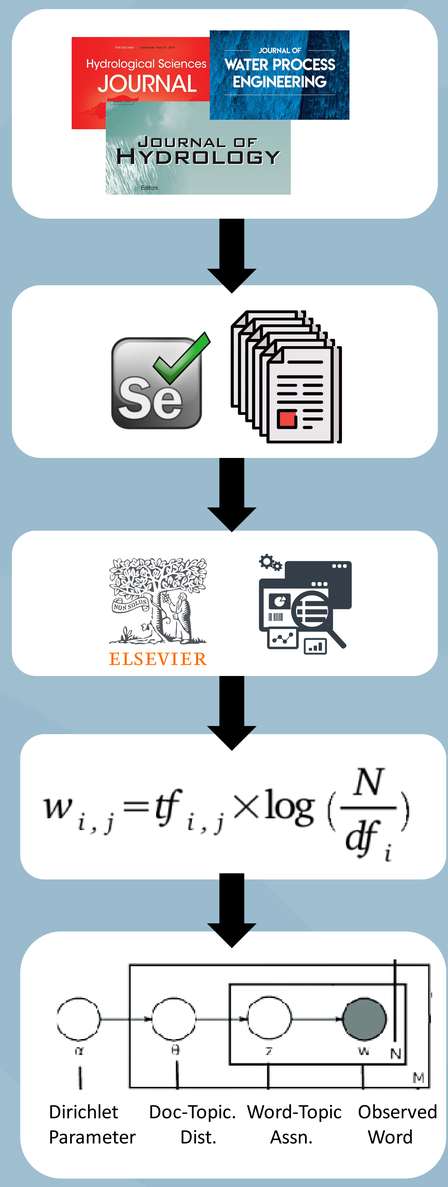

Results

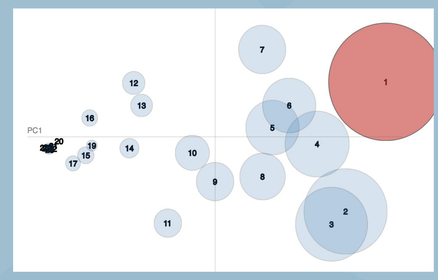

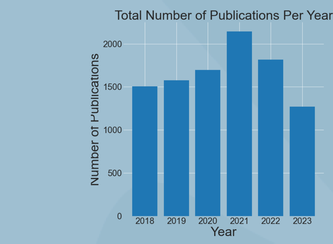

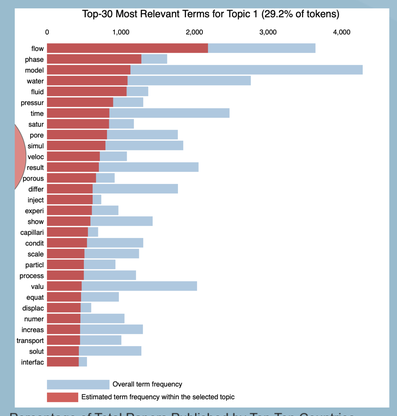

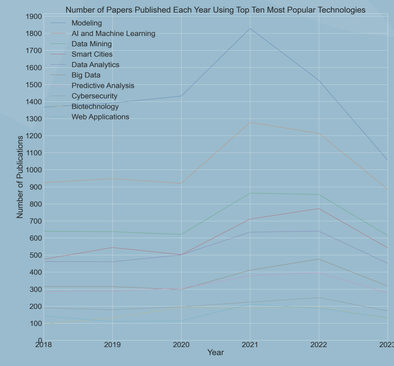

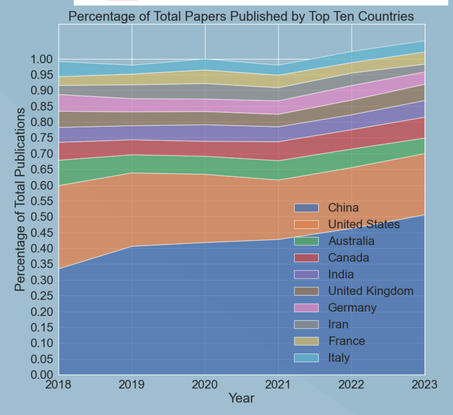

Conclusion and Future Research

The trends over the past five years have reflected recent technological developments. For example, Artificial intelligence and big data have remained popular throughout the years. Modeling and Web Applications have likely remained stable over the past decade. Among the most popular hydrological subfields include groundwater and rainfall modeling, as well as chemical hydrology. These results are important because it reveals new technologies, like biotechnology, that one might not have considered to be applicable to hydrology research but are actually prevalent. Although it is not used as often as things like AI and modeling, it is nonetheless worth consideration for further investigation into its implications.

In the future, we would like to repeat the same study to see how the field of hydrology and its subfields have further evolved, as well as testing other classification algorithms while using a more comprehensive list of buzzwords.

IIHR—Hydroscience and Engineering

References & Acknowledgements

I would like to thank the Belin-Blank Center and SSTP Program for providing this research opportunity for me, as well as Carlos Ramirez, Yusuf Sermet, and Professor Demir for guiding me on my five-week experience.

Wang, K., & Herr, I. (2022). Machine-Learning-Based bibliometric analysis of pancreatic cancer research over the past 25 years. *Frontiers in Oncology*, *12*. https://doi.org/10.3389/fonc.2022.832385
Chang, I., Horng, J., Liu, C., Chou, S., & Yu, T. (2022). Exploration of topic classification in the tourism field with text mining technology—a case study of the academic journal papers. *Sustainability*, *14*(7), 4053. https://doi.org/10.3390/su14074053

The Effect of Circadian Rhythm Disruptions on Serotonin Neurons and Time-of-day Dependent Serotonergic Chemosensitivity

Zirui Song[1,2], Benjamin L Kreitlow[3-6], and Gordon F Buchanan[3-6]

[1]Horace Greeley High School, Chappaqua, NY, USA, [2]Secondary Student Training Program, [3]Medical Scientist Training Program, [4]Interdisciplinary Graduate Program in Neuroscience, [5]Iowa Neuroscience Institute, [6]Department of Neurology, University of Iowa Carver College of Medicine, Iowa City, IA, USA

Introduction

- Epilepsy is a neurological disease associated with spontaneous seizures.
- 1 in 26 people will develop epilepsy within their lifetime[1].
- Sudden unexpected death in epilepsy, or SUDEP, is a phenomenon where seizures result in death.
- SUDEP occurs more frequently during the night[2,3].
- Nocturnal mouse models of seizure-associated death are also more likely to die during the night[2,3].
- The mechanism driving nighttime risk of death in SUDEP is *unknown.*
- The neurotransmitter serotonin (5-HT) is a compelling target of study, due to its known daily fluctuations in the brain[2,3], relationship with seizure mortality and severity, and role in CO_2 chemosensitivity[4-6].

HYPOTHESES

1. Disruption of the circadian rhythm (viral ablation, electrolytic lesion, and genetic deletion) will result in fewer serotonin neurons.
2. 5-HT-associated CO_2 chemosensitivity (CO_2 arousal and the hypercapnic ventilatory response, HCVR) is time-of-day-dependent with the lowest response during the night in wild-type animals and low regardless of time of day in mice lacking 5-HT neurons in the brain.

Materials and Methods

Experiment #1 – Neuroanatomy

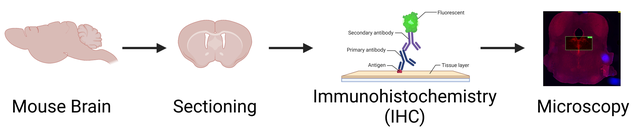

Experiment #2 –Serotonin Physiology

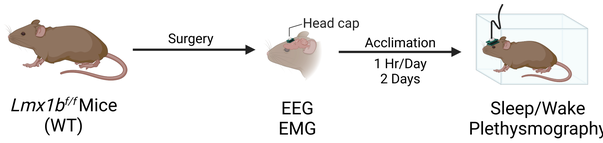

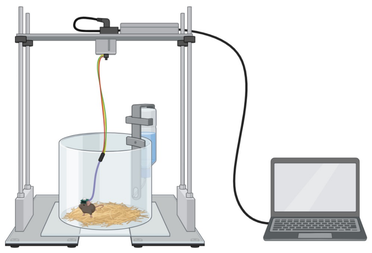

Graphical Abstract

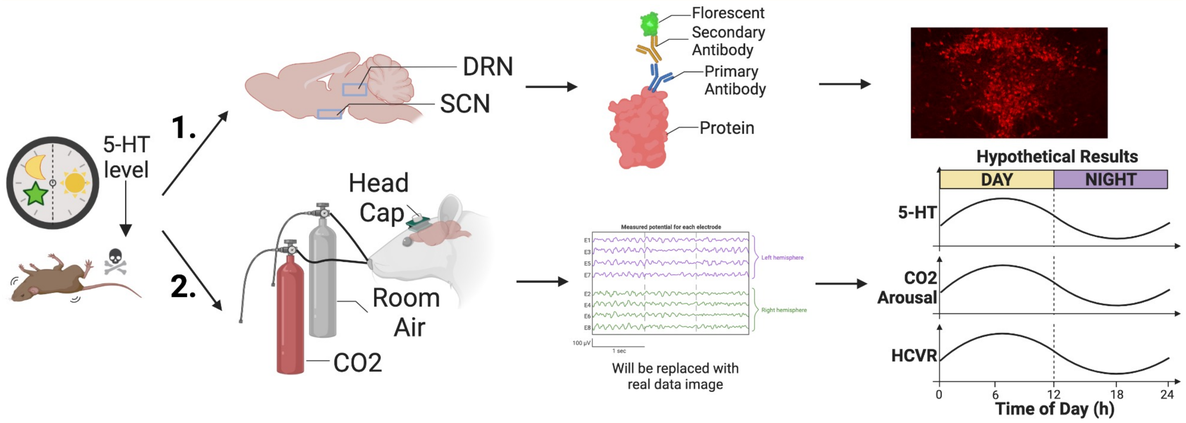

Results

Experiment #1 – Neuroanatomy

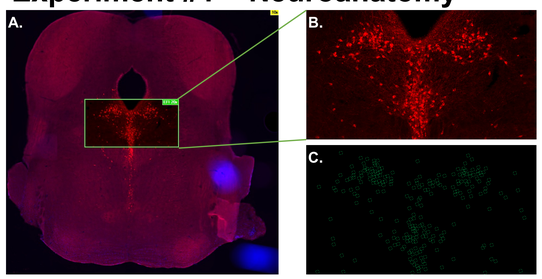

Figure 1. Fluorescent IHC was used to label TPH2+ 5-HT neurons in the DRN. A, A zoomed out image of a representative coronal section containing the DRN. **B,** Comparable zoomed in images just ventral to the cerebral aqueduct were used for cell counting experiments. **C,** TPH2-positive neurons were counted and secondarily verified by another scientist.

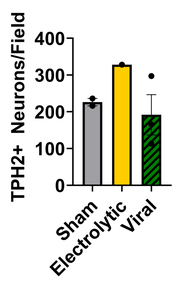

Figure 2. Number of TPH2+ neurons in the DRN following lesion. Preliminary cell counting studies demonstrate more TPH2+ neurons following electrolytic lesioning compared to sham and viral ablation groups.

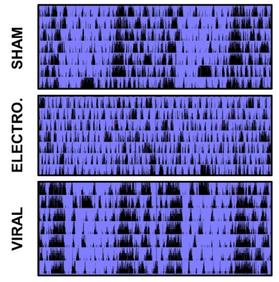

Figure 3. Actograms from each lesion strategy. Motion sensors were used to capture locomotor activity. Electrolytic-lesioning, but not attempted viral ablation, resulting in arrhythmic locomotor activity in constant darkness.

Experiment #2 – Development of an Open-Loop Trigger and Serotonin Physiology

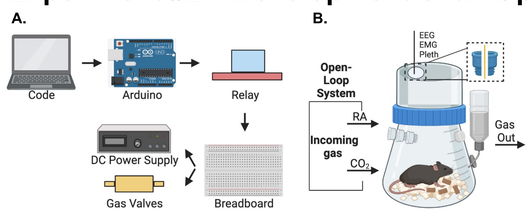

Figure 4. A novel open-loop system was developed to trigger gas challenges at specific times of the day automatically. A, A flow chart that shows the design of the system. Gas switches were controlled by a programmable microcontroller (Arduino Uno) interfacing with a real-time clock using the open-loop system. **B,** The graphical demonstration of the system set-up with a newly created Plethysmography chamber where Mice were placed in a novel plethysmography chamber with access to food, water, and bedding, which allows for overnight experiments.

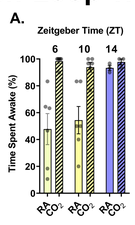

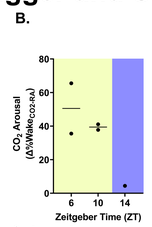

Figure 5. Time-of-day-dependent rhythm in CO_2 arousal was measured by comparing amount of time awaking under CO_2 conditions compared to baseline (room air) conditions. **A,** Bar graph demonstrates the percentage of wake under RA and CO_2. **B,** The difference between the percentage of awake in RA and CO_2

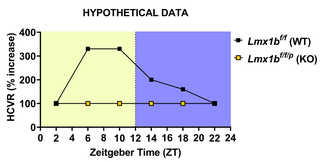

Figure 6. Time-of-day-dependent rhythm in hypercapnic ventilatory response (HCVR) will be quantified by comparing ventilation (volume of air moved through lungs) under CO_2 versus room air conditions. When ZT=8, *Lmx1b*$^{f/f}$ has the fastest showing an increase in breathing rates with rhythm.

Discussion/Conclusion

Neuroanatomy: Electrolytic lesioned mice have more DRN 5-HT neurons than sham lesioned & dual viral ablation mice.

Open-Loop System: reduce experimental confounds and improve time-of-day-dependent experiments in the future.

CO_2 arousal and HCVR: wild-type (*Lmx1b*$^{f/f}$) mice demonstrate time-of-day-dependent variability in CO_2 arousal and HCVR.

In the future, **chronotherapeutic strategies** that influence serotonergic physiology could be leveraged to reduce the nighttime risk of death for people living with epilepsy.

Future Directions

1. **Find time-of-day-dependent regulation of 5-HT-associated genes** (tryptophan hydroxylase, TPH & serotonin transporter proteins).
2. **Study how seizures at different times of day affect serotonergic physiology** (induce seizures followed by an automatic gas challenge).
3. **Investigate the serotonergic physiology (CO_2 arousal and HCVR) in *Lmx1b*$^{f/f/p}$ (5-HT knock-out) animals**.
4. **Explore alternative serotonin physiologies** (autoresuscitation & post-ictal generalized electroencephalography suppression)

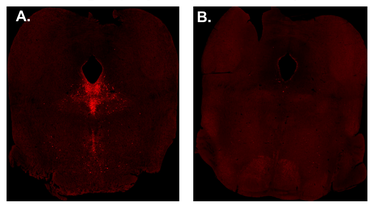

Figure 7. Representative IHC from mice lacking serotonin neurons and wild-type littermates. A, wild-type (*Lmx1b*$^{f/f}$) and **B,** knock-out (*Lmx1b*$^{f/f/p}$).

Acknowledgments

This work was supported by the NIH/NIGMS T32 CM007337 (to Iowa MSTP), NIH/NINDS R01 NS095842 (to GFB), NIH/NINDS R01 NSNS129722 (to GFB), Cure Epilepsy Award - The Joanna Sophia Foundation (to GFB), and the Beth L. Tross Epilepsy Professorship (to GFB).

References

1. Hesdorffer, D. C., Logroscino, G., Benn, E. K. T., Katri, N., Cascino, G., and Hauser, W. A. 2011. Estimating risk for developing epilepsy: a population-based study in Rochester, Minnesota. *Neurology, 76*(1): 23 – 27. https://doi.org/10.1212/WNL.0b013e318204a36a
2. Kreitlow, B. L., Li, W., & Buchanan, G. F. (2022). Chronobiology of epilepsy and sudden unexpected death in epilepsy. *Frontiers in Neuroscience, 16*. https://doi.org/10.3389/fnins.2022.936104
3. Purnell, B.S., Thijs R. D., and Buchanan, G. F. 2018. Dead in the Night: Sleep-Wake and Time-Of-Day Influences on Sudden Unexpected Death in Epilepsy. *Frontiers in Neurology. 9:* 1079. http://doi.org/10.3389/fneur.2018.01079. eCollection 2018
4. Buchanan, G. F., & Richerson, G. B. (2010). Central serotonin neurons are required for arousal to CO2. *Proceedings of the National Academy of Sciences*, *107*(37), 16354–16359. https://doi.org/10.1073/pnas.1004587107
5. Hodges, M. R., Tattersall, G. J., Harris, M. B., McEvoy, S. D., Richerson, D. N., Deneris, E. S., Johnson, R. L., Chen, Z.-F., & Richerson, G. B. (2008). Defects in breathing and thermoregulation in mice with near-complete absence of central serotonin neurons. *The Journal of Neuroscience*, *28*(10), 2495–2505. https://doi.org/10.1523/jneurosci.4729-07.2008
6. Petrucci, A. N., Joyal, K. G., Purnell, B. S., & Buchanan, G. F. (2020). Serotonin and sudden unexpected death in epilepsy. *Experimental Neurology*, *325*, 113145. https://doi.org/10.1016/j.expneurol.2019.113145

Examining the Neurocognitive Differences in FVIII Deficiency (Hemophilia A) by Comparing Neuro-inflammatory Marker Expression and Behavior Test Analysis

Katie Sun[1], Danielle York[2], Kevin Gubner[2], Janice Staber, MD[2]

[1]Crystal Springs Uplands School, [2]Department of Pediatrics, University of Iowa Stead Family Children's Hospital

University of Iowa Stead Family Children's Hospital

Background

Hemophilia A (Factor VIII deficiency) is a bleeding disorder caused by defective or missing Factor VIII, a blood clotting protein.

- Hemophilia A is associated with neurophenotypic differences including increased cerebral microbleeds, mental health disorders, and decreased brain volumes in hemophilia patients (Al-Huniti et al., 2019, 2020).
- Staber lab has found significant differences in select neuro-inflammatory marker expression between human hemophilia and heathy patients.

Staber Lab Pilot Studies

Elevated rates of neuro-inflammation based on activated microglia morphology

Increased anxiety-like and depression-like behavior in HA mice

Elevated expression of inflammatory markers in the cerebellum and brain stem

Research Objectives

1. Measure the relative gene expression of pro-inflammatory and pro-repair markers in 6-week FVIII deficient (hemophilia) mice.
2. Examine anxiety-like behaviors in hemophilia mice compared to wild type based on behavior test data.

Determine if 6-week hemophilia mice express similar neurocognitive and behavioral differences observed in older 6-month mice and human patients.

Methods

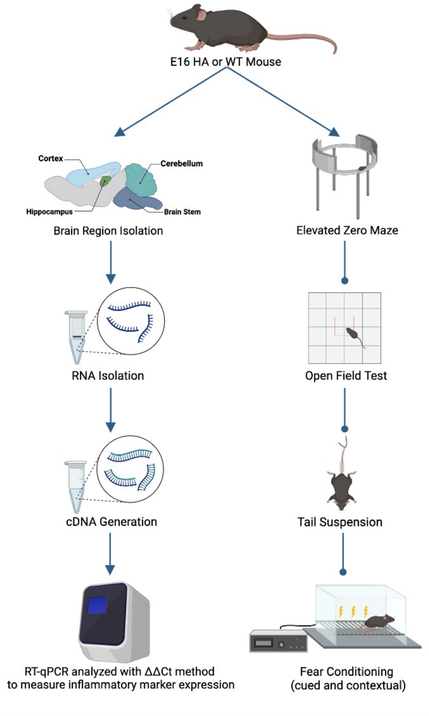

Results

RT-qPCR Relative Gene Expression

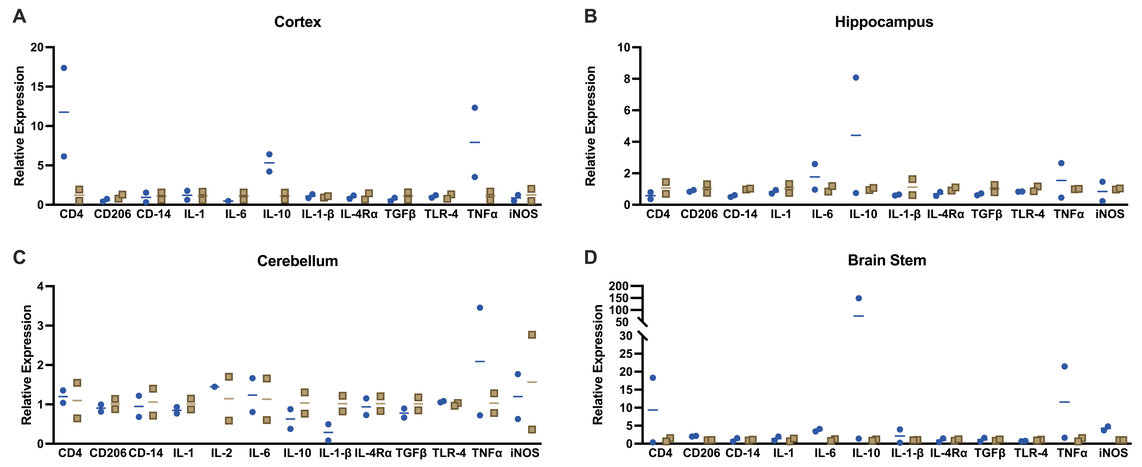

Figure 1. Neuroinflammatory Marker Relative Expression WT vs. HA
(A) CD4, IL-10, and TNFα expression appear elevated in the cortex of HA mice. **(B)** IL-6 and IL-10 expression trend upward in the hippocampus of HA mice. **(C)** TNFα expression is increased in the cerebellum of one HA mouse but is decreased compared to WT in the second HA mouse. **(D)** One mouse (H76-1) in particular shows increased expression; the average relative expression in the brainstem of HA mice trends upwards for CD4, IL-6, IL-10, Il-1β, TNFα, and iNOS.

Behavioral Tests

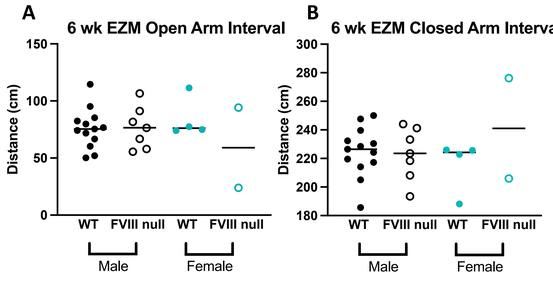

Figure 2. Elevated Zero Maze
(A) HA and WT males have similar average times in the closed arm of the EZM; HA females trend towards increased time spent in the closed arm. **(B)** Time spent in the open arm of the EZM is not significantly different between WT and HA males; HA females trend towards lower time intervals spent in the open arm.

Types of Behavioral Tests

Name	Purpose
Elevated Zero Maze	Measures anxiety-like behavior in mice by analyzing time spent in closed (higher for anxiety-like) or open (lower for anxiety-like) arms of the maze.
Open Field Tests	Measures anxiety-like behavior in mice by analyzing time spent in the periphery/outer edge (higher for anxiety-like) or center (lower for anxiety-like) arms of the field/box.
Tail Suspension	Measures depression-like behavior in mice by analyzing time immobile (higher for depression-like) or mobile while hanging by the tail.
Fear Conditioning (cued and contextual)	Assesses learning and memory by delivery a shock to a tone one day and observing the reaction to the same tone after. Acts as a metric for anxiety and fear in mice.

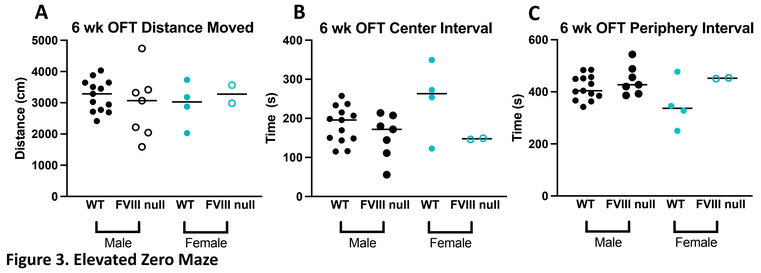

Figure 3. Elevated Zero Maze
(A) HA and WT males and females do not move significantly different distances. **(B)** HA males and females trend towards more time spent in the outer edge of the open field compared to WT. **(C)** HA males and females appear to spend less time in the center of the open field compared to WT.

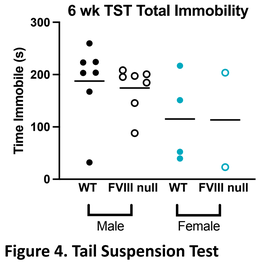

Figure 4. Tail Suspension Test
FVIII null mice do not have significantly different times immobile compared to WT mice of the same sex.

Conclusions

1. Initial results from 2 HA and 2 WT 6-week mice show trends towards increased neuroinflammation in the brains on HA mice, especially relative expression of pro-inflammatory markers in various brain regions.
   Markers trending towards increased expression:
   - Pro-inflammatory: IL-6 (hippocampus, brain stem), TNFα (cortex, cerebellum of one mouse, brainstem), iNOS (brain stem), CD4 (cortex, brain stem), Il-1β (brain stem)
   - Pro-repair/Anti-inflammatory: IL-10 (cortex, hippocampus, brain stem)
2. Hemophilia mice demonstrated increased anxiety-like behaviors but interestingly no significant differences in depression-like behaviors, which could signal a lack of depressive phenotype; increased rates of depression observed could be a result of hemophilia as a chronic disease as opposed to a result of FVIII deficiency.

This research adds to previous neuro-inflammatory studies conducted on 6-month hemophilia mice, which also showed a trend towards increased neuroinflammation. The combination of inflammatory marker expression and behavioral tests connect observed neurocognitive differences and mental health disorders with internal markers or causes of neuro-cognitive function and processes in FVIII deficient patients.

Future Directions

1. Increased sample size – use a power test to determine the number of mice needed to produce statistically significant results.
2. Continue expanding the age range of mice studied in order to reveal more about the relationship between neuro-inflammation and hemophilia.
3. Utilize knowledge about the neuro-cognitive component of FVIII deficiency to improve treatment for Hemophilia A patients.

Acknowledgements

I would like to thank Dr. Staber for welcoming me into her lab and giving me the opportunity to contribute to her research. Special thanks to Danielle York for her generous mentorship this summer, as well as Kevin Gubner for his help with qPCR and data analysis. I would also like to thank the SSTP program and Belin Blank Center for curating this summer research experience.

Images created with Biorender. PRISM Graphpad was used for graph generation and data analysis.

References

Al-Huniti, A., Reyes Hernandez, M., Ten Eyck, P., & Staber, J. M. (2020). Mental health disorders in haemophilia: Systematic literature review and meta-analysis. *Haemophilia*, *26*(3), 431-442. https://doi.org/10.1111/hae.13960

Al-Huniti, A., Harshman, L. A., Novak, M., Nopoulos, P., & Staber, J. M. (2019). Brain anomalies in children with severe factor VIII deficiency- a pilot study. *Blood*, *134*(Supplement 1), 1121. https://doi.org/10.1182/blood-2019-131804

Buranahirun, C., Walsh, K. S., Mrakotsky, C., Croteau, S. E., Rajpurkar, M., Kearney, S., Hannemann, C., Wilkening, G. N., Shapiro, K. A., & Cooper, D. L. (2019). Neuropsychological function in children with hemophilia: A review of the hemophilia growth and development study and introduction of the current eTHINK study. *Pediatric Blood & Cancer*, *67*(1). https://doi.org/10.1002/pbc.28004

Fu, S. P., Chen, S. Y., Pang, Q. M., Zhang, M., Wu, X. C., Wan, X., Wan, W. H., Ao, J., & Zhang, T. (2022). Advances in the research of the role of macrophage/microglia polarization-mediated inflammatory response in spinal cord injury. *Frontiers in immunology*, *13*, 1014013. https://doi.org/10.3389/fimmu.2022.1014013

Troubat, R., Barone, P., Leman, S., Desmidt, T., Cressant, A., Atanasova, B., Brizard, B., El Hage, W., Surget, A., Belzung, C., & Camus, V. (2020). Neuroinflammation and depression: A review. *European Journal of Neuroscience*, *53*(1), 151-171. https://doi.org/10.1111/ejn.14720

Sea Spray Aerosol Particles' Morphologies and Phase States under the Wind Speed of ~19 m/s

Mengnan Sun, Chamika K. Madawala, Alexei V. Tivanski

Introduction

- Sea Spray Aerosols (SSAs) are generated from the air bubbles entrained from the breaking of sea waves.
- SSAs can influence Earth's radiative budget both directly and indirectly.
- SSAs are highly variable and unpredictable, so we need to examine them on an individual particle level to see their effects on the climate.
- The Atomic Force Microscopy (AFM) has been proven to be an effective way to analyze individual SSA particles.
- SSAs have different morphologies and phase states under different relative humidity (RH).
- The wind speed of 1600 rpm generated by a fan simulates a wind speed of 19.1 m/s at 10 m height above the ocean surface.

Objective

Investigating the morphologies and phase states of SSA particles sized from ~70 to 1200 nm under the wind speed of 19 m/s.

Instrumentation

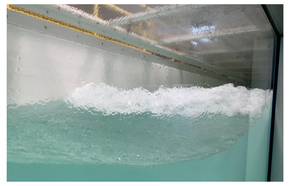

1. Fill the tank with collected seawater and use a fan to simulate a wind speed of 1600 rpm (approximately 19.1 m/s).

2. Deposit SSA particles onto the hydrophobically coated silicon substrates in the MOUDI.

3. Get the particle scans and force plots using the AFM instrument

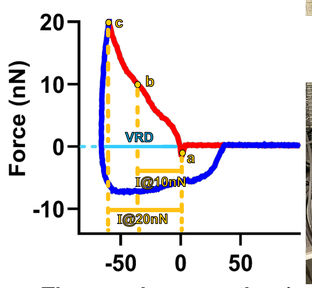

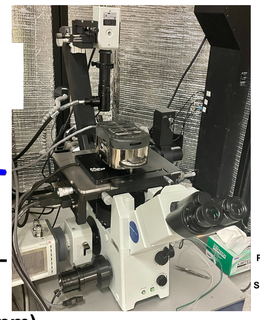

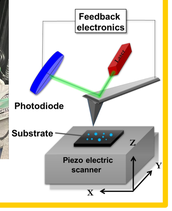

Methodology

I. Determine the **morphologies** of each particle using the **images scanned by the Atomic Force Microscope (AFM)**

II. Determine **if a particle is a liquid** using the **force plots** and the **Relative Indentation Depth (RID) formula**

i. Measure the indentations **at 20 nN** on the force plots of the particle

ii. Use the Height image scanned by the AFM to determine the particle height

iii. $\mathbf{RID} = \frac{Indentation}{Particle\ Height}$ (Larger RID value = softer particle; smaller RID value = stiffer particle)

iv. If RID > **0.95**, the particle is in liquid state; otherwise, it is either a solid or semisolid

III. Determine if a particle is **a solid or a semisolid** using the **force plots** and the **Viscoelastic Response Distance (VRD) formula**

i. **Smooth** the force plots to ensure that the noise during the experiment did not affect the results measured at a particular RH

ii. Measure the distance (**in nm**) between the approach and retract curves **at 0 nN**, and this value is the VRD

iii. If VRD < **0.5**, the particle is a solid; otherwise, it is a semisolid (only if its RID ≤ 0.95)

Results

Morphologies observed among SSA particles sized ~70 to 1200 nm under the wind speed of 19.1 m/s:

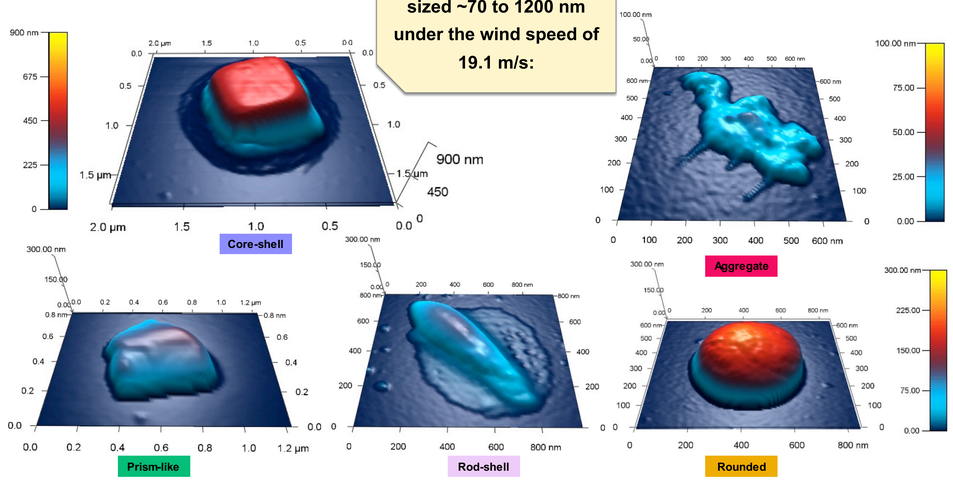

SSA Particles' Morphology Distribution under the Wind Speed of ~19m/s

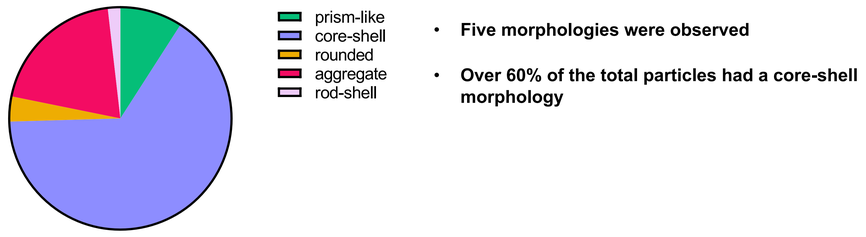

- **Five morphologies were observed**
- **Over 60% of the total particles had a core-shell morphology**

Core-shell shaped SSA particles' phase state distribution at 20% and 60% RH (measured at their shells):

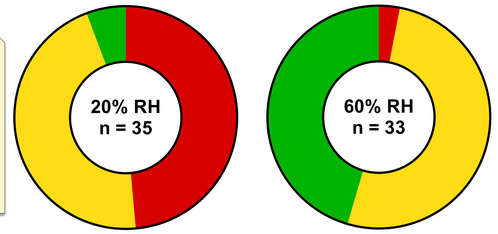

- **At 20% RH, ~94% were solids or semisolids.**
- **At 60% RH, ~97% were semisolids or liquids.**

Conclusion

These findings show a significant variability in SSA morphology and phase state with respect to a particular wind speed. Thus, the variability observed by the current findings suggests the importance of investigating the dynamic nature of SSA's morphology and phase state as a function of wind speed to accurately predict their climate-related effects.

Acknowledgments

Special thanks to Chamika K. Madawala, Alexei V. Tivanski, and everyone in the Tivanski group for the help on this project. Huge thanks also to the Department of Chemistry at the University of Iowa and the SSTP program for providing the opportunity to do this research.

References

1. Kaluarachchi, C. P., Or, V. W., Lan, Y., Madawala, C. K., Hasenecz, E. S., Crocker, D. E., Morris, C., Lee,H., Mayer, K. M., Sauer, J. D., Lee, C. S., Dorce, G., Malfatti, F., Stone, E. A., Cappa, C. D., Grassian, V. H., Prather, K. A., & Tivanski, A. V. (2021). Size-Dependent Morphology, Composition, Phase State, and Water Uptake of Nascent Submicrometer Sea Spray Aerosols during a Phytoplankton Bloom. *ACS Earth and Space Chemistry*, *6*(1), 116–130. https://doi.org/10.1021/acsearthspacechem.1c00306

2. Lee, H., Ray, K., & Tivanski, A. V. (2017). Solid, semisolid, and liquid phase states of individual submicrometer particles directly probed using atomic force microscopy. *Analytical Chemistry*, *89*(23), 12720–12726. https://doi.org/10.1021/acs.analchem.7b02755

3. Morris, H. S., Estillore, A. D., Laskina, O., Grassian, V. H., & Tivanski, A. V. (2016). Quantifying the Hygroscopic Growth of Individual Submicrometer Particles with Atomic Force Microscopy. *Analytical Chemistry*, *88*(7), 3647–3654. https://doi.org/10.1021/acs.analchem.5b04349

4. Madawala, C. K., Lee, H., Kaluarachchi, C. P., & Tivanski, A. V. (2021). Probing the water uptake and phase state of individual sucrose nanoparticles using atomic force microscopy. *ACS Earth and Space Chemistry*, *5*(10), 2612–2620. https://doi.org/10.1021/acsearthspacechem.1c00101

IOWA | Mengnan Sun
megansmn0829@gmail.com

Assessing Effects of a **Phthalate** on **Sperm Morphology** in a freshwater snail ecotoxicology model

Yiyi Tu[1], Nadia Patel[2], Bryan Guevara[3], Maurine Neiman[3]

[1]The Bishop's School, CA; [2]Cedar Falls High School, IA;

[3]Department of Biology, University of Iowa, IA

Do plastic additives affect reproduction?

- Phthalates are a series of endocrine-disrupting chemicals often found in plastics and common commodities (Wang & Qian 2021).
- This study analyzes the influence of DMP on reproduction in the New Zealand mud snail (*Potamopyrgus antipodarum*).
- We **hypothesize** that DMP will negatively affect male sperm, **predicting** that these sperm would have different and potentially abnormal phenotypes relative to unexposed males, and with these consequences increasing with DMP dose.

Quantifying Sperm Traits

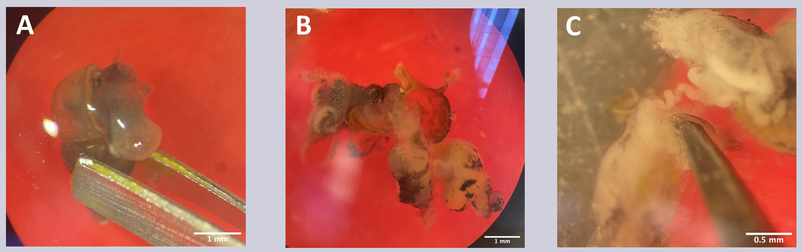

Fig 1. Dissection of *P. antipodarum* sperm duct under a dissecting microscope (Fig 1A and 1B at 30x; 1C at 40x). (A) Snail held with forceps. (B) Removed from shell. (C) Sperm duct.

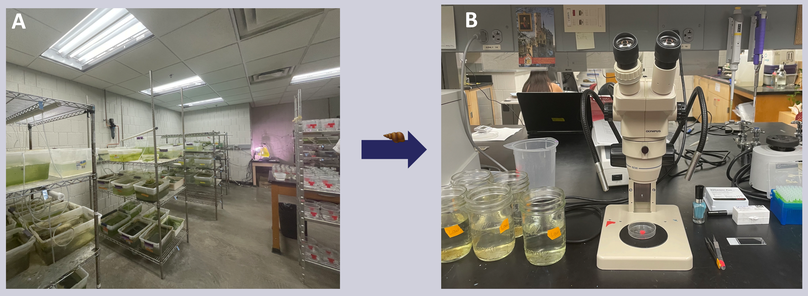

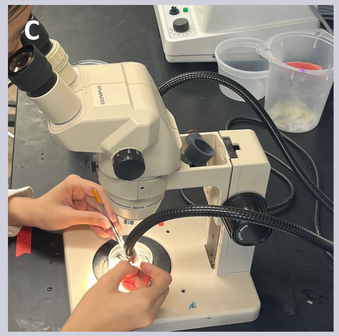

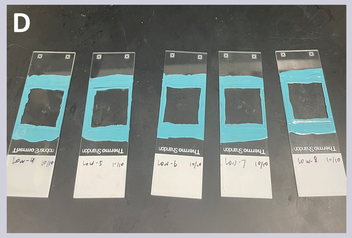

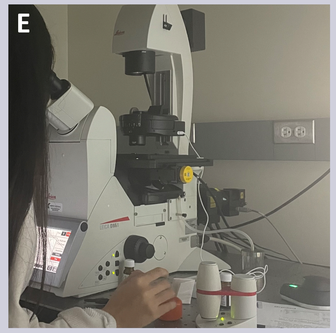

Fig 2. Experimental Process. (A) Snail room where snails were exposed to treatment for five weeks. (B) Dissecting microscope and equipment. (C) Dissection process. (D) Sealed slides containing sperm duct. (E) Looking at slides under LEICA DMi8 microscope in brightfield contrast.

How does a common phthalate affect sperm traits?

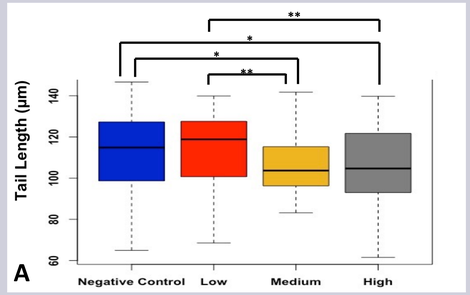

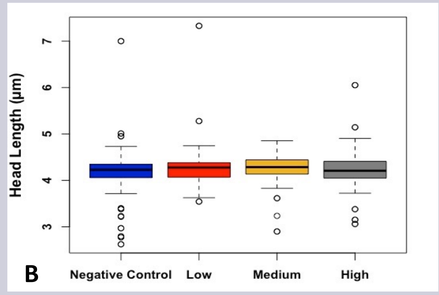

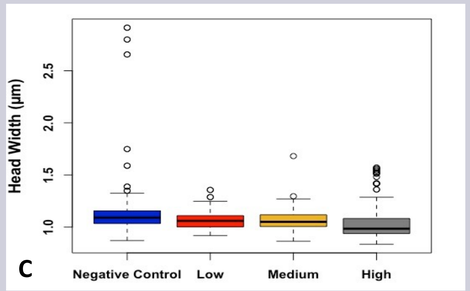

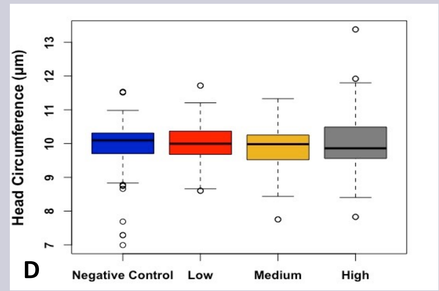

Fig 3. Boxplots displaying medians and variance from 10 sperm per slide across four treatment groups, Negative Control, Low (10^{-10} M), Med (10^{-8} M), High (10^{-6} M) (A) Tail length. (B) Head length. (C) Head circumference. (D) Head width. * = $p < 0.05$, ** = $p < 0.005$.

DMP Treatment	Tail Length (SD)	Head Length (SD)	Head Circumference (SD)	Head Width (SD)
Negative control	113.81 (16.21)	4.18 (0.57)	9.97 (0.73)	1.19 (0.38)
Low	114.51 (14.31)	4.27 (0.45)	10.01 (0.57)	1.07 (0.09)
Medium	107.58 (14.31)	4.27 (0.32)	9.91 (0.65)	1.07 (0.1)
High	108.47 (17.19)	4.24 (0.42)	10.08 (0.93)	1.06 (0.19)

Table 1. Means and standard deviation (SD) of sperm measurements.

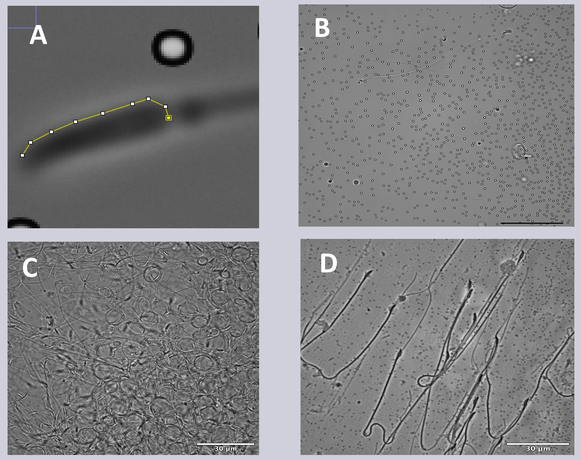

Fig 4. Images of sperm under LEICA DMi8 microscope. (A) Measuring the sperm in ImageJ. (B) Deformed sperm with oblong head. (C) Sperm duct. (D) Group of sperm.

- Sperm head length and head circumference did not differ across groups (Kruskal-Wallis, $p > 0.05$). Head width decreased as DMP concentration increased, suggesting DMP might decrease the amount of DNA in the sperm head, with potential for negative consequences.
- Sperm tail length decreased as the concentration of DMP increased, suggesting that DMP could decrease sperm motility.

Future Directions

- More sperm per snail are needed to adequately quantify abnormalities, which occur at fairly low (<<10%) frequency in normal sperm (Jalinsky et al. 2020).
- Increased DMP dosage might increase our ability to detect consequences in sperm.
- As *P. antipodarum* are a worldwide invasive species, a study comparing sperm in snails from different environments with different pollutant exposures could also be illuminating.

Acknowledgments & References

Special thanks to Bryan (the) G. and Dr. Neiman for their guidance and mentorship, the Neiman Lab for being amazing, Dr. Smolikove for allowing use of the LEICA microscope throughout this project, and the Belin-Blank center & SSTP program for this opportunity and funding.

Snail photo: Bart Zijlstra. Snail drawing: Assata Caldwell.

References: Schneider et al. 2012, Nature Methods, 9(7), 671–675. Jalinsky et al. 2020, Journal of Evolutionary Biology, 33(8), 1050–1059. R Core Team 2023, R Foundation for Statistical Computing, Vienna, Austria.

Understanding the SETDB1 Oncogenic Function in Endometrial Cancer

Jasmine Wang[1]; Kiarash Salari[2]; Shujie Yang, PhD[2]
[1]St. Andrew's Episcopal School, MD; [2]Department of Pathology, University of Iowa

I. Introduction

- **Endometrial cancer** (EC) is the most common gynecologic cancer.
- The incidence (66,200 new cases/year) and death (13,030 death/year) are on the rise.
- **SETDB1**, a histone methyltransferase which regulates gene silencing, is **overexpressed** in EC and **predicts worse survival**.
- Knock out SETDB1 in EC cells **slows down tumor growth** and prolongs survival in mice.
- SETDB1 promotes tumorigenesis by enhancing proliferation and immune evasion in EC.
- High expression of FLNA and CD47 predicts **worse survival** in EC patients and the high expression of ZNF266, ZNF841, and MT-CO1 predicts **favorable survival** in EC patients.

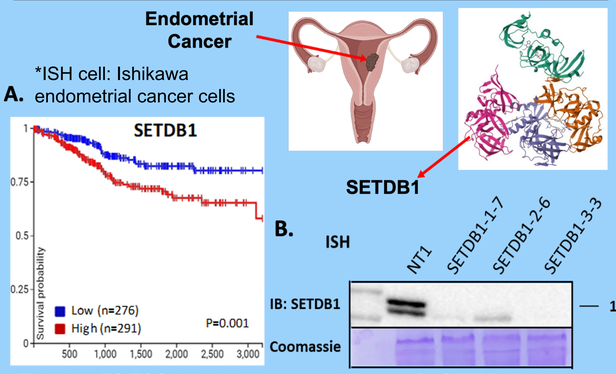

Fig 1. (A) EC-TCGA Kaplan Meyer survival curve for SETDB1 high and low expressing patients **(B)** SETDB1 immunoblot for NT1 and knockout clones in ISH*, Hec50 and ECC1 cancer cell lines

What are the mechanisms that SETDB1 promote tumorigenesis in EC?

II. Purpose and Hypothesis

- The purpose is to understand the **oncogenic function** of SETDB1 gene in EC.
- We hypothesize that SETDB1 can **promote oncogene expression** and **repress tumor suppressor gene expression** in EC.

III. Procedure

• RT q-PCR	• Western Blot	• CHIP assay
• Design primer using primer bank or IDT • Verify primer specificity using PCR • Run q-PCR to quantify mRNA expression	• Collect cells from cell plates • Extract protein from cells • Run Western blot to check protein expression	• Find SETDB1 binding peak on the target gene • Design gDNA primer • CHIP assay • Run PCR and q-PCR to verify the binding

IV. Method

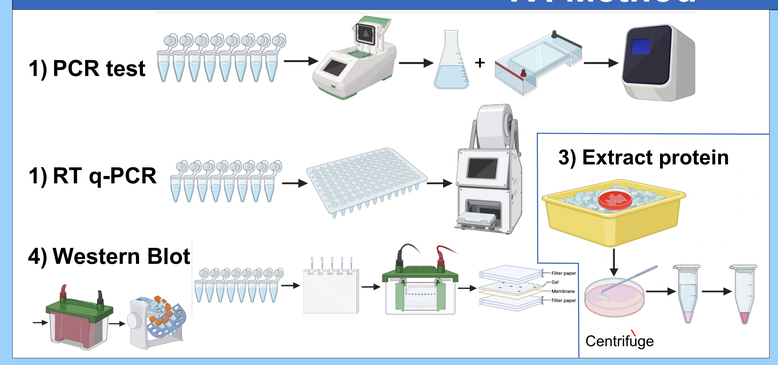

Venessa Camp, Kiarash Salari et al., 2021, AJCR, Review

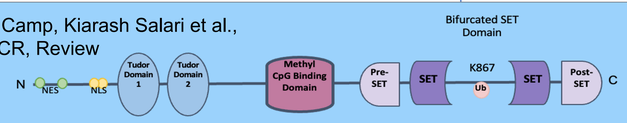

SETDB1 Structure

1) PCR: Use PCR machine and Agarose gel
2) RT q-PCR: use q-PCR machine (2 hrs)
3) Extract protein:
- **a) Dump medium and wash with washing buffer twice and add 1ml of it**
- **b) Scrape cells off and centrifuge**
- **c) Dump supernatant and extract proteins from the pellet**

4) Western blot
- **a) Run samples on the gel for 1hr**
- **b) Transfer protein from the gel to membrane using tank blotting transfer system**
- **c) Probe the membrane with 1st and 2nd antibody for 2hrs**

V. Results and Data

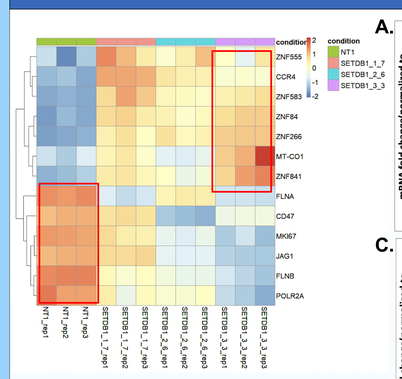

Fig 2. Cluster Heat map of SETDB1 and regulated genes

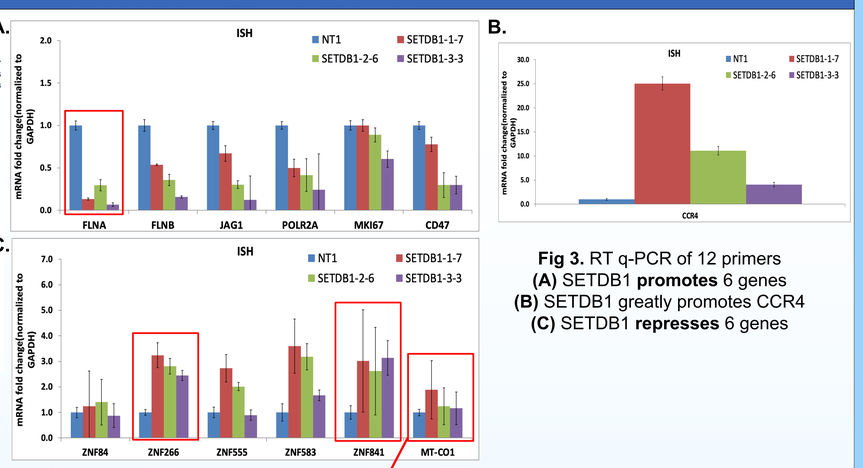

Fig 3. RT q-PCR of 12 primers
(A) SETDB1 **promotes** 6 genes
(B) SETDB1 greatly promotes CCR4
(C) SETDB1 **represses** 6 genes

- POLR2A, FLNB, MKI67, CD47: **high expression** in NT1 cells, but **Low** in SETDB1 knockout.
- ZNF841, MT-CO1, ZNF266, ZNF84, ZNF583, CCR4, ZNF555: **low expression** in NT1 cells, but **high** in SETDB1 knockout.

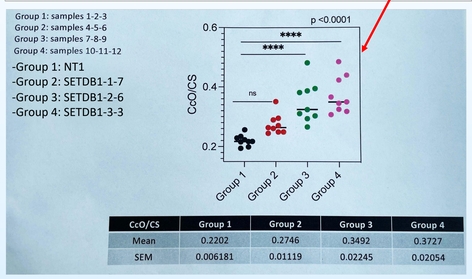

CcO/CS	Group 1	Group 2	Group 3	Group 4
Mean	0.2202	0.2746	0.3492	0.3727
SEM	0.006181	0.01119	0.02245	0.02054

*CcO, cytochrome C oxidase
CS, citrate synthase

- Downregulate SETDB1 can increase **MT-CO1 mRNA expression** and increase **mitochondria super complex IV activity.**

Fig 4. Activity test for MT-CO1 in NT1 and SETDB1 knockout

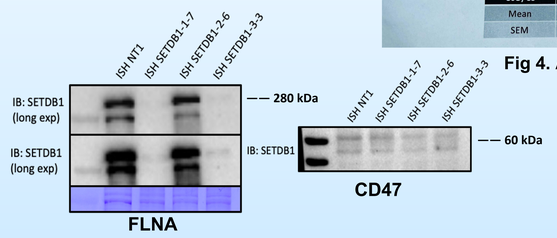

Fig 5. Detection of protein expression of FLNA and CD47 in knockout cell and wild type cell by Western blot

- FLNA has nearly **no expression** in SETDB1-1-7, 3-3 KO.
- CD47 expression is slightly **decreasing**.

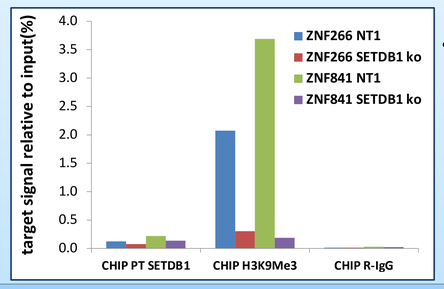

- Knockout SETDB1 **reduces binding** of SETDB1 and H3K9me3 on ZNF266 and ZNF841.

Fig 6. CHIP q-PCR of ZNF266 and ZNF841

VI. Conclusion

- Knockout SETDB1 greatly **decreases** POLR2A, FLNA, and **increases** ZNF266, ZNF841 and MT-CO1.
- Depletion of SETDB1 **decreases** FLNA and CD47 expression at protein level.
- Depletion of SETDB1 **enhances** Mitochondria super complex IV activity.
- SETDB1 **directly binds on the promoter regions of ZNF266 and ZNF841**, thus repressing their expressions through H3K9 trimethylation.

VII. Discussion

- Understand **how SETDB1 regulates** POLR2A, MT-CO1, and SETDB1 itself.
- For those genes that SETDB1 promotes, how SETDB1 promotes them in EC.
  - Does SETDB1 **trigger a chain of event** that activate some other genes, thus resulting in promoting those genes?
  - Does SETDB1 **itself** activate them?
- After we testified binding ability in ISH cell, can we generalize to **all the cell lines**?
- Test the function of downstream genes through either overexpressing or knocking down the genes.
  - Investigating the functional implication of the gene in tumor growth.

VII. Acknowledgement

The project was supported by NIH R37-CA238274(SY), the Department of Pathology Start-Up Fund(SY) and Belin-Blank Center SSTP.

IX. Reference

- American Cancer Society. (2023). *Cancer Facts & Figures 2023*. American Cancer Society.
- Frietze, S., O'Geen, H., Blahnik, K. R., Jin, V. X., & Farnham, P. J. (2010). ZNF274 recruits the histone methyltransferase SETDB1 to the 3' ends of ZNF genes. *PloS one*, *5*(12), e15082. https://doi.org/10.1371/journal.pone.0015082
- Griffin, G. K., et al., (2021). Epigenetic silencing by SETDB1 suppresses tumour intrinsic immunogenicity. *Nature*, *595*(7866), 309–314. https://doi.org/10.1038/s41586-021-03520-4
- Johnson, E., Salari, K., & Yang, S. (2023). SETDB1: A perspective into immune cell function and cancer immunotherapy. *Immunology*, *169*(1), 3–12. https://doi.org/10.1111/imm.13619
- Lazaro-Camp, V. J., Salari, K., Meng, X., & Yang, S. (2021). SETDB1 in cancer: overexpression and its therapeutic implications. *American journal of cancer research*, *11*(5), 1803–1827.

3D-Printed Silk Scaffolds for an In Vitro Lung-on-a-Chip Model

Maximilian Wang[1], Reza Amouzandeh[2], M.S., Xuan Mu[2], PhD.

[1]Isaac M. Bear High School; [2]Roy J. Carver Department of Biomedical Engineering, University of Iowa

IOWA

Roy J. Carver Department of Biomedical Engineering

PROBLEM ADDRESSED

- Drug discovery research involves the use of various models to predict drug effects in humans.
- Traditional 2D (i.e. Petri dish), 3D (i.e. hydrogel scaffold), and in vivo (animal) models have often proven to be oversimplified, expensive, and/or irrelevant.
- Such drawbacks have slowed research and resulted in higher drug prices (Caddeo et al., 2017).
- This could be addressed by a tissue model that can accurately, conveniently, and repeatably model human organs and organ systems.

PROJECT OBJECTIVES

- One recent concept to replace traditional models, the organ-on-a-chip (OoC), aims to replicate tissues via a careful combination of biocompatible scaffolds, microfluidic channels to maintain a flow of culture media, and physiologically relevant mechanical factors (Huh et al., 2012).
- This concept has been expanded with recent advancements in 3D printing, which enables customizable, efficient, and high-throughput manufacturing of monolithic proteinaceous scaffold materials (Mu et al., 2021).
- This study aims to evaluate lung cell growth on silk-based 3D printed membranes processed with different bioinspired solvents. Via optical density imaging to determine transparency and confocal microscopy to determine cell proliferation, we explore various salt ion effects on the ability of monolithic silk substrates to support lung alveoli cells in a lung-on-a-chip model.

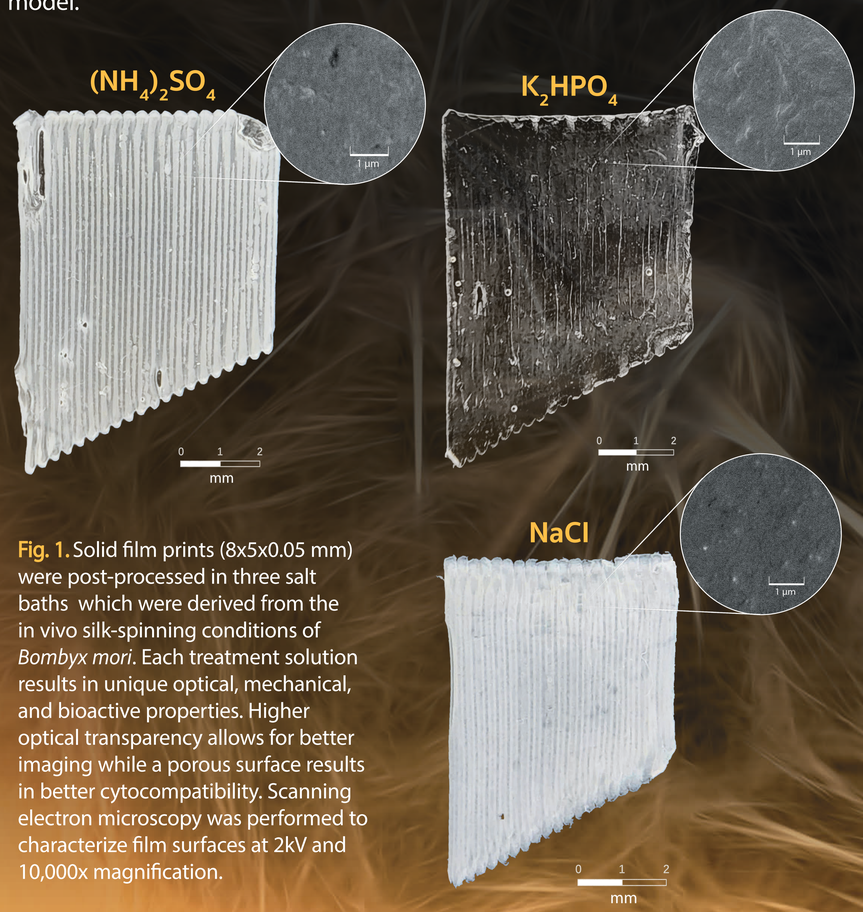

Fig. 1. Solid film prints (8x5x0.05 mm) were post-processed in three salt baths which were derived from the in vivo silk-spinning conditions of *Bombyx mori*. Each treatment solution results in unique optical, mechanical, and bioactive properties. Higher optical transparency allows for better imaging while a porous surface results in better cytocompatibility. Scanning electron microscopy was performed to characterize film surfaces at 2kV and 10,000x magnification.

We explored salt ion effects for manufacturing silk substrates to support lung alveoli cells in a 3D lung-on-a-chip model.

EXPERIMENTAL DESIGN

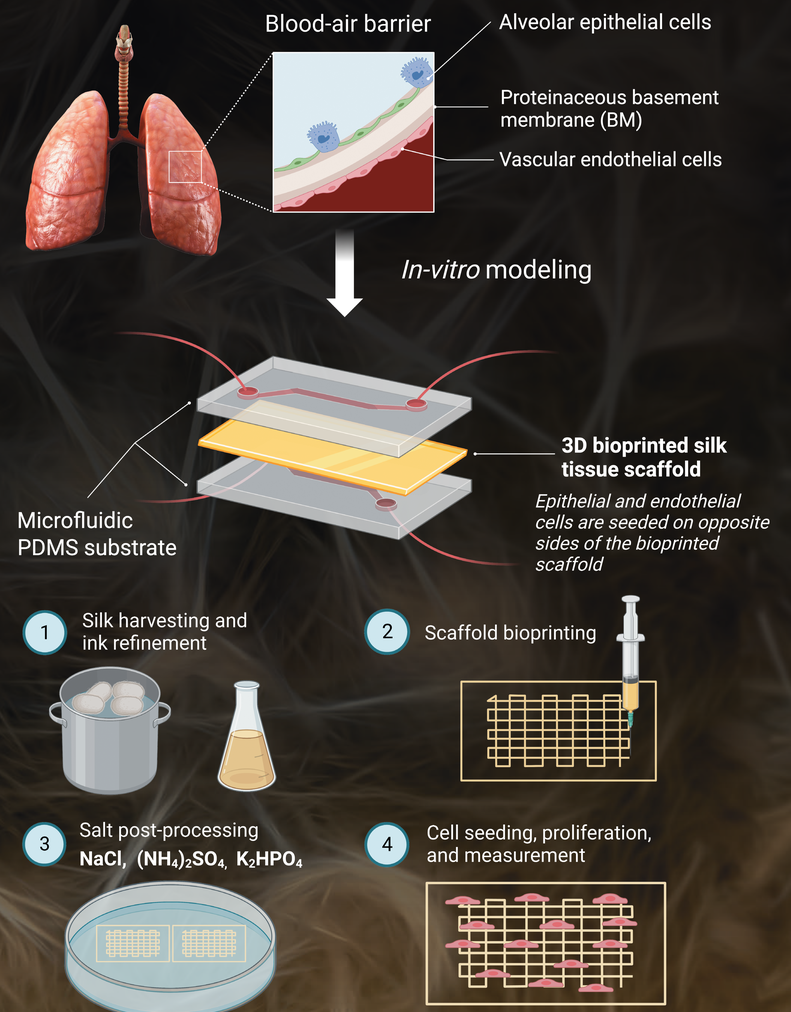

Fig. 2. Experimental design was guided by the testing of three post-processing salt baths; NaCl, $(NH_4)_2SO_4$, and K_2HPO_4. 1. Silk was harvested and boiled in 20 mM $NaCO_3$, dissolved in LiBr, and dialyzed and concentrated. 2. Solid films were printed on a CELLINK Inkredible printer. 3. Prints were processed in various salt baths. 4. Mammalian lung cells were seeded on top of the prints and growth was measured via cell immunostaining and confocal microscopy after incubation at physiological conditions.

RESULTS

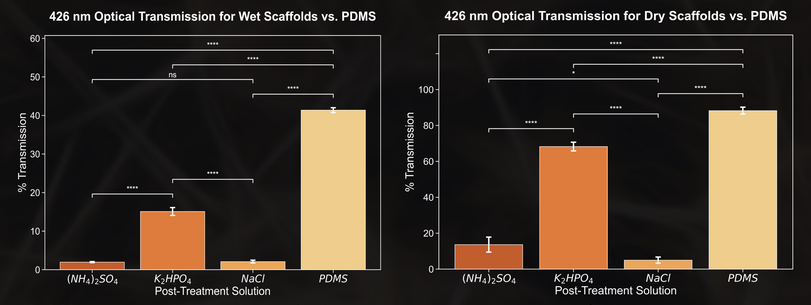

Fig. 3. Mean percent optical transmittance of various post-processing methods on **wet** and **dry** silk substrates as compared to PDMS. ns: $p \leq 1.00$, *: $0.01 < p \leq 0.05$, **: $0.001 < p \leq 0.01$, ***: $0.0001 < p \leq 0.001$, ****: $p \leq 0.0001$. p-values were calculated via a two-sample t-test assuming unequal variance.

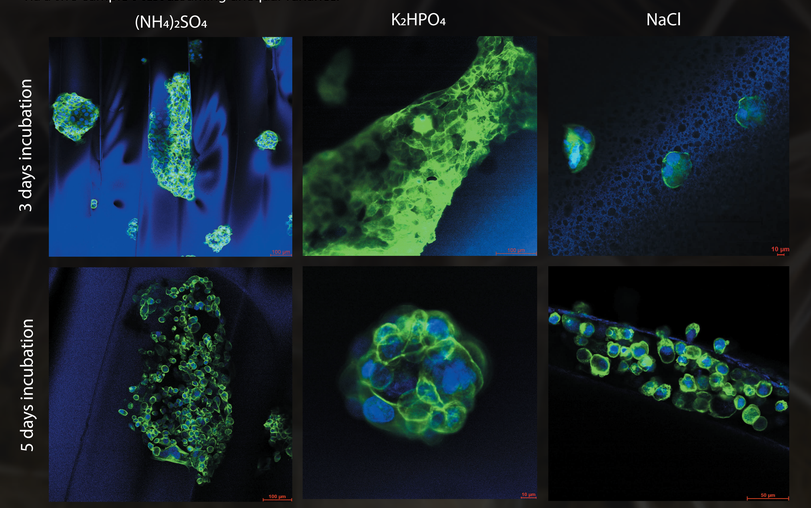

Fig. 4. Confocal microscopy of HCI-N441 cancerous lung cells immunostained with DAPI (405 nm, shown in blue) and phalloidin (488 nm, shown in green), which indicate cell nuclei and cytoskeletons, respectively. Silk background autoflouresces (seen as blue) due to certain amino acids present in the silk fibroin protein.

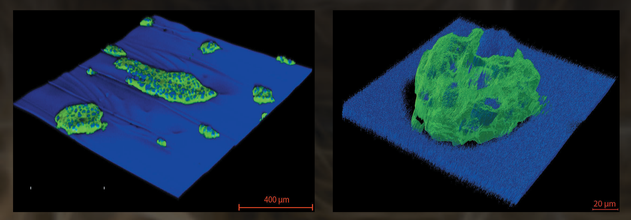

Fig. 5. Left-to-right: 3D Z-stack reconstructions of cellular aggregates on $(NH_4)_2SO_4$ and K_2HPO_4 after 3 days and 5 days of incubation, respectively. Large aggregates were observed as opposed to the expected cellular monolayer, likely due to procedural difficulties.

CONCLUSION & DISCUSSION

- $(NH_4)_2SO_4$ scaffolds featured high cytocompatibility with a larger observed cell population and larger aggregates after five days of incubation.
- K_2HPO_4 scaffolds featured high optical transparency, comparable with the PDMS control, for convenient imaging.
- NaCl scaffolds featured the least observed cell population, but have previously demonstrated superior mechanical performance via higher structural beta-sheet concentration, which may be relevant for stresses exerted by integration into a lung-on-a-chip (Mu et al., 2023).
- Overall, monolithic silk scaffolds demonstrate high potential for a highly customizable and biocompatible substrate for lung-on-a-chip models
- Future work includes investigation of the exact nature of special ion effects on silk protein molecular assembly, as well as optimization to produce the most biocompatible and experimentally viable scaffolds.

REFERENCES

Caddeo, S., Boffito, M., & Sartori, S. (2017). Tissue engineering approaches in the design of healthy and pathological in vitro tissue models. *Frontiers in Bioengineering and Biotechnology*, *5*. https://doi.org/10.3389/fbioe.2017.00040

Huh, D., Leslie, D. B., Matthews, B. F., Fraser, J. S., Jurek, S., Hamilton, G. A., Thorneloe, K. S., McAlexander, M. A., & Ingber, D. E. (2012). A human disease model of drug toxicity–induced pulmonary edema in a lung-on-a-chip microdevice. *Science Translational Medicine*, *4*(159). https://doi.org/10.1126/scitranslmed.3004249

Mu, X., Agostinacchio, F., Xiang, N., Pei, Y., Khan, Y., Guo, C., Cebe, P., Motta, A., & Kaplan, D. L. (2021). Recent advances in 3D printing with protein-based inks. *Progress in Polymer Science*, *115*, 101375. https://doi.org/10.1016/j.progpolymsci.2021.101375

Mu, X., Amouzandeh, R., Vogts, H., Luallen, E., Arzani, M. Biofabrication with silks using special ion effects (2023). University of Iowa.

ACKNOWLEDGEMENTS

Many thanks to Dr. Xuan Mu, Mr. Reza Seyed Amouzandeh, Mr. Milad Arzani, and Ms. Hannah Vogts for supporting my learning and research. I also could not have done this project without Mr. Jacob Olsen, Mr. Reynold Tawiah-Quashie, and the rest of the SSTP and Belin-Blank staff.

Effect of Early Life Stress on Microglia in the Prefrontal Cortex of Mice

Gloria Wu, Sara B. Mitchell[1, 2], Rainbo Hultman, PhD[1, 2], Hanna E. Stevens, PhD[1]

[1]Department of Molecular Physiology and Biophysics, University of Iowa; [2]Department of Psychiatry, University of Iowa

Background

- Microglia are the brain's resident immune cells. [1]
- Microglia are impacted by early life stress (ELS).[2]
  - Microglia are lastingly impacted in the human brain after childhood abuse and could lead to increased vulnerability to psychiatric disorders.
- The prefrontal cortex (PFC) is one of the last structures to develop, making it more vulnerable to the effects of ELS. [3]
- Maternal separation leads to a decrease in microglia in the infralimbic PFC (IL) compared to the prelimbic PFC (PL) in male mice. [4]
- Women are more susceptible to the effects of ELS. [5]

Hypothesis: ELS causes a decrease in microglia density and soma size in the PFC of adolescent female mice.

Methods

- Brain tissue of 11 adolescent (P30) female mice were immunostained for Iba1, a marker for microglia.
  - Control group (N=5), ELS group (N=6)

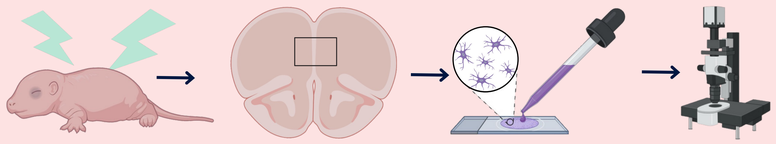

- Slides were cover-slipped with VECTASHIELD with DAPI to visualize cell count.
- Pictures were taken using a fluorescent microscope.
  - Three sections containing the PFC per brain (35 µm sections).
  - Four fields per section (two per hemisphere); two in the PL, two in the IL.
  - Two focal planes per image field.
  - One Iba1 + one DAPI picture per focal plane.
- Microglia density per field and soma sizes were recorded using ImageJ's measurement tool.
- GraphPad Prism was utilized for statistical analysis.

Results

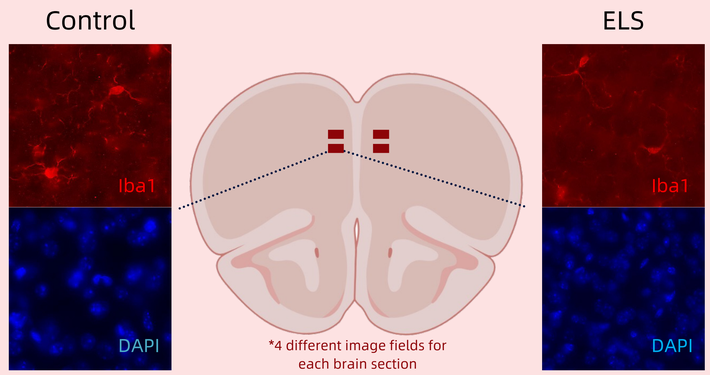

Microglia Density

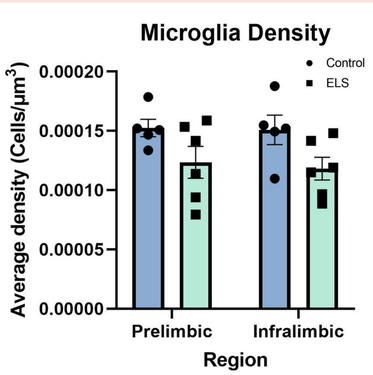

Figure 1. Average microglia density per sample

There is a trending decrease (p=.06) in microglia density in the PFC between the control group (M=.00015) and ELS group (M=.00012), but no significant difference between the PL and IL.

Soma Size

There is no statistically significant difference between the soma sizes of microglia in the control group (M=725.5) and ELS group (M=716).

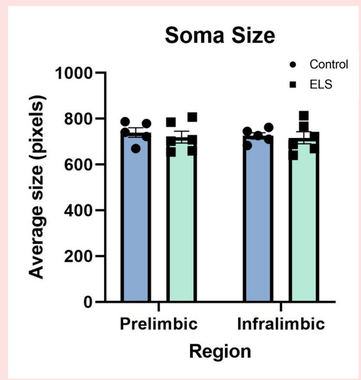

Figure 2. Average soma size per sample

Conclusions

- **ELS causes a trending decrease in microglia density in the PFC of adolescent female mice** but no significant difference in soma size.
- ELS does not seem to have a differing impact on microglia density or size in the PL vs. the IL.
- A decrease in microglia density could potentially impact their ability to form and wire neuronal circuits, however more research is needed.

Future Directions

- Differences in microglia morphology.
- Sex differences in microglia density, size, and morphology.
  - A previous study has shown that ELS causes an increase in microglia density in the PFC of adolescent male mice.[6]
- Long-term impact of ELS on microglia.
- Impact of ELS on microglia in different regions of the brain.
- Impact of ELS on the density of different brain cells.

Acknowledgements

Special thanks to the Hultman Lab, Stevens Lab, and especially my mentor, Sara Mitchell, for their continued support throughout the course of this project. I would also like to thank SSTP and the Belin-Blank Center for this opportunity.

Design created via Canva.
Graphics generated via BioRender and Canva.
Graph generated via GraphPad Prism.

References

1. Milbocker, K. A., Campbell, T. S., Collins, N., Kim, S., Smith, I. F., Roth, T. L., & Klintsova, A. Y. (2021). Glia-driven brain circuit refinement is altered by early-life adversity: Behavioral outcomes. Frontiers in Behavioral Neuroscience, 15. https://www.frontiersin.org/articles/10.3389/fnbeh.2021.786234/full
2. Vecchiarelli, H. A. & Simoncicova, E. (2021). Microglial involvement with psychiatric diseases. Psychiatric Times, 38(1). https://www.psychiatrictimes.com/view/microglial-involvement-psychiatric-diseases
3. Reemst, K., Kracht, L., Kotah, J. M., Rahimian, R., van Irsen, A. A. S., Sotomayor, G. C., Verboon, L. M., Brouwer, N., Simard, S., Turecki, G., Mechawar, N., Kooistra, S. M., Eggen, B. J. L., & Korosi, A. (2022). Early-life stress lastingly impacts microglial transcriptome and function under basal and immune-challenged conditions. Translational Psychiatry, 12. https://doi.org/10.1038/s41398-022-02265-6
4. Gildawie, K. R., Orso, R., Peterzell, S., Thompson, V., & Brenhouse, H. C. (2021). Sex differences in prefrontal cortex microglia morphology: Impact of a two-hit model of adversity throughout development. Neuroscience Letters, 738. https://doi.org/10.1016/j.neulet.2020.135381
5. Goodwill, H. L., Manzano-Nieves, G., Gallo, M., Lee H., Oyerinde, E., Serre, T., & Bath, K. G. (2019). Early life stress leads to sex differences in development of depressive-like outcomes in a mouse model. Neuropsychopharmacology 44(4), 711-720. https://doi.org/10.1038/s41386-018-0195-5
6. Usui, N., Ono, Y., Aramaki, R., Berto, S., Konopka, G., Matsuzaki, H., & Shimada, S. (2021). Early life stress alters gene expression and cytoarchitecture in the prefrontal cortex leading to social impairment and increased anxiety. Frontiers in Behavioral Neuroscience, 12. https://www.frontiersin.org/articles/10.3389/fgene.2021.754198/full

Exploring Vocal Acoustic Features as a Marker for Depression and Anxiety Status with TMS Treatment

[A] Kent School, CT
[B] Department of Communication Sciences and Disorders
[C] Iowa Neuroscience Institute
[D] University of Iowa Department of Psychiatry

Dora Xiang[a], Lucas Casten[b], Ethan Bahl[b], Annie Gleason[b], Jacob J. Michaelson (PhD)[b,c,d]

Background:

- Approximately 280 million people around the globe struggles with depressive disorder, and approximately **8.4% of the US population** are suffer from **Major Depressive Disorder** (MDD) in 2020. Those numbers continue to increase. (World Health Organization, 2020)
- Of those with depression, **almost one-third** are simultaneously **treatment-resistant** (World Health Organization, 2020)
- **Anxiety disorders dominates ~20% of the US.** (Lépine et al., 2002)
- **TMS (transcranial magnetic stimulation)** helps improve treatment-resistant depression by using series of magnetic pulses to stimulate nerves in the areas associated with depression. Thus, altering depression via brain wave stimulation. (UC San Diego Health)

- TMS can help anxiety by activating brain cells regulating mood. (UC San Diego Health)
- **Vocal features** can act as markers for one's depression because they are difficult to hide; jitter and shimmer score have abnormalities in those with depression. (Weintraub et al., 2023)
- Previous studies show that pitch and volume decreases with one's depression scores, (Weintraub et al., 2023) while their hoarseness increases (Jia et al., 2019).

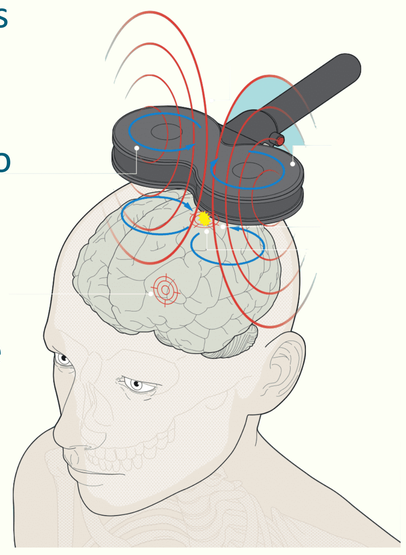

Objective:

- Identify vocal biomarkers of depression and anxiety in a sample undergoing TMS treatment for MDD or other severities of depression.

Research Question:

- **How significant of a correlation does acoustics have with one's depression and anxiety status before and after TMS treatment?**
- Can vocal acoustics (e.g., loudness) predict depression and anxiety scores?
- Can these features predict who will respond best to TMS treatment?

Methods:

- Speech samples from 20 patients with either MDD or other forms of depressive disorders were collected in the University of Iowa Clinic
- Quantitative measurements of depression and anxiety were collected weekly from the PHQ 9 (Patient Health Questionnaire) and GAD 7 (Generalized Anxiety Disorder Assessment) scores.
- Weekly speech samples were extracted from each patient during every TMS treatment..
- Acoustic features such as jitter scores, shimmer scores, mean pitch, HNR (Harmonic to Noise Ratio), standard deviation of pitch, and loudness were extracted using Surfboard, a Python tool. and their difference scores were calculated.
- Correlation tests (T.Tests, R correlation tests, p values) were used to compute levels of association between acoustic features and PHQ 9 and GAD 7 scores in the R script.

PHQ 9 and GAD 7 Score Comparison:

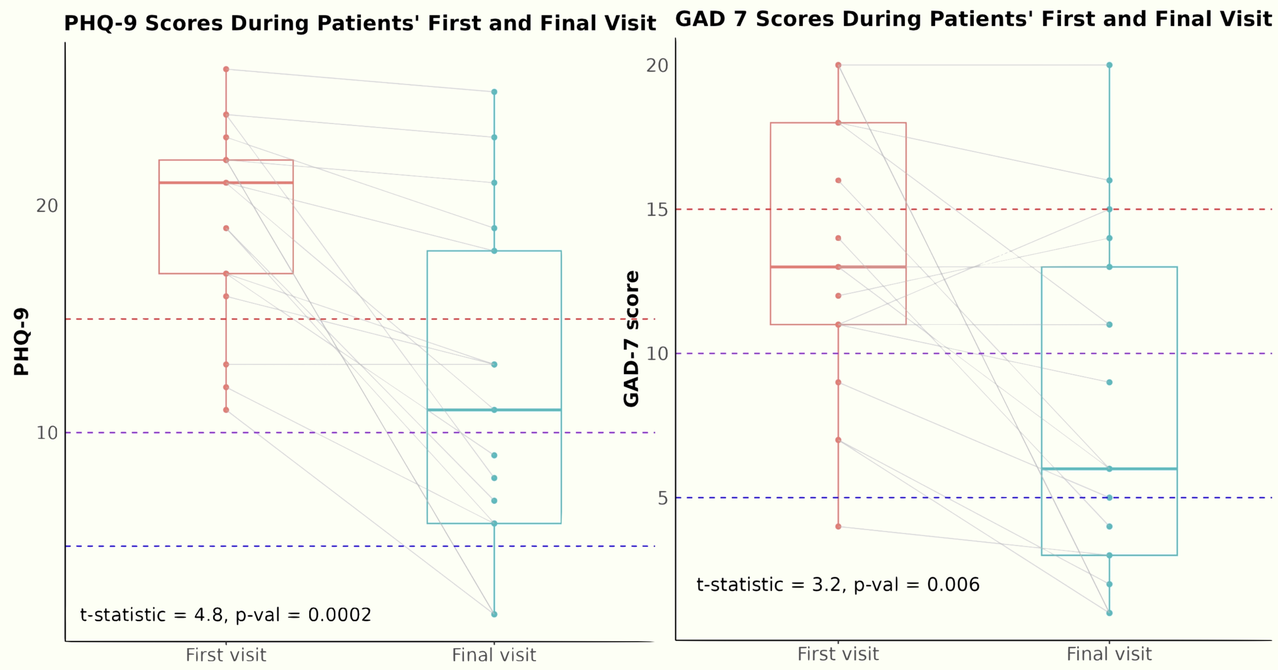

- Note: Patients with mild to moderate anxiety/depression had a much more significant improvement in scores as compared to those on the severe end of the spectrum

Mental Health Scores and Acoustic Scores Correlation:

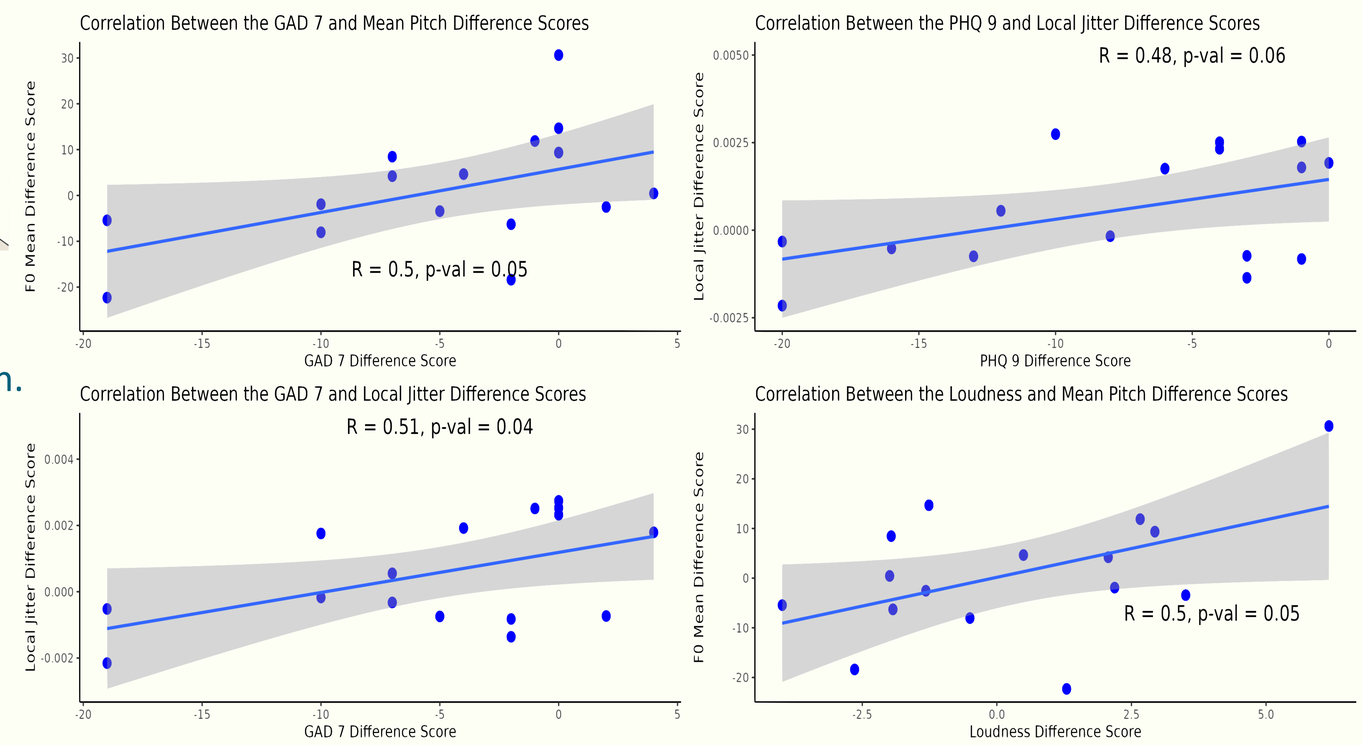

- GAD 7 scores had a much more significant correlation to acoustic features as opposed to PHQ 9 Scores
- Jitter and F0 mean pitch scores had a much more significant correlation to GAD 7 and PHQ 9 scores than shimmer, HNR, or F0 standard deviation scores.

Acoustic Features Predictive of Treatment Response:

Dependent Variable	Independent Variable	Beta Estimate	P Value	R^2
GAD 7 Response Score	Loudness Before Treatment	-1.1	<0.01	37%
PHQ 9 Response Score	Loudness Before Treatment	-0.45	0.346	6%

Conclusion:

- TMS is an effective treatment for depression and anxiety.
- Anxiety is significantly correlated with vocal acoustics.
- Vocal acoustics can predict TMS treatment response
- This study has some limitations including a small sample size, no placebo treatment, and treatment duration inconsistency.
- Future directions for this study would be to see if vocal acoustics in treatment responses have correlations with other psychiatric disorders, and to identify variables associated with non-responsive TMS patients.

References

1. Lépine, J. P. (2002). The epidemiology of anxiety disorders: prevalence and societal costs. *Journal of Clinical Psychiatry*, *63*, 4-8.
2. Jia, Y., Liang, Y., & Zhu, T. (2019, October). An analysis of voice quality of Chinese patients with depression. In *2019 22nd Conference of the Oriental COCOSDA International Committee for the Co-ordination and Standardisation of Speech Databases and Assessment Techniques (O-COCOSDA)* (pp. 1-6). IEEE.
3. *Transcranial magnetic stimulation (TMS) to treat symptoms of depression*. Transcranial Magnetic Stimulation (TMS) to Treat Symptoms of Depression: Americas TMS Center: TMS Specialists. (n.d.)https://www.americastms.com/blog/transcranial-magnetic-stimulation-tms-to-treat-symptoms-of-depression
4. *Transcranial magnetic stimulation (TMS)*. UC San Diego Health. (n.d.). https://health.ucsd.edu/care/behavioral-mental-health/depression-treatment/tms/#:~:text=What%20Is%20Transcranial%20Magnetic%20Stimulation,be%20associated%20with%20major%20depression
5. Weintraub MJ, Posta F, Ichinose MC, Arevian AC, Miklowitz DJ. Word usage in spontaneous speech as a predictor of depressive symptoms among youth at high risk for mood disorders. J Affect Disord. 2023 Feb 15;323: pp.675-678. doi: 10.1016/j.jad.2022.12.047. Epub 2022 Dec 14. PMID: 36528134; PMCID: PMC9848879.
6. World Health Organization. (2023a, March 31). *Depressive disorder (depression)*. World Health Organization. https://www.who.int/news-room/fact-sheets/detail/depression

Acknowledgements

We are grateful to all of the individuals who participated in this study. Thank you to Aaron Bose MD, PHD and Nick Trapp MD for administering the TMS treatment to the patients. Importantly, special thanks to everyone in the Michaelson lab for mentoring me and the Belin Blank center for providing me with this research opportunity.

Contact

michaelson.lab.uiowa.edu
jacob-michaelson@uiowa.edu

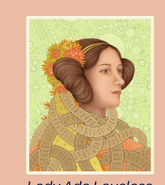

Lady Ada Lovelace

Physical and Computational Analysis of Metal Complexes to Better Understand Metal-Ligand Bonding

Alan Xu[1], Dhruba R Paudel[2], Aditi Bhattacherjee, Ph.D.[2]

The University of Iowa

Background and Objectives

A coordination complex is a chemical compound that consists of a central atom, often a metal, and various surrounding molecules known as ligands. Metal-ligand bonding is an interesting topic in that there are very many unique ways in which a ligand can bond to a metal in a complex.

A cyclopentadienyl anion (C5H5- or commonly Cp-), is a common organic ligand. Cp- can bond to a large set of different metals to form interesting coordination complexes with various unique properties.

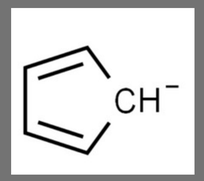

Metal-ligand bonding is an especially interesting topic considering the way Metal-ligand interactions can occur on a spectrum of covalence. Not only that, these interactions mirror acid-base reactions concerning electron donation during bonding. Ligands can also coordinate through multiple contiguous atoms. Almost all complexes with cyclopentadienyl have a hapticity of 5, meaning all five carbons in the cyclopentadienyl ring are bound to the metal ion.

The overall objective boils down to a single question:

How exactly do metal-ligand bonds work between cyclopentadienyl and metal ions

This question involve many smaller questions as well:

How exactly are electrons shared in these bonds? Are there any differences between this any other bonds at hapticity one? How does electron-sharing work in higher hapticities?

Methodology

Complex molecules are first modeled with Gaussview, where bond distances and energies are left ambiguous

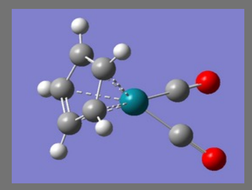

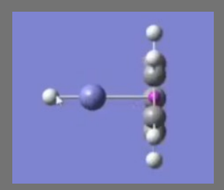

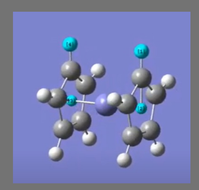

The files are then packaged into data files, and computer calculations are run to find exact bond energies, bond lengths, and to correct atomic positions.

Then, UV-vis spectroscopy is run on the substance while considering expected results

Results

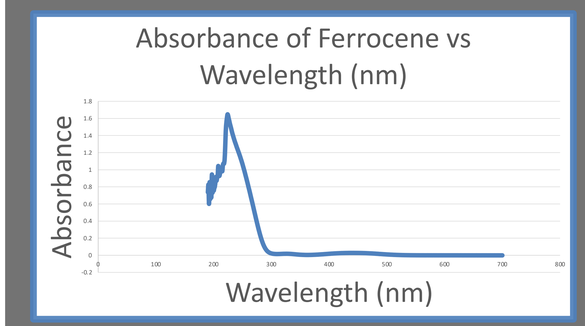

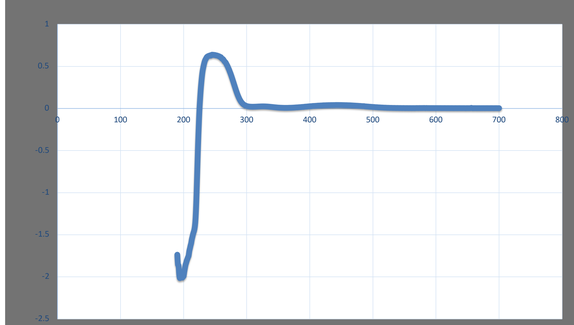

Mulliken charges:

		1
1	Fe	0.845350
2	C	-0.312803
3	H	0.228876
4	C	-0.313154
5	C	-0.313154
6	H	0.228824
7	C	-0.313901
8	H	0.228824
9	C	-0.313901
10	H	0.228856
11	H	0.228856
12	C	-0.312803
13	H	0.228876
14	C	-0.313154
15	C	-0.313154
16	H	0.228824
17	C	-0.313901
18	H	0.228824
19	C	-0.313901
20	H	0.228856
21	H	0.228856

Implications

Most of these results simply confirm what we already knew or suspected:

Shared equal charges among carbons in cyclopentadienyl complexes (with a hapticity of five)

Expected ultraviolet absorbance at around 200 nm along with expected absorbance at around 400 nm

Ultimately, these results help set up deeper research involving more advanced research techniques.

Conclusion

Although the results were not necessarily interesting, they set us up for further research into these molecules, and potential to find interesting interactions with different wavelengths of light

Acknowledgements and References

Jay, R. M., Banerjee, A., Leitner, T., Wang, R.-P., Harich, J., Stefanuik, R., Wikmark, H., Coates, M. R., Beale, E. V., Kabanova, V., Kahraman, A., Wach, A., Ozerov, D., Arrell, C., Johnson, P. J., Borca, C. N., Cirelli, C., Bacellar, C., Milne, C., … Wernet, P. (2023). Tracking C–H activation with Orbital Resolution. *Science*, *380*(6648), 955–960. https://doi.org/10.1126/science.adf8042

Hashikawa, Y., & Murata, Y. (2021). Synthesis and oligomerization of cpm(co)2. *ACS Omega*, *6*(49), 34137–34141. https://doi.org/10.1021/acsomega.1c05739

Godin, R., Wang, Y., Zwijnenburg, M. A., Tang, J., & Durrant, J. R. (2017). Time-resolved spectroscopic investigation of charge trapping in carbon nitrides photocatalysts for hydrogen generation. *Journal of the American Chemical Society*, *139*(14), 5216–5224. https://doi.org/10.1021/jacs.7b01547

Thank you to the Aditi Bhatacherjee, Dhruba R. Paudel, Caleb H. DeWittt, Belin-Blank Center, and the University of Iowa

Identifying Brain Networks Critical for Working Memory

Ethan Yang[1,2], Mark Bowren[1], Daniel Tranel[1,2]

[1]Department of Neurology, University of Iowa Carver College of Medicine; [2]Department of Psychological and Brain Sciences, University of Iowa Carver College of Medicine

Introduction

Working memory is a brain system that provides temporary storage and manipulation of information necessary for such complex cognitive tasks such as language comprehension, learning, and reasoning (Baddeley, 1992)

- Comprised of three parts
    - Central Executive – main processing unit
    - Phonological Loop – temporary storage of auditory information
    - Visuospatial Sketch Pad – temporary storage of visual and spatial information

Working memory can be measured in many ways including neuropsychological tests such as the digit span

- Digit span includes three parts
    - Forwards – patients repeat digits given in the same order
    - Backwards – patients repeat digits given in backwards order
    - Sequencing – patients repeat digits given in ascending

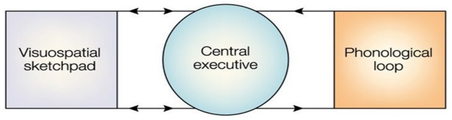

Nature Reviews | Neuroscience

Purpose and Hypothesis

We aimed to determine specific regions of the brain that influence working memory. We predicted the lateral prefrontal cortex in the left hemisphere to have the most influence due to previous research indicating its importance in the processing of words (Pisoni et al., 2019). The lateral prefrontal cortex has also been shown to house the central executive which is the impaired system in this experiment

Methods

- Identified patients with lesions and working memory impairment
    - LDSF - LDSB ≥ 3
- Created heat maps which layered lesions of patients to help identify areas of concentration
- Generated T-tests comparing lesion location, specifically in the superior longitudinal fasciculus and the rest of the brain

Results

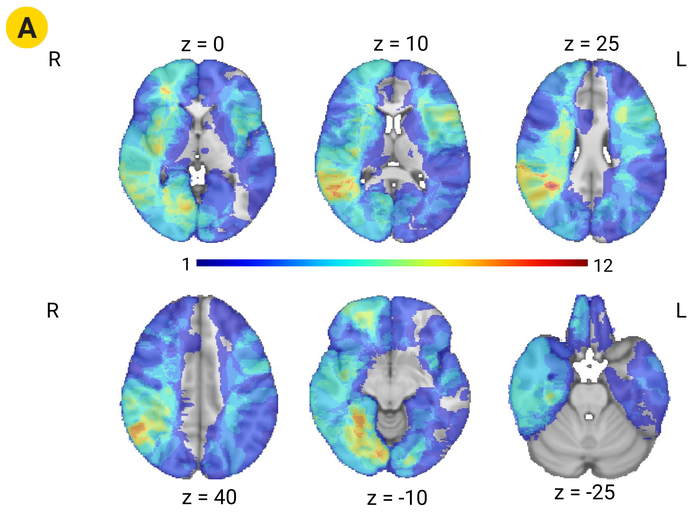

Figure A: 2D Heat maps of patients in different locations. Warmer colors represent higher lesion overlap

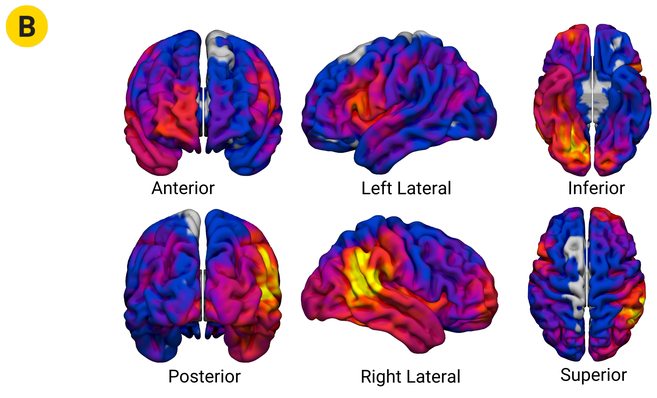

Figure B: 3D heat maps of patients. Warmer colors represent higher lesion overlap

C

Figure C: T-test comparing patients with SLF damage to those without

Conclusion

- The greatest overlap of the lesions appeared in the intersection between the parietal and occipital lobe in the right hemisphere
- A small, less significant, population of lesions also appeared in the lateral prefrontal cortex on the left hemisphere
- T-test revealed significantly more patients had lesions within the SLF along with an average lower LDSB hinting at the SLF's role in working memory.

Future Work

- Collect data for all patients in the registry
- Utilize different tests that measure working memory
- Create data collection standards that more strongly correlate to and measure working memory impairments.
    - Low LDSB score
    - LDSF-LDSB≥ 3 and low LDSB score
- Generate voxel-based lesion-symptom mapping

Acknowledgments

Special thanks to thank Dr. Bowren and Dr. Tranel for all their guidance throughout this research experience. Thank you to the University of Iowa and the SSTP program for this amazing opportunity.

References

1. Baddeley, A. (1992). Working memory. Science, 255(5044), 556–559. https://doi.org/10.1126/science.1736359
2. Pisoni, A., Mattavelli, G., Casarotti, A., Comi, A., Riva, M., Bello, L., & Papagno, C. (2019). The neural correlates of auditory-verbal short-term memory: A voxel-based lesion-symptom mapping study on 103 patients after glioma removal. Brain Structure and Function, 224(6), 2199–2211. https://doi.org/10.1007/s00429-019-01902-z
3. Geva, S., Truneh, T., Seghier, M. L., Hope, T. M., Leff, A. P., Crinion, J. T., Gajardo-Vidal, A., Lorca-Puls, D. L., Green, D. W., & Price, C. J. (2021). Lesions that do or do not impair digit span: A study of 816 stroke survivors. Brain Communications, 3(2). https://doi.org/10.1093/braincomms/fcab031
4. Faria, C. de, Alves, H. V., & Charchat-Fichman, H. (2015). The most frequently used tests for assessing executive functions in aging. Dementia & Neuropsychologia, 9(2), 149–155. https://doi.org/10.1590/1980-57642015dn92000009

Effect of Interface Geometry on Dielectric Properties of Ceramic-Polymer Composites

Xuan Yang, Jake Atzen, Xuan Song

McCallie School, Chattanooga, TN, Department of Industrial and Systems Engineering, University of Iowa

Background

Piezoelectricity is the property of certain material that have a spontaneous electric polarization that enables the generation of a surface charge, in response to the application of an external mechanical stress on the material.

Conventional piezoelectric materials, such as ferroelectric ceramics and piezoelectric polymers, have limitations in terms of energy conversion efficiency and brittleness. However, bi-continuous piezocomposites, which combines a ceramic phase and a flexible polymer phase, demonstrates both mechanical flexibility and piezoelectricity.

Study has shown that 3D printed all-dielectric structures could offer a convenient method to move towards the manufacturing of structures with metamaterial electromagnetic properties and tunable operational frequencies.

We've also proven that the geometry of the interface between the ceramic and polymer does impact the capacitance of the composite. Under the same volume fraction of ceramics, when the interface has a larger surface area and distance, a trend emerges in which capacitance increases.

Objective

The purpose of this project was to validate our actual test results on permittivity of the integrated part by verifying the correct simulation parameters, based on the study of the correlation between the interface geometry and the capacitance of bi-continuous piezocomposites through comparison of data from virtual simulation and actual testing.

Methods

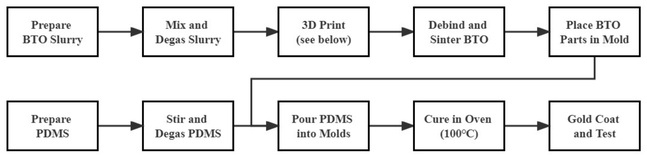

Ceramic Stereolithography Process:

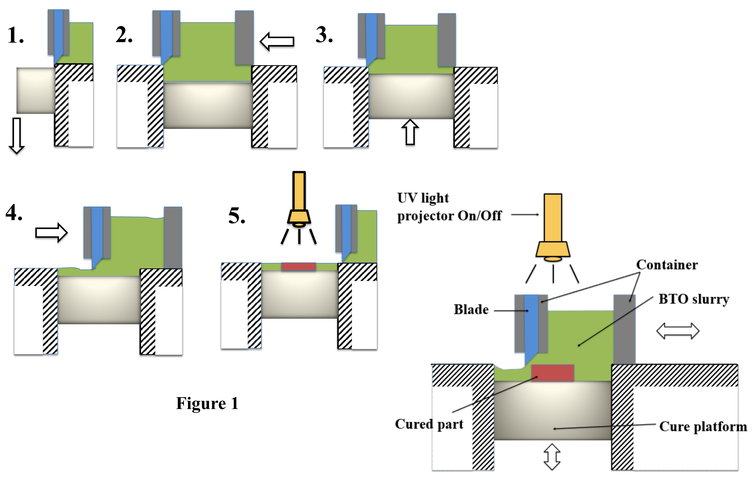

Figure 1

Figure 2

Capacitance Test for BTO / PDMS Parts Using the Analog Discovery 2:

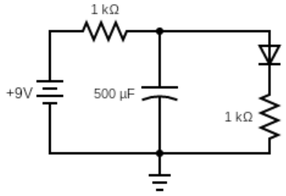

Figure 3

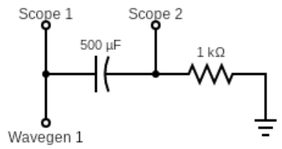

Figure 4

Figure 3: Visualize capacitance using an LED in an RC circuit.
Figure 4: Capacitance testing process for individual part, scope 1 and 2 are oscilloscopes, measuring points on multimeter, wavegen1 is the power source.

Results

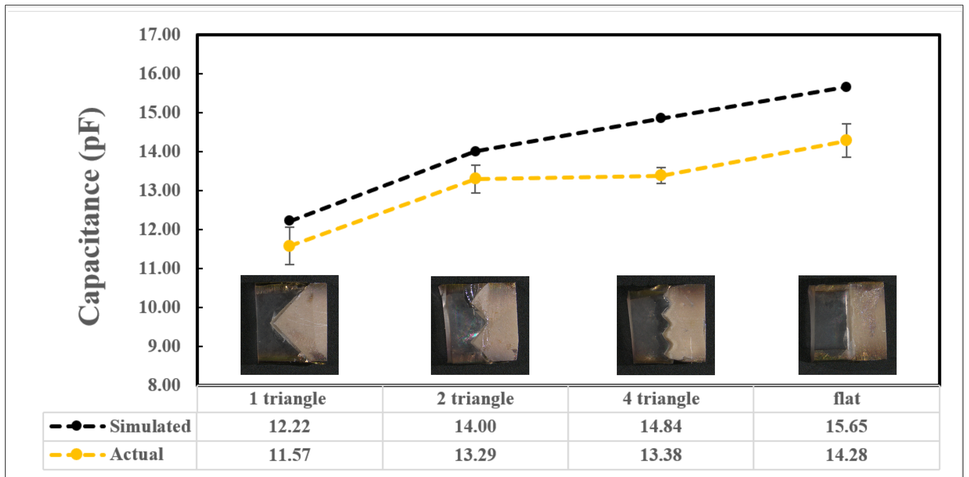

	1 triangle	2 triangle	4 triangle	flat
Simulated	12.22	14.00	14.84	15.65
Actual	11.57	13.29	13.38	14.28

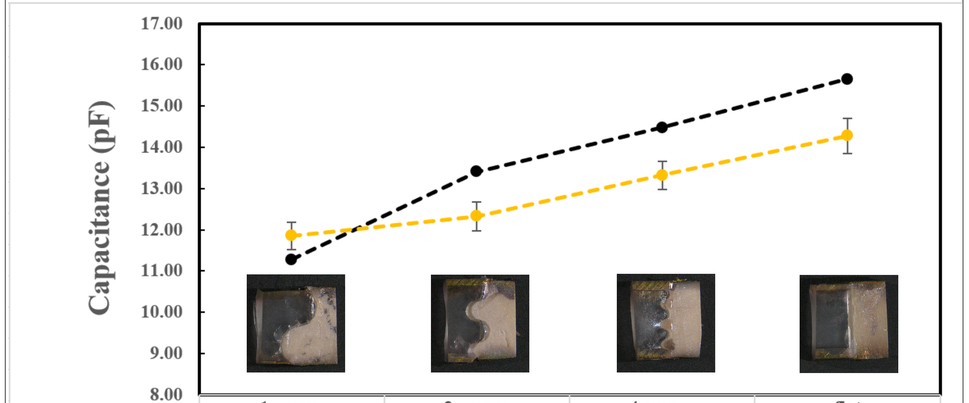

	1 curve	2 curves	4 curves	flat
Simulated	11.28	13.41	14.48	15.65
Actual	11.85	12.33	13.32	14.28

Figure 5&6: Before the experimental value of capacitance was inserted, As interface geometry changes, both values exhibit an accordant rate of change, but actual value is consistently 15% to 20% above the simulated value. Simulated value compared to that of the actual after the test on actual permittivity of PDMS and BTO produced under our process is done. This time simulated value is mostly above the actual and has a smaller deviation from 5% to 10%.

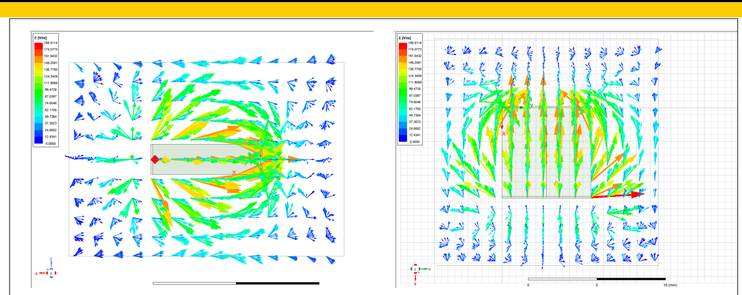

Figure 7& 8: Results of simulated electric field view of integrated part from the side and from the top. Interface geometries does not affect strength and shape of the electric field. The plate area and voltage are the primary factors.

Discussion

- The reason why the simulated capacitance in the first set of experiment is far off from actual value is because the additive manufacturing process for our BTO is not widely used, from the ingredient to heat treatment process. Thus, even though the permittivity of this material could be obtained, the literature value available does not match with the permittivity of the material that's manufactured under our procedure.
- Measuring the capacitance for this specific application is very difficult, in that BTO is a very small and fragile part, so traditional method of measurement, like gold press, does not apply and might produce inconsistent outcome. Therefore, Analogdiscovery2 is used for measurement.
- Given that most segment of simulated capacitance in second trial is higher than that of the actual, the yielded result confirms our previous concern, because simulated capacitance is in an ideal condition. The smaller deviation, which is around 5% to 10%, also enhances the accuracy of the simulation.

Acknowledgements

I would like to give thanks Jake Atzen for his guidance and mentorship throughout my research experience at SSTP program, as well as for Dr. Xuan Song for his advise. I would also like to thank other members in this lab for all the help and support, and I wish the best luck for them in the future. This work is based on materials supported by the National Science Foundation Award No. 1825962.

Reference

1. He, L., Fei, F., Wang, W., & Song, X. (2019a). Support-free ceramic stereolithography of complex overhanging structures based on an elasto-viscoplastic suspension feedstock. ACS Applied Materials & Interfaces, 11(20), 18849–18857. https://doi.org/10.1021/acsami.9b042
2. Isakov, D. V., Lei, Q., Castles, F., Stevens, C. J., Grovenor, C. R. M., & Grant, P. S. (2016). 3D printed anisotropic dielectric composite with meta-material features. Materials & Design, 93, 423–430. https://doi.org/10.1016/j.matdes.2015.12.176
3. Kim, K., Zhu, W., Qu, X., Aaronson, C., McCall, W. R., Chen, S., & Sirbuly, D. J. (2014). 3D optical printing of piezoelectric nanoparticle–polymer composite materials. ACS Nano, 8(10), 9799–9806. https://doi.org/10.1021/nn503268f
4. Song, X., He, L., Yang, W., Wang, Z., Chen, Z., Guo, J., Wang, H., & Chen, L. (2019). Additive manufacturing of bi-continuous piezocomposites with triply periodic phase interfaces for combined flexibility and piezoelectricity. Journal of Manufacturing Science and Engineering, 141(11). https://doi.org/10.1115/1.4044708
5. Su, J., & Zhang, J. (2015). Remarkable enhancement of mechanical and dielectric properties of flexible ethylene propylene diene monomer (EPDM)/ barium titanate (batio3) dielectric elastomer by chemical modification of particles. RSC Advances, 5(96), 78448–78456. https://doi.org/10.1039/c5ra14047a

Increasing Solar Panel Efficiency

Design, Digital Simulation, and Characterization of 3D-Printed Solar Cell System – Solar Cell Concentrator and Sun Tracker

Contributors: Dorothy Zhang, Sebastian Hazlett, Reyna Alam, Maxwell Leonard, Mentors: Dr. Fatima Toor, Dan Keefe, Rezwan Mohammad Sayeed

Introduction

Photovoltaics is a powerful source of energy; however, standard solar panels are approximately 20% efficient, due to recombination and surface reflection losses (PV Education).

Solar concentrators reduce surface reflections, increase absorbance, and suppress radiative recombination (Van Dijk, 2015). Sun trackers maintain the constrained angle of incidence light from the concentrator.

The purpose of our research is to increase the efficiency of solar panels by developing a solar system. Our research questions thus are:

1. What is the optimal geometric concentrator shape, and how can we generate standardized models and digitally test the lux of each?
2. What metallic coat on the concentrator inside can have best reflective properties?
3. How can we implement a sun tracker system either through sensor or data to best take advantage of the concentrator?

Based on previous research done, our hypothesis came to be:

<u>An aluminum coated 8x circular parabolic concentrator will provide the optimal optical properties.</u>

Methods

SOLAR TRACKER DEVELOPMENT – *HARDCODED & PROGRAMMED*

Approach 1: We created a 3D printed dual axis solar tracker inspired by online research. Servo motors continuously rotate until the adjacent photoresistor input differences into the Arduino are within a certain range.

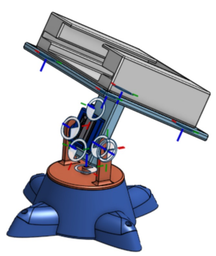

Solar Tracker CAD: *Onshape*

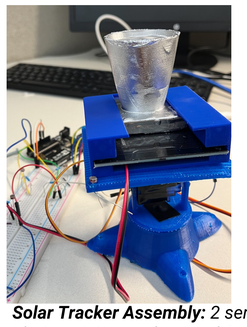

Solar Tracker Assembly: *2 servo, 4 photoresistors, solar panel & concentrator*

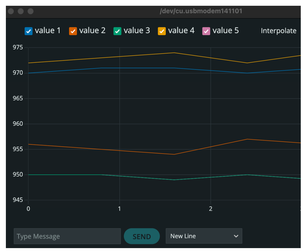

Arduino*: Photoresistor input*

Approach 2: We developed a stepper motor tracker following the sun movements based on the SolTrack library given a time and location

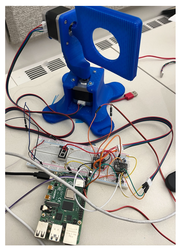

Solar Tracker Assembly

```
from soltrack import SolTrack
import datetime as dt
import AccelStepper
import RPi.GPIO as gp
import utils
import solarglobals
import signal, sys
import steppermovementsystem as step
solarglobals.init()

geo_lon = 41.6578
geo_lat = 91.5346

st = SolTrack(geo_lon, geo_lat, use_degrees=True)
st.set_date_time(dt.datetime.now())
st.compute_position()

step.move_alt_to(st.altitude)
step.move_azi_to(st.azimuth)
step.run_steppers_to_position()
print("Done moving steppers to position")
print("Corrected azimuth, altitude:         %10.6lf° %10.6lf°"    %
print()

def signal_handler(sig, frame):
    print('Ctrl+C pressed, returning steppers to default positions')
    step.move_alt_to(0)
    step.move_azi_to(0)
    step.run_steppers_to_position()
    sys.exit(0)
```

Python code: *SolTrack Library*

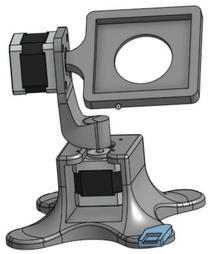

Solar Tracker CAD: *Onshape*

SOLAR CONCENTRATOR DEVELOPMENT -- *SHAPE & REFLECTIVE MATERIAL*

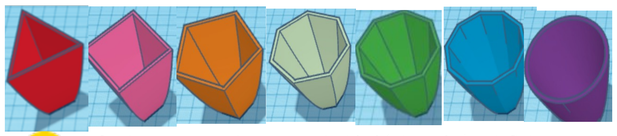

1 ***Solar Concentrator CAD:*** *From 3-sided (triangular) to infinite-sided (circular) parabolic shapes*

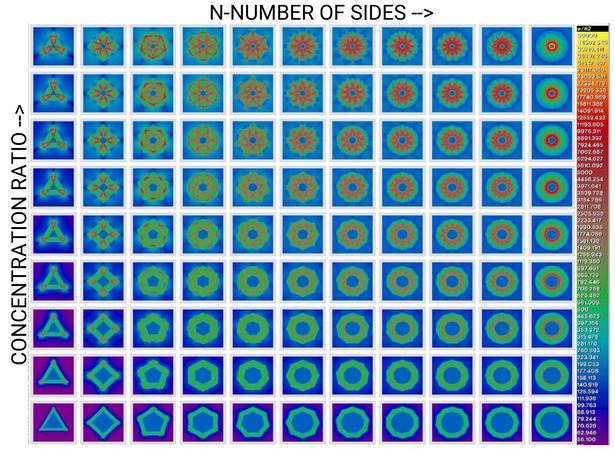

2 ***Figure 1:*** *Radiance simulation of energy lux (w/m^2) on bottom aperture dependent on concentration ratio and n-gon*

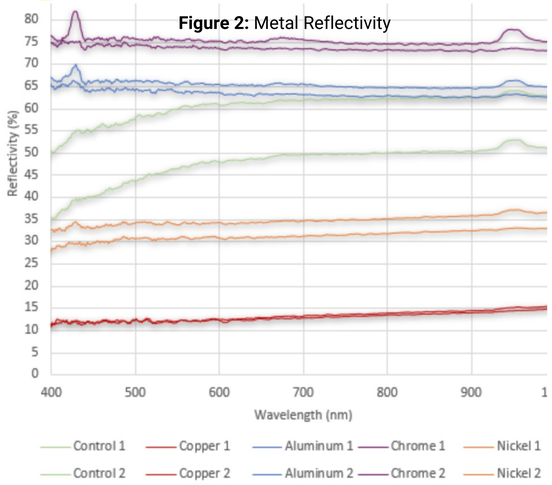

4 ***Metal characterization system:*** *spectrometer, integrated sphere, light source, into graph*

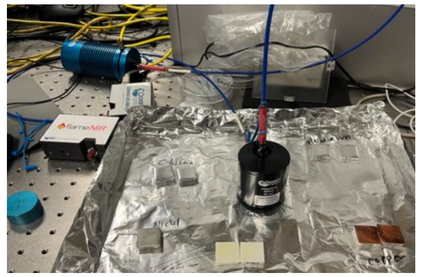

5 **Finished Solar Concentrators:** 2x, 5x, 10x, & 4, 5, 8, infinite sided

6 **PV Education:** Solar Simulator Setup

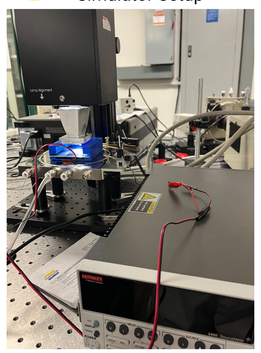

Solar Simulator: 13x circular concentrator

3 ***QR Code: Detailed project repository***

1. Wrote an **OpenSCAD script to parametrically generate a matrix** of 2x through 10x magnification, 3 through 12 n-side polygon parabolic concentrators, with dimensions based on Al-Shidhani's research.
2. **Rendered the concentrators in Radiance**, a ray tracing software, to digitally simulate the effects of sunlight at a 0% acceptance angle (straight above) on the renders with mirror material.
3. Processed the luminance HDR (high dynamic range) images in **Matlab to calculate the amount of lux** (w/m^2) fallen on the bottom aperture of the solar cell.
4. **Characterized the reflectivity of various flat** pieces spray with chromium, aluminum, control, copper, nickel material. Using Ocean Optics spectrometer, we found chromium to have optimal reflectivity.
5. **Polished using XTC-3D Print Coating**, a combination of two basic chemicals which dissolves and redistributes the texture surface and coated the polished **concentrator with chromium spray paint.**
6. Used PV Education **solar simulator and 3D print holder to test efficiency** (short circuit current density) of concentrator on a standard solar cell.

Results

RADIANCE FINDINGS

MATLAB analyses of ray-traced Radiance renders found the highest optical efficiency in the circular 13x concentrator (height = 60cm, bottom radius=10mm, half-acceptance angle = 37 degrees, n-sides = 256).

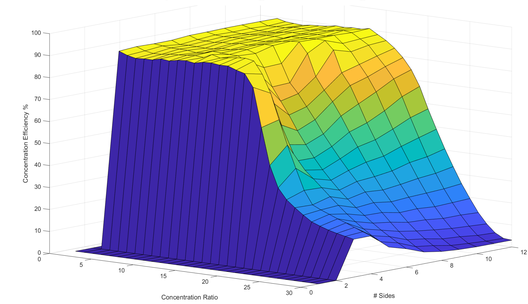

Figure 3: Radiance Ray Tracing & Matlab Results

SOLAR SIMULATOR FINDINGS

Highest non-control short circuit current density (Jsc) was the circular 10x concentrator. An increase in sides showed clear increase in efficiency, but concentration ratios didn't correspond.

<u>This confirms Thomas Cooper's previous work on parabolic solar concentrators, as well as the shape aspect of our original hypothesis.</u>

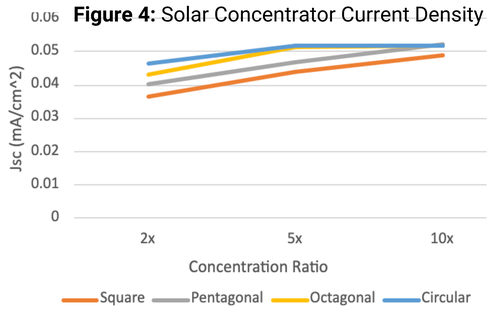

Acknowledgments

Thank you for your guidance, Dr. Toor, Dan, and Rezwan, I could not have done this work without you. Thank you to my stellar research group, Maxipad the computer, Sebas the cyborg, and Reyna the Reyba, my family for the summer. And Nick you're a real one. Caleb you're cool too.

References

1. Al-Shidhani, M., Al-Najideen, M., Rocha, V. G., & Min, G. (2018). Design and testing of 3D printed cross compound parabolic concentrators for LCPV systems. *AIP Conference Proceedings*. https://doi.org/10.1063/1.5053489
2. Cooper, Thomas, et al. "Performance of Compound Parabolic Concentrators with Polygonal Apertures." Solar Energy, 20 July 2013, www.sciencedirect.com/science/article/pii/S0038092X13002533.
3. Van Dijk, L., Marcus, E. A. P., Oostra, A. J., Schropp, R. E. I., & Di Vece, M. (2015). 3D-printed concentrator arrays for external light trapping on thin film solar cells. *Solar Energy Materials and Solar Cells*, *139*, 19–26. https://doi.org/10.1016/j.solmat.2015.03.002
4. "Photovoltaics." PVEducation, www.pveducation.org/. Accessed 18 July 2023.

The Impact of CO_2 on EEG and Breathing Before and After Induced Seizure in an Amygdala-Kindled Mouse

Yiming Zhao[1], Rui Li[2,3], Katelyn G. Joyal[2,3,4], and Gordon F. Buchanan[2,3]

[1]The Governor's Academy, Byfield, MA, USA, [2]Iowa Neuroscience Institute, [3]Department of Neurology, Carver College of Medicine, Iowa City, IA, USA [4]Interdisciplinary Graduate Program in Neuroscience

Introduction

- Sudden unexpected death in epilepsy (SUDEP) ranks second only to stroke in years of potential life lost among all neurological diseases[1].
- SUDEP tends to follow a generalized tonic-clonic seizure which can cause hypercapnia[2].
- Respiratory dysfunctions have been implicated in the etiology of SUDEP[3].
- Promoting signaling from the neurons in charge of the hypercapnic response can reduce the length of a SUDEP risk marker[4] and modulate post-ictal breathing[5].
- Therefore, the objective of the current study is to examine the impact of CO_2 on EEG and breathing before and after an induced seizure.

Hypothesis: We hypothesized that the impact of CO_2 on EEG and breathing may differ before and after an induced seizure

Methods

Surgery

An EEG/EMG headmount was surgically implanted in a C57BL6/J mouse along with a bipolar electrode inserted into the right amygdala.

Kindling

After recovery, the mouse was stimulated with a small current determined by afterdischarge thresholding twice every day until it produced consistent generalized seizures.

Recording With Closed-Loop System

A custom MATLAB script was used to record EEG/EMG/plethysmography data. When RMS value of the EEG data exceeded a predetermined threshold, the script automatically triggers the gas valve to allow for the influx of 7% CO2 air for 5 minutes

Data Analysis

EEG and plethysmography collected during CO2 influx from pre- and post-seizure settings were analyzed using a custom Matlab script utilizing the EEGLab toolbox. Appropriate statistical analysis was performed.

Results

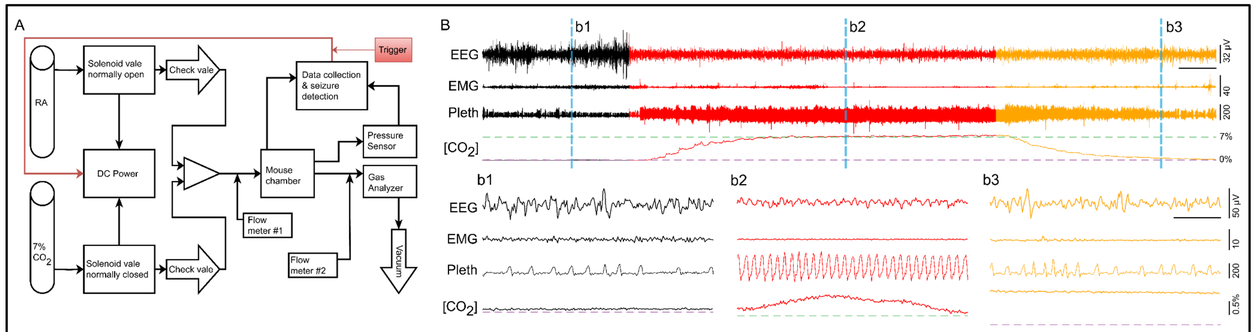

Figure 1. Schematic (A) and example traces (B) recorded using the closed-loop system of an amygdala kindled mouse.of closed-loop system. The horizontal bars in (B) and (b1-3) indicate 30 sec and 1 sec, respectively.

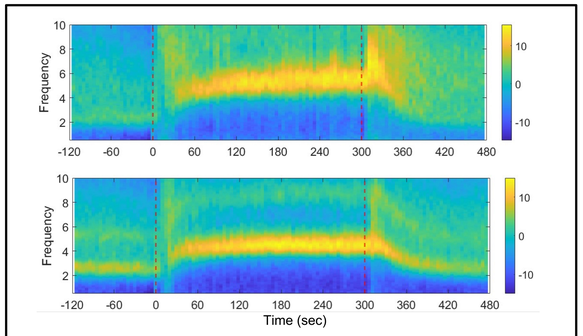

Figure 3. Comparison of breathing patterns in response to CO_2 before (top) and after (bottom) induced seizure.

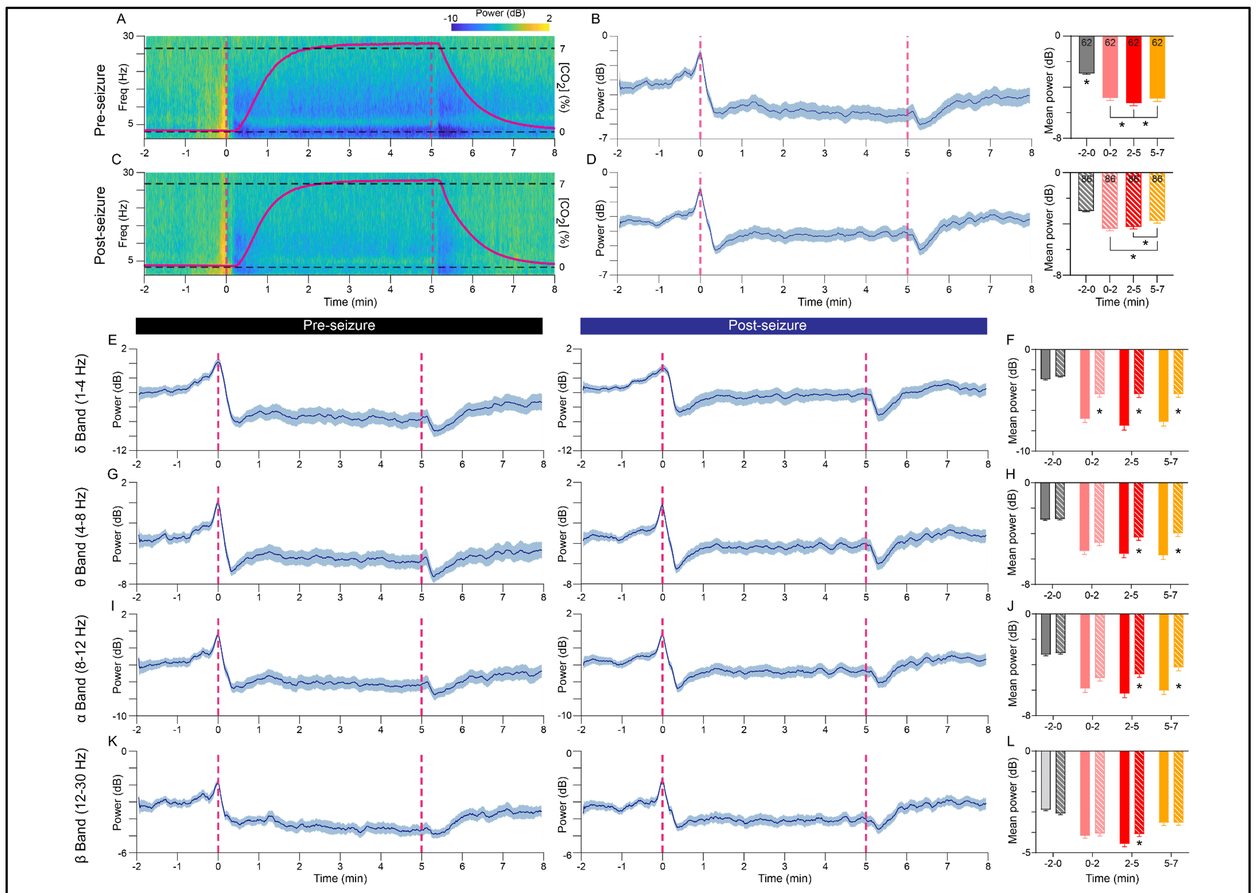

Figure 2. Changes of EEG activity in response to 7% CO_2 challenge pre and post an induced seizure. (A-D) Heatmaps (A and C) of averaged EEG power changes of all trials in response to elevated CO_2 concentration (indicated by the overlaid magenta curve) before (A) and after (C) an induced seizure. Mean values across 1-30 Hz frequency band were extracted and summarized in (B and D). Changes in different frequency bands of EEG activity were analyzed. (E and F) for delta band, (G and H) for theta band, (I and J) for alpha band, and (K and L) for beta band. Solid colored bar graphs indicate pre-seizure CO_2 challenge, while shaded colored bar graphs indicate post-seizure CO_2 challenge. One-way ANOVA was used for (B and D), and two-way ANOVA was used for (F, H, J, and L). * indicates p <0.05.

Conclusion and Future Directions

- CO_2 suppressed EEG activity in both pre- and post-seizure settings
- The delta band power of the EEG data are notably less suppressed by CO_2
- In the future, more detailed analysis on breathing data is required to fully decode the effect of CO_2 on breathing pattern
- We would also investigate the interaction between CO_2 and seizure in the context of the serotonergic (5-HT) system,

References

1. Thurman, D. J., Hesdorffer, D. C., & French, J. A. (2014). Sudden unexpected death in epilepsy: Assessing the public health burden. *Epilepsia*, *55*(10), 1479-1485. https://doi.org/10.1111/epi.12666
1. Ryvlin, P., Nashef, L., Lhatoo, S. D., Bateman, L. M., Bird, J., Bleasel, A., Boon, P., Crespel, A., Dworetzky, B. A., Høgenhaven, H., Lerche, H., Maillard, L., Malter, M. P., Marchal, C., Murthy, J. M., Nitsche, M., Pataraia, E., Rabben, T., Rheims, S., . . . Tomson, T. (2013). Incidence and mechanisms of cardiorespiratory arrests in epilepsy monitoring units (MORTEMUS): A retrospective study. *The Lancet Neurology*, *12*(10), 966-977. https://doi.org/10.1016/s1474-4422(13)70214-x
2. Sainju, R. K., Dragon, D. N., Winnike, H. B., Nashelsky, M. B., Granner, M. A., Gehlbach, B. K., & Richerson, G. B. (2019). Ventilatory response to co₂ in patients with epilepsy. *Epilepsia*, *60*(3), 508-517. https://doi.org/10.1111/epi.14660
3. Petrucci, A. N., Joyal, K. G., Chou, J. W., Li, R., Vencer, K. M., & Buchanan, G. F. (2021). Post-ictal generalized EEG suppression is reduced by enhancing dorsal raphe serotonergic neurotransmission. *Neuroscience*, *453*, 206-221. https://doi.org/10.1016/j.neuroscience.2020.11.029
4. Joyal, K. G., Petrucci, A. N., Littlepage-saunders, M. V., Boodhoo, N. A., Wendt, L. H., & Buchanan, G. F. (2023). Selective serotonin reuptake inhibitors and 5-HT2 receptor agonists have distinct, sleep-state dependent effects on postictal breathing in amygdala kindled mice. *Neuroscience*, *513*, 76-95. https://doi.org/10.1016/j.neuroscience.2023.01.016

Acknowledgements

This work was supported by the Belin-Blank Center, NIH/NINDS R01 NS095842 and NS129722 (GFB) and the Beth L. Tross Epilepsy Professorship (GFB).

Effects of Stimulant Medication on Social Behavior for Three Children with ADHD

Carolyn Zhou[1], Matthew J. O'Brien, PhD[2], Alex Pauls, MA[2]
[1]The Pingry School, Basking Ridge, NJ, [2]Center for Disabilities and Development, University of Iowa, Iowa City, IA

University of Iowa Stead Family Children's Hospital

Introduction

- ADHD is one of the most diagnosed neurodevelopmental disorders in children[1]
- 90% of diagnosed children are treated with stimulant medications[2]
- While the efficacy of these medications on reducing challenging behaviors is well documented, little is known about the side effects, particularly on social play[2]

Objective: Determine the effect of stimulant medication on decreasing social behavior in 3 children with ADHD

Participants

Ross (7 y.o.)	ADHD, ODD, dyslexia, dysgraphia, anxiety, chronic motor tic disorder	15 mg Ritalin (MPH-IR) 2x daily
Chandler (7 y.o.)	ADHD	27 mg Concerta (MPH-ER) every morning 5 mg Ritalin (MPH-IR) as needed
Joey (12 y.o.)	ADHD	30 mg Vyvanse (Lisdexamfetamine-ER) every morning

Methods

- Observed seven-14 free play sessions on and off meds during functional analysis (FA) or free operant preference assessment (FOPA)
- 5-minute sessions were coded by a primary and reliability coder for the following behaviors:

Frequency:
- Verbal, gestural, physical initiation & reciprocation
- Therapist initiation and reciprocation

Duration:
- Interactive play
- Solitary play
- Orienting towards
- Orienting away

Results

Fig. 1: Ross Rates of Initiation/Reciprocation

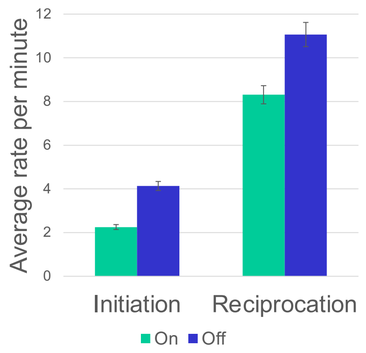

Fig. 2: Ross % Engagement

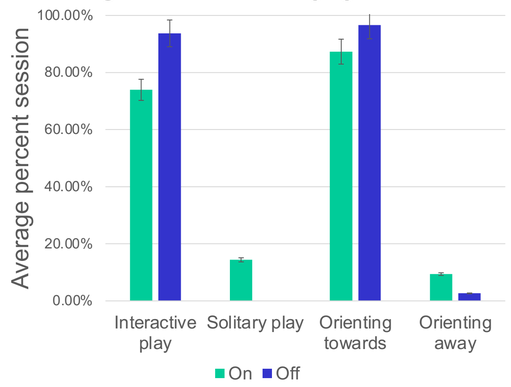

Fig. 3: Chandler Rates of Initiation/Reciprocation

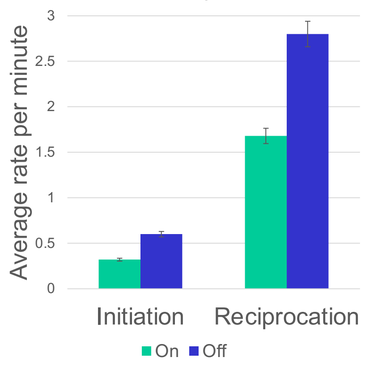

Fig. 4: Chandler % Engagement

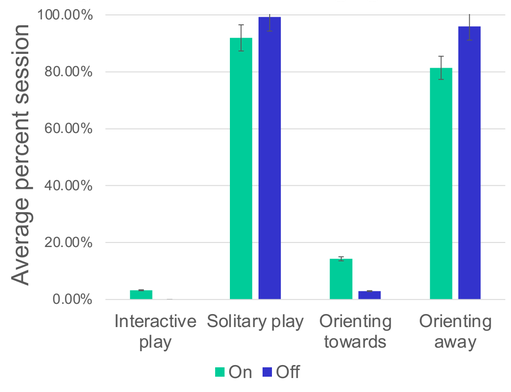

Fig. 5: Joey Rates of Initiation/Reciprocation

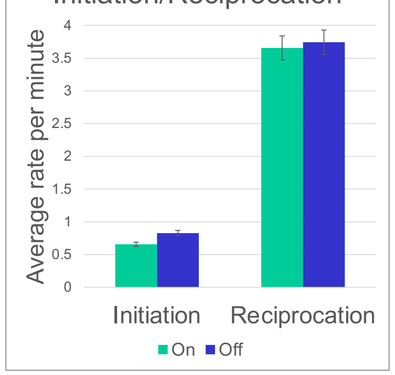

Fig. 6: Joey % Engagement

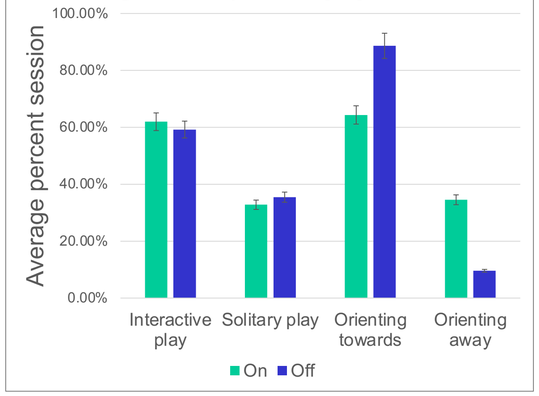

Discussion

- Results support hypothesis that stimulants cause decrease in socialization in kids with ADHD, with some nuances

	Initiation/ reciprocation	Play	Orientation
Ross	Considerable increase in initiation/ reciprocation off meds	Higher % of session interactive/no % solitary off meds	Higher % of session towards/less away off meds
Chandler	Considerable increase in initiation/ reciprocation off meds	Minimal levels of interactive regardless, overlap of solitary %	Minimal levels of towards regardless, higher % away off meds
Joey	Negligible increase in initiation/ reciprocation off meds	Negligible % of increase of interactive on meds, solitary off meds	Higher % of session towards/less away off meds

Conclusion

- Overall, averages of initiation/reciprocation rates of all three individuals show considerable increase off medications
- Negligible differences in play may indicate less of marker for social behavior
- Slight difference in orientation
- Limited sample size, correlation between social play and stimulants should be studied more in depth
- Help inform doctors, patient, and family about side effects of medication

References

1. Scandurra, V., Emberti Gialloreti, L., Barbanera, F., Scordo, M. R., Pierini, A., & Canitano, R. (2019). Neurodevelopmental Disorders and Adaptive Functions: A Study of Children With Autism Spectrum Disorders (ASD) and/or Attention Deficit and Hyperactivity Disorder (ADHD). *Frontiers in psychiatry*, *10*, 673. https://doi.org/10.3389/fpsyt.2019.00673
2. Larue, R. H., Northup, J., Baumeister, A. A., Hawkins, M. F., Seale, L., Williams, T., & Ridgway, A. (2008). An evaluation of stimulant medication on the reinforcing effects of play. *Journal of Applied Behavior Analysis*, *41*(1), 143-147. https://doi.org/10.1901/jaba.2008.41-143